Nano-Enabled Optoelectronic and Mechatronic Devices

A dissertation submitted by
Kasturi Gogoi

to
Indian Institute of Technology Guwahati
for the award of the degree of
Doctor of Philosophy

Centre for Nanotechnology
Indian Institute of Technology Guwahati

Guwahati – 781039, Assam, India

June, 2022

DECLARATION

The thesis entitled "**Nano-Enabled Optoelectronic and Mechatronic Devices**" is an original work carried out by me under the supervision of **Prof. Arun Chattopadhyay, Department of Chemistry, Indian Institute of Technology Guwahati**. This thesis has been submitted by me to the **Centre for Nanotechnology, Indian Institute of Technology Guwahati** for the award of the degree of Doctor of Philosophy.

I declare that, this thesis has not been submitted elsewhere for award of any degree or diploma.

Kasturi Gogoi.

Kasturi Gogoi

Centre for Nanotechnology
Indian Institute of Technology Guwahati
Guwahati-781039
Assam, India

June, 2022
Guwahati

CERTIFICATE

This is to certify that the work contained in the dissertation entitled “**Nano-Enabled Optoelectronic and Mechatronic Devices**” being submitted to the **Indian Institute of Technology Guwahati**, by ***Kasturi Gogoi*** (Roll No. **166153002**), for the award of the degree of **Doctor of Philosophy** in ***Nanotechnology*** is a bonafide record of research work carried out by her. The contents of this thesis are solely the results of her original findings. She has meticulously carried out the investigations and followed the guidelines of the laboratory.

This work has not been submitted elsewhere for any degree or diploma.

Prof. Arun Chattopadhyay
Department of Chemistry
Indian Institute of Technology Guwahati
Guwahati-781 039, INDIA

Arun Chattopadhyay

Professor
Department of Chemistry
Centre for Nanotechnology
Indian Institute of Technology Guwahati
Guwahati-781039, Assam, India

June, 2022
Guwahati

Dedicated to…

My Parents

ACKNOWLEDGEMENT

I would like to express my heartfelt gratitude to everyone who has helped me in any manner throughout my Ph.D in every beautiful way possible.

I extend my sincere gratitude to Prof. Arun Chattopadhyay, my thesis supervisor for giving me this opportunity to be a part of this esteemed institution and pursue research work under his supervision. I express my heartfelt thanks for being the constant support and motivating me to strive for excellence. This dissertation would not have been possible without his consistent guidance and encouragement. His commitment towards research and thirst for novelty always inspired me to put my best towards work. I would always be grateful for his contributions in shaping my research career.

I would like to thank my doctoral committee members Prof. Siddhartha Sankar Ghosh, Prof. Roy P. Paily, Dr. Partha Sarathi Guha Pattadar for evaluating my thesis work and for their valuable comments and suggestions which helped me improve my dissertation work.

A special thanks to the Centre for Nanotechnology, Department of Chemistry, Central Instruments Facility, Indian Institute of Technology Guwahati, for allowing me to access the state of the art facilities to execute my research work.

I would like to thank my collaborators Dr. Sabyasachi Pramanik and Srimanta Pal for giving me the opportunity to learn from them and for their constant involvement in executing the experiments. I would also like to thank my seniors Dr. Sunil Kumar Sailapu and Dr. Deepanjalee Dutta for teaching me and for the constant motivation. I would also like to thank Anitha T. Simon and Mihir Manna for their help and support throughout this journey. I would also like to express my sincere regards to senior and junior lab mates for their helping hand in need and for all the wonderful memories shared together. I thank all my friends who have made my life colourful and the moments together will be treasured forever.

A sincere gratitude to my parents for being the pillars of my journey. Also specials thanks to my dearest sisters to stand by my side every hour.

-Kasturi

ABSTRACT

Moore's Law, which predicts the rise in processing performance of semiconductor chips due to downsizing of device dimensions, has primarily driven advances in semiconductor technology during the last few decades. As the physical device scales approach atomic dimensions, further downsizing is limited due to quantum – mechanical effects and inter-atomic interactions. Hence, nanoelectronics emerged as a promising complementary technology, that provided novel methods and architectures in order to bring in atomic scale interactions to macroscopic functionalities. Nanoelectronics holds significant promise for expansion of electronic device performances. As for example, it facilitates low energy usage, self-powered operations, and photoluminescence, which are applicable in the areas of optoelectronics, flexible technology, displays, wearable technology and energy technology to name a few.

This dissertation work is focussed towards fabricating semiconducting devices through incorporation of their physical and chemical properties at the nanoscales. In particular, functional properties of quantum dots and nanoparticles were modified through ligand interactions and semiconducting devices were engineered for applications towards thin film transistors, UV-photodetectors and multi-stimuli responsive mechanoreceptors in flexible frameworks. **Chapter 1** presents a brief introduction to nanomaterials, their functional properties and different approaches to tailor their physical and chemical properties. A short insight is given on nanomaterial deposition techniques for fabrication of semiconducting devices. Successively, brief description on thin film transistors, photodetectors and self-powered detectors are presented. An insight is presented on different categories of tactile sensors and in addition, recent advancements in this arena are discussed. At the end, we present an overview of the challenges and scopes for developing multifunctional devices targeting different applications. **Chapter 2** presents synthesis of Mn^{2+}-doped ZnS quantum dots and surface complexation of these quantum dots with 8-hydroxyquinoline 5-sulphonic acid ligand. Herein photoluminescence characteristics of surface complexed quantum dot due to the formation of bluish green emitting zinc quinolate ($Zn(QS)_2$) complex are discussed. Thin film transistors were fabricated and device characteristics such as carrier mobilities, carrier densities, trap state densities and carrier hopping characteristics at variable temperatures were studied. **Chapter 3** presents fabrication of Mn^{2+} doped ZnS quantum dot complex

photodetectors (QDC-PD) for efficient and ultrasensitive detection of UVA radiations. In the same context, effect of Mn^{2+} doping in ZnS Qdot and surface modification of doped Qdot in the detector performance were studied. A shift in the detection band from UVC in Qdot to UVA in QDC was observed due to the formation of a luminescent moiety at the Qdot surface. UV- photodetection under self-powered mode was demonstrated. Also, the dual emitting feature of QDC was utilized as an anti-counterfeiting ink for data encryption. In **Chapter 4,** a highly sensitive tactile sensor developed from a crosslinked gold nanoparticle network and a micro-structured PDMS layer is demonstrated. Herein, the device responses to mechanical deformations and external stimuli were recorded and piezo-resistive nature of gold nanoparticle network was studied under applied mechanical strain. The tactile sensor enabled recognition of physical activities such as jogging, leg movements, standing, tapping action and also to identify weight and vibration. To enhance the multifunctional attributes of the tactile sensor, the piezo-phototronic nature of the assembled nanoparticles was also explored. **Chapter 5** summarizes the works carried out in the dissertation and highlights the key objectives achieved. It also presents future prospects of this dissertation work especially the novel application potential in diverse fields.

Contents

ABBREVIATIONS

AFM	Atomic Force Microscopy
Au	Gold
Au NP	Gold Nanoparticles
CIE	Commission International d'Eclairage
EDX	Energy Dispersive X-Ray
FESEM	Field Emission Scanning Electron Microscopy
FET	Field Effect Transistor
FTIR	Fourier Transform Infrared Spectroscopy
HRTEM	High resolution transmission electron
LEFET	Light Emitting Field Effect Transistor
LED	Light Emitting diode
Mn	Manganese
MPTES	3-mercaptopropyl trimethoxy silane
PA	Picolileamine
PD	Photodetector
PL	photoluminescence
PDMS	Polydimethylsiloxane
PET	Polyethylene terephthalate
Qdot	Quantum Dot
QDC	Quantum dot Complex
QY	Quantum Yield
SAED	Selected area electron diffraction
SERS	Surface enhanced raman spectroscopy
SPR	Surface plasmon resonance
TEM	Transmission Electron Microscopy
TRPL	Time-Resolved Photoluminescence

UV	Ultraviolet
XRD	X-Ray Diffraction

Chapter 1

Introduction

Nanoscience and nanotechnology have made ground-breaking achievements in the last few decades and have expanded their footprints in almost every discipline of science and technology. Miniaturization, high density integration, low power consumption, manifold improvement in performance and cost of production are the prime trajectories that the electronics industry traverses on. Substantial breakthrough in materials chemistry, versatile chemical and physical properties of nanomaterials have opened up platforms for a wide array of applications. Applications of nanomaterials in electronics have given rise to new directions and have accelerated the technological leap. Advancements in nanoelectronics is targeted mainly towards fabrication of environmentally benign and application driven sensors, photodetectors, transistors, logic devices, solar cells, light emitting diodes, wearable gadgets, energy harvesting systems and flexible electronic devices. Effective design and fabrication of multifunctional systems from functional nanomaterials that facilitate synergistic coupling between different physical environments would be a novel approach to build intelligent systems. The concept of nanotechnology was first introduced by Nobel laureate Richard Feynman in 1959, which now has become a wide area of research that deals with materials in the size domain 1 nm -100 nm. To be precise one nanometer is equivalent to one billionth of a meter (10^{-9} m). When materials are scaled down to nanometer range, their chemical and physical properties are completely different from that of their bulk properties. Nanotechnology and their synthetic procedures allow us to manipulate these properties through controlled growth, nanoparticle assembly formation and surface functionalization in accordance with the application of interest. Physical dimensions of nanomaterials could be confined from all the three dimensions (nanosheet- confined in one dimension, nanowire- confined in two dimensions, nanoparticle/ quantum dots- confined in all the three directions), which facilitate large surface to volume ratio, exhibit quantum confinement effects and allow dynamic interactions that enhance their application potential.

1.1 Metal Nanoparticles

Metallic nanoparticles (NP) draw immense interest because of their unique optical, electrical and magnetic properties dictated by their shape, size and composition. Metallic nanostructures, when impinged with photons of certain energy, produces free electron clouds known as localized surface plasmons (LSP), which coherently oscillate in the metal surface and generate strong electromagnetic field near the surface of the nanostructure (**Figure 1.1a**).

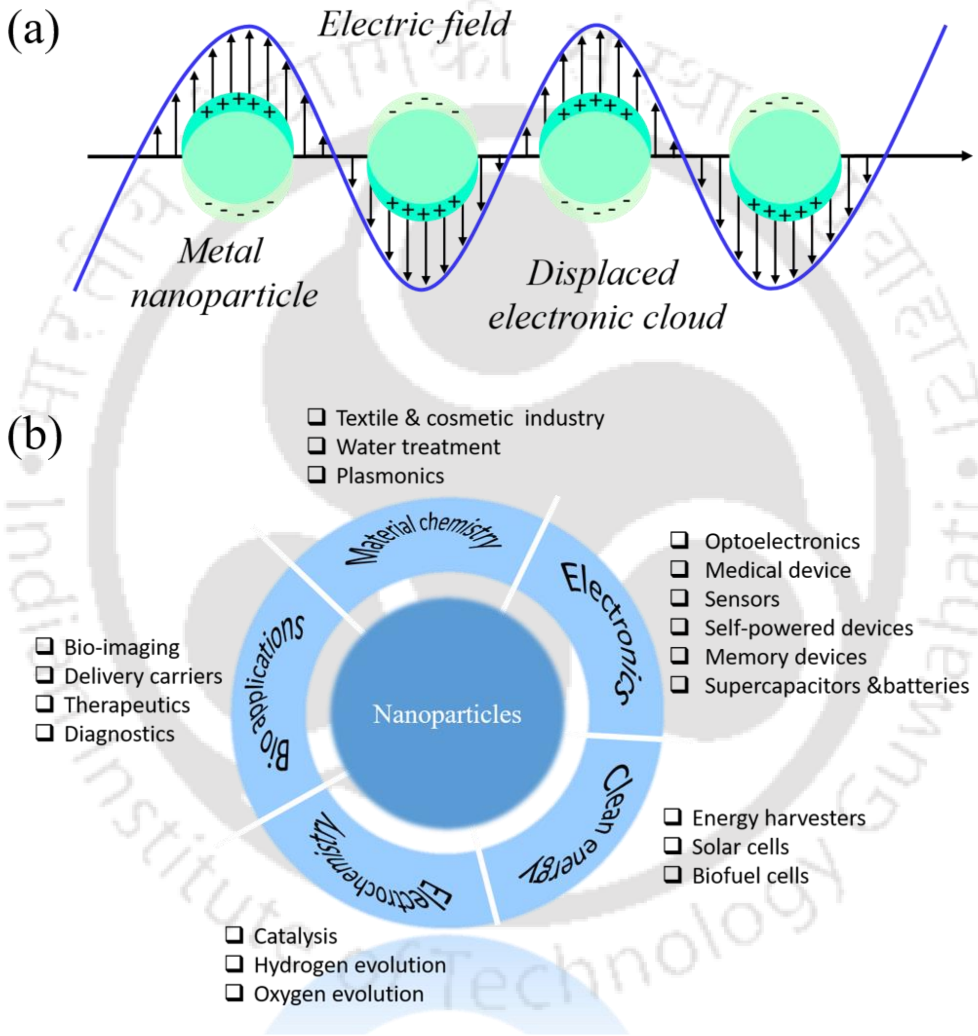

Figure 1.1. (a) Schematic representation of localized surface plasmon resonance in metal nanoparticles and (b) broad area of application of functional nanomaterials.

Controlled organization of these metal nanoparticles can couple localized surface plasmons of individual nanostructures and generate hybrid plasmons. These oscillating plasmons can relax radiatively by re-emitting photons or non-radiatively through generation of non-equilibrium hot carrier population, which dissipate their energy via heating of the nanostructured framework. Based on this phenomenon, a number of applications have been demonstrated such as enhancement in chemical reactivity[1] and photocurrent generation.[2] For instance, gold nanoparticles (AuNP) decorated on MoS_2 layers exhibited enhancement in the photocurrent generation, which was further improved through periodically arranged AuNP.[2] On a similar note, graphene quantum dot when incorporated with AuNP showed superior broadband detection capabilities.[3] In addition to their wide scale application potential in photochemistry,[4, 5] bio imaging[6, 7] therapeutics,[8] and material chemistry[4] these are predominantly studied in the field of clean energy[9] as well as electronic devices[10] (**Figure 1.1b**). In addition, crosslinked nanoparticles have gained significant interest because of beneficial carrier tunnelling between the particles, which provides applicability in numerous fields. The charge transport in crosslinked nanoparticles is dependent on the interparticle distance, which is governed by structural features of the stabilizing ligand. In this regard, chemiresistive sensors are developed that are responsive towards different analytes depending on the type of the cross linker.[11] In the recent past, such nanoparticle frameworks have also been used as strain sensitive tactile sensors.[10, 12] These molecularly mediated assemblies of nanoparticles offer piezoelectric characteristics which have been employed to design static and dynamic pressure sensor, motion detectors, pulse sensors, breath analyser etc.[10, 13]

1.2 Quantum Dots

Semiconducting quantum dots (Qdots) owing to their zero dimensionality demonstrate strong size dependency on their optical and electronic charge transport properties due to quantum confinement of their electronic wavefunctions. Over the last three decades, Qdots have been important materials of research interests and are considered ideal absorbers as well as emitters to be utilized for next generation solar cells, diodes, photodetectors, catalysis and optical sensors. In addition, due to their size tuneable wide colour gamut, quantum yield, excitation and emission dynamics, colour purity and stability, they are highly anticipated as building blocks for commercial displays. Qdots are zero dimensional nanocrystals, sizes of which range from 1-10 nm. Their versatility originates mainly from the size dependent bandgap and diverse surface modifications made possible by a wide array of ligand interactions, which allows low cost synthesis and fabrication of devices and facilitates facile modifications of electronic properties.

1.3 Functional Attributes of Qdots

1.3.1 Quantum Confinement Effect

The salient feature of Qdots exhibiting size tunable optical and electronic properties attract significant commercial importance. When the size of a semiconductor material is scaled down to the range that approaches the de-Broglie wavelength of an electron the energy levels are discretised unlike continuous energy bands in bulk materials. Upon three dimensional confinement of the physical dimensions of 0 dimensional Qdots to the excitonic Bohr radius of the material, the motion of excitons (electron hole pairs upon photo excitation) are also restricted in all the three spatial coordinates. This phenomenon is known as quantum confinement effect.[14, 15] The degree of confinement is inversely proportional to the size of the Qdots i.e., as the size of the Qdots is reduced, the degree of quantum confinement increases and the energy levels are discretised (**Figure 1.2a**).[15] Discretised energy levels due to quantum confinement effect exhibit extraordinary photoluminescence properties (**Figure 1.2b**), which make them a superior choice for next generation electronic devices especially displays and photovoltaics.

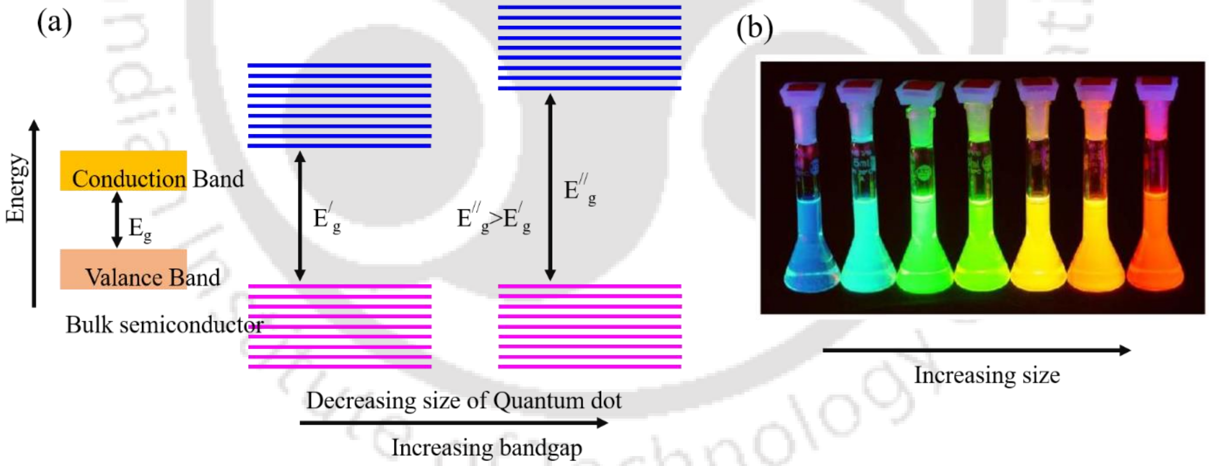

Figure 1.2. (a) Schematic representation of discretization of energy levels due to quantum confinement effect. (b) Photoluminescence of CdSe/ZnS Qdots in the size band 1.7 nm to 5 nm. (Reprinted with permission from reference 15. Copywrite 2002 John Wiley and Sons)

1.3.2 Photoluminescence of Quantum Dots

When photons having higher energy than the band gap of the Qdot is impinged on the material, electrons in the valance band are excited to the conduction band. These poto-excited electrons can relax back to the ground state via two possible pathways, 1. Radiative recombination and

2. Non-radiative recombination. The radiative recombination of photo-excited electrons and holes leads to photon emission, the wavelength of which is largely dependent on the bandgap as well as defect states of the Qdot.[16] Qdots attract huge attention, because precise control of the emission wavelengths could be achieved through tuning the size of the Qdot, doping impurity metals and ligand interactions on the Qdot surface.[15-17] The schematic representation of various processes involved in Qdot photoluminescence is schematically represented in **Figure 1.3**.

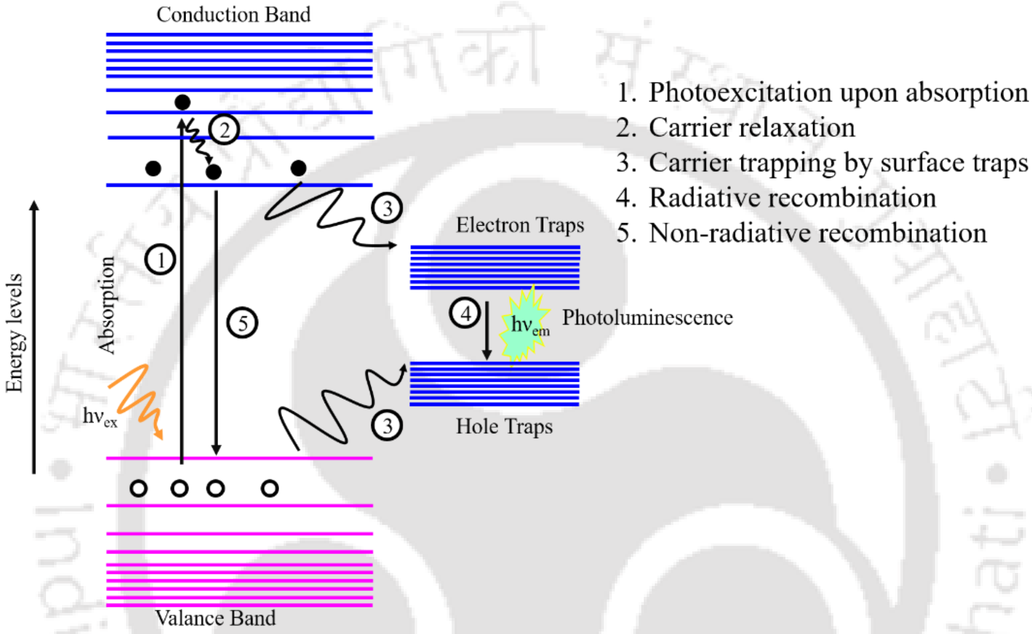

Figure 1.3. Schematic representation of associated processes involved in Qdots photoluminescence.

Size Tailoring

Photoluminescence characteristics of Qdot can be controlled by controlling the physical dimensions of the Qdot. As the size of the Qdot is reduced, a blue shift in the photoluminescence spectrum could be observed whereas, if the size is increased a red shift in the spectrum could be observed. This relationship could be mathematically understood from the Brus equation as follows, where band gap of the Qdot is inversely proportional to its radius.[18]

$$E_g(Qdot) = E_g(bulk) + \left(\frac{h^2}{8R^2}\right)\left(\frac{1}{m_e} + \frac{1}{m_h}\right) - \frac{1.8e^2}{4\pi\varepsilon\varepsilon_0 R} \qquad \mathbf{1.1}$$

Where, E_g is the bandgap, R is the radius of the Qdot, h is the Planck constant, m_e and m_h are the effective mass of electron and hole respectively, ε corresponds to dielectric constant of the material. From the above equation, it can be illustrated that with decrease in the radius of the Qdot (size of the Qdot) the energy band gap is widened. As for example, the photoluminescence of CdSe/ZnS core shell Qdots from diameter 1.7 nm to 5 nm are shown in **Figure 1.2b**, where we can observe size tunable photoluminescence characteristics.[15]

Impurity Doping

Doping of impurity atoms to semiconducting Qdots create intermediate electronic transition states in the bandgap of the material, which allows recombination of the excited electrons via these transition states, and thereby alters the recombination dynamics. As a result, the photoluminescence characteristics of the material changes/shifts to longer wavelengths. Intentional doping of lanthanide and transition metals to Qdots have been reported to have improved carrier lifetime, achieved desired Stokes shift as well as introduced paramagnetic properties to the host Qdot. For instance, doping Mn ions to wide bandgap II-VI compounds such as ZnS and ZnSe, creates energy levels between the bandgap of the host.[19, 20] Photoexcited electrons move from valance band to the conduction band of the host Qdot, which upon relaxation are transferred to the $^4T_1$ transition state of the Mn ion and finally decays radiatively to $^6A_1$ state exhibiting bright orange emission.[20] On a similar note, doping Cu ions to ZnS/ ZnSe exhibits cyan or bright green photoluminescence, in contrast to the blue emission of the host.[21]

Surface Modifications

The surface of the nanostructured materials is reactive due to the presence of interfacial uncoordinated dangling bonds. These unsaturated dangling bonds could effectively become carrier traps, which would result in non-radiative carrier combination. Non-radiative carrier-recombination reduces the quantum yield of a semiconductor thus would reduce its application potential. Recent literature suggests that, there are many surface passivation strategies, that have been proven beneficial in improving phtoluminescence characteristics. Among them, shell passivation, ligand modifications with organic and inorganic ligands and complexation reaction at the Qdot surface are prominent; they help to incorporate desired characteristics to the Qdot surface in addition to surface passivation.

1.3.3 Functionalization of Qdots

Ligand exchange strategies at the Qdot surface has the ability to introduce functional properties to the Qdot, such as solubility,[22] improve quantum yield, introduce chiroptical property,[23] pH sensitivity, improve conductivity due to interdot coupling,[24] reduce trap state density,[25] and enhance charge storage capability[26]. For instance, a colorimetric pH sensor based on fluorescent Qdots, graphene oxide sheets and organic linker molecules was demonstrated, where pH responsive linker molecules poly(acrylic acid) (PAA) and poly(2-vinylpyridine) (P_2VP) are reported to tune the efficiencies of Förster resonance energy transfer from fluorescent Qdot to GO, as a result of which photoluminescence of Qdots are tuned.[27]

1.3.4 Surface Complexation Reactions

Surface complexation on the surface of a Qdot is a newly designed surface modification strategy, where, superior optical and thermal properties were formulated. Surface complexation involves, interaction of an organic ligand at the Qdot surface, that forms inorganic complexes with the chemically reactive surface cations. This leads to the generation of another fluorescent moiety at the generally fluorescent Qdot surface (we term it here as quantum dot complex (QDC)). This type of surface complexation reaction favours incorporation of fluorescent properties of two moieties into a single component without compromising its size and crystallinity.

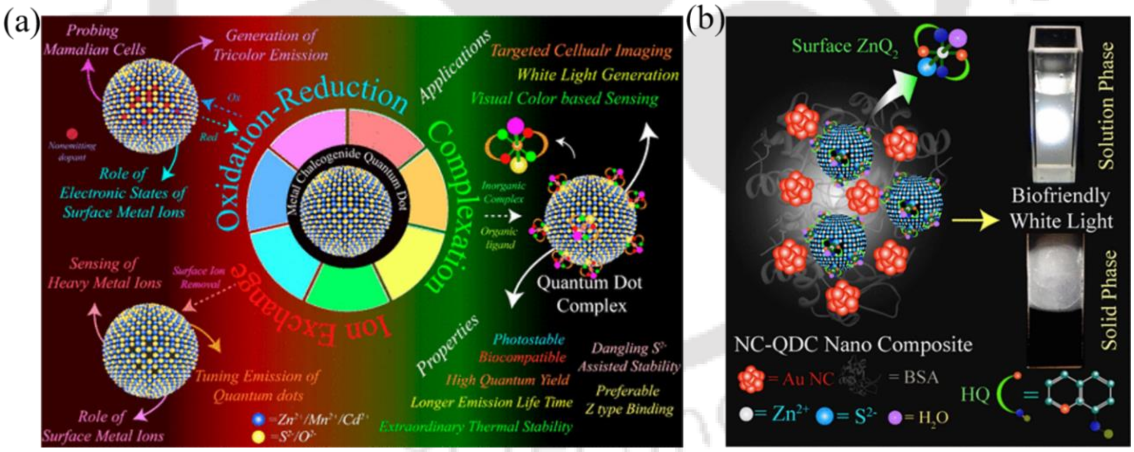

Figure 1.4. (a) Schematic showing salient features and applications of quantum dot complex (QDC). (Reprinted with permission from reference 29. Copywrite 2019 American Chemical Society). (b) Luminescent QDC and gold nanocluster embedded in protein for white light luminescence. (Reprinted with permission from reference 31. Copywrite 2016 American Chemical Society).

As for example, complexation of 8-hydroxyquinoline with ZnS Qdot led to the formation of zincquinolate complex (ZnQ_2) at the Qdot surface, by interacting with the Zn^{2+} dangling bonds of the Qdot. This resulted in the formation of green emitting surface complex moiety. ZnS Qdot with attached ZnQ_2 exhibited higher photoluminescence yield, longer carrier lifetime, and better thermal stability compared to as-synthesised ZnS Qdot.[28] Salient features and significant achievements in complexation reaction mechanisms are presented in **Figure 1.4a**.[29] Notably, such a QDC has been used as a reversible pH sensor where ratiometric change in the luminescence profile was calibrated with the change in pH ranging from 6.5 to 10.3.[30] In another report, nanocomposites of QDC and gold nanocluster embedded in protein have shown overall white light emission that were biocompatible in nature (**Figure 1.4b**).[31]

1.4 Semiconductor Device Fabrication

Top-down approach:

Mechanical exfoliation: It is a top down approach and usually is adopted to exfoliate two-dimensional sheets from bulk material. A small quantity of bulk material is adhered to adhesive tapes and are repeatedly peeled off with another adhesive tape and finally transferred to the device substrate. This process is cost effective and easy to process but the throughput remains inefficient due non-uniformity in the film formation.

Chemical exfoliation: In this method of exfoliation, the bulk material is dispersed in organic solvents such as N-methylpyrrolidine (NMP) or isopropyl alcohol (IPA) and are ultrasonicated usually for a long duration and the resultant is centrifuged to obtain the desired nanocrystals. To speed up the exfoliation process, sometimes metal ions are intercalated during ultasonication process. The nanocrystal dispersion is then drop-cast or sprayed over the substrate.

Physical and chemical vapour deposition- Physical vapour deposition (PVD) techniques such as RF sputtering, pulsed laser deposition, molecular beam epitaxy, thermal and electron beam evaporation are used to obtain wafer scale uniformity and thickness controllability. However, these processes require high end instrumentations and the targets used are not cost effective. The films produced through PVD suffer from high defect concentration and results in non-stoichiometric films with high resistivity. On the other hand, chemical vapour deposition methods facilitate defect free large area growth. However, high temperature and high pressure conditions are notable limitations in this approach as well.

Bottom-up approach: It is a highly efficient and controlled synthetic route to develop functional nanostructure and also enables controlled organization of nanostructures, such as nanoclusters, freestanding monolayers, cross-linked nanoparticles etc. Bottom-up approach is highly promising in terms of attaining homogeneous compositions, less defects and no damage to the crystallographic orientations. Most extensively used process to obtain the desired thickness of nanomaterial thin films is through spin coating, where the colloidal dispersion is cast over the substrate and is spun at a specific speed and time. Spray pyrolysis, blade coating, dip-coating are some other techniques, which are popularly used for thin film formation.

1.5 Thin Film Transistors

A typical transistor is a three terminal device, where current flows from the source electrode (terminal 1) to the drain electrode (terminal 2) through a thin semiconducting layer, which is controlled by voltage at the gate electrode (terminal 3). A schematic representation of a thin film transistor is shown in **Figure 1.5a**. The semiconducting transport layer is separated from the gate electrode by a gate dielectric layer. This dielectric layer can be made of inorganic insulator such as SiO_2, Al_2O_3, or insulating polymer such as poly(methyl methacrylate)(PMMA) or poly(4-vinylphenol) (PVP) depending on the transistor structure. The source and the drain terminals are generally fabricated using metals such as Au, Ag, Pt etc. The fundamental operation regimes of a thin film transistor at different biasing conditions are illustrated in **Figure 1.5b, c and d**. In the figure, V_g and V_d correspond to gate to source voltage and drain to source voltage, respectively, where the source terminal is normally grounded.

Condition 1: At $V_g=V_{th}$, Vs=0V, $V_d<V_g-V_{th}$: At positive gate bias voltage, negatively charged electrons will accumulate at the semiconductor/gate dielectric interface when no potential is applied across the source and the drain terminals. Whereas, when negative potential is applied at the gate terminal, holes (positive charges) will get accumulated at the interface. At this condition, the carrier concentration remains uniform throughout the channel. However, all the accumulated charges are not mobile and some charges get trapped in the deep trap states. So, a voltage higher than threshold voltage (V_{th}) is required at the gate terminal for charge accumulation. The threshold voltage of a transistor is determined by the dielectric used and built-in-dipoles, interfacial traps and impurities. When $V_d < V_g-V_{th}$ a linear gradient of charge density is established from source to drain and the current flowing through the channel is directly proportional to the drain voltage (**Figure 1.5b**) and this regime of operation is termed as linear region. Considering gradual channel approximations, current flowing through the channel in the linear regime can be written as-

$$I_d = \frac{W}{L}\mu_{linear}C_i(V_g - V_{th})V_{ds} \qquad \textbf{1.2}$$

Differentiating the above equation, with respect to V_g, the carrier mobility in the linear regime can be obtained as –

$$\mu_{lin} = \frac{\delta I_{ds}}{\delta V_g} . \frac{L}{W C_i V_{ds}} \qquad \textbf{1.3}$$

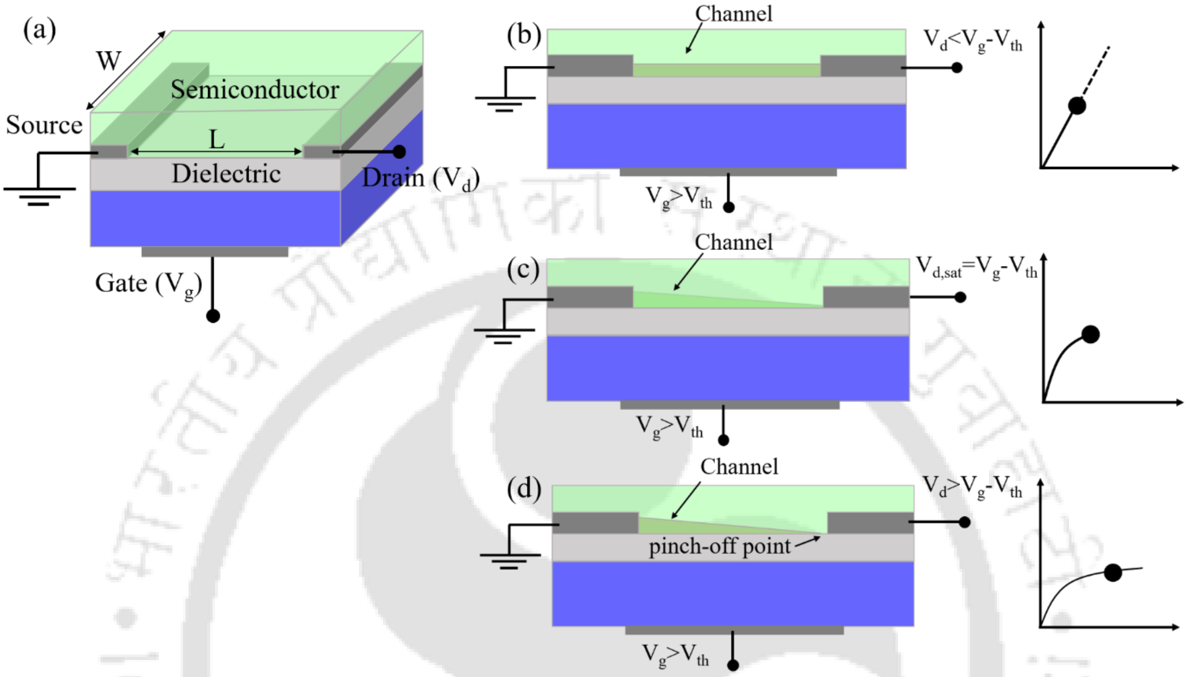

Figure 1.5. Schematic representation of thin film transistors at different operating conditions.

Condition 2: $V_g=V_{th}$, $V_d= V_g-V_{th}$: When $V_d =V_g-V_{th}$, the channel is pinched off and a depletion region is formed near the drain end (**Figure 1.5c**).

Condition 3: $V_g=V_{th}$, $V_d> V_g-V_{th}$: On further increasing the voltage, from the pinch off region, the drain current saturates and no substantial increase in the drain current could be observed (**Figure 1.5d**).[32] The saturation current and carrier mobility at saturation can be expressed as equations 1.4, 1.5 respectively.

$$I_d(sat) = \frac{W}{2L} \mu_{sat} C_i (V_g - V_{th})^2 \qquad \textbf{1.4}$$

$$\mu_{sat} = \frac{\delta I_{ds}(sat)}{\delta V_g} . \frac{L}{W C_i (V_g - V_{th})} \qquad \textbf{1.5}$$

The switching characteristics of a transistor is determined by the ratio of drain current in ON state and the OFF state (I_{on}/I_{off}) and a high value is desired for efficient performance. The ON state drain current is determined by the carrier mobility within the semiconductor and the dielectric capacitance, whereas the gate leakage current determines the OFF state current.[32] Thin film transistors are fabricated in different architectures namely, top contact/bottom gate (TC/TG), bottom contact/bottom gate (BC/BG) and bottom contact/top gate (BC/TG). Lithographic techniques and shadow masks are used to deposit the electrodes/metal contacts of the transistor. The polarity of the accumulated charges at the channel describes the type of the transistor, which can be influenced and altered by impurity doping or through ligand interaction with the channel material. For instance, ambipolar nature of PbS Qdot thin film transistor is modulated to n-type by doping n-type benzyl viologen molecules with the help of crosslinking ligands, such as 3MPA, TBAI and MAI.[33] In another report, post-synthetic treatment of CdSe Qdots with halide compounds (InX, X=Cl, Br, I) have exhibited effective n-type doping and surface passivation and high carrier mobility and I_{on}/I_{off} ratio were obtained due to effective electronic coupling between the Qdots.[34] Moreover, stoichiometrically controlled S-rich PbS Qdots based FET was demonstrated, which showed a strong hole transport characteristics and their potential towards optoelectronic devices was illustrated.[35]

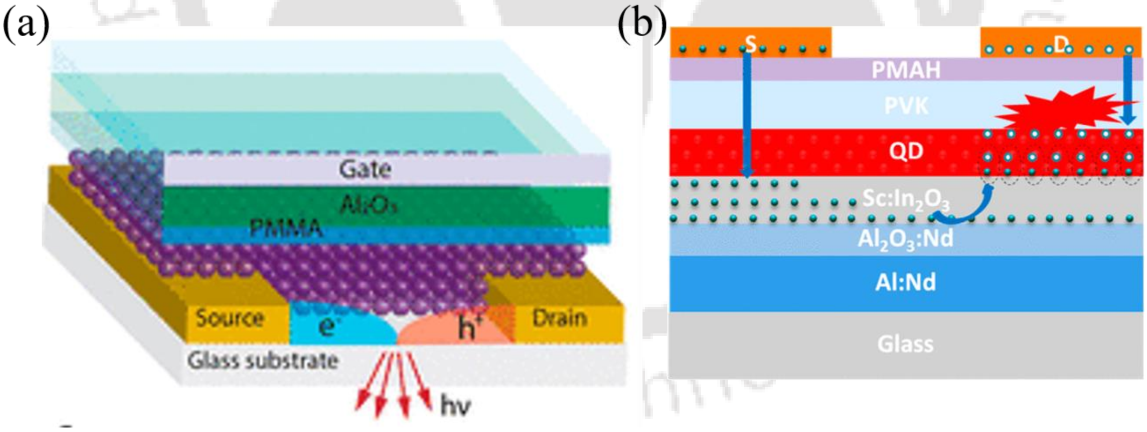

Figure 1.6. (a) Schematic representation of Qdot LEFET. (Reprinted with permission from reference 38. Copywrite 2018 ACS). (b) Schematic representation of multi-layered vertical LEFET. (Reprinted with permission from reference 39. Copywrite 2018 American Chemical Society).

In optoelectronics, light emission and electronic switching are two key functions, which are performed separately by light emitting diodes and transistors, respectively. If these two functions could be performed by a single device, it would not only give us an easy approach for miniaturization and high density integration, but also would reduce the cost of production and power consumption. In this regard, light emitting field effect transistors (LEFET) have caught significant interest, which is an intelligent approach of embedding switching operation and light emission in a single device. These bi-functional feature of LEFET make them interesting for high density integration of devices in next generation electronics.[36] As for example, PbS Qdots have been used as an active emissive material, where ionic gel electrolyte gate was employed to increase the current density and hence improved external quantum efficiency.[37]

In another report, solid gated LEFET from PbS Qdots treated with tetrabutylammonium iodide (TBAI) was fabricated, where state of the art near infrared emission was obtained (**Figure 1.6a**).[38] One of the prerequisites for LEFETs to function is to have ambipolar transport characteristics since light emission involves recombination of electrons and holes. Therefore, it is necessary to choose a channel material that supports transport of both type of carriers. In addition to this, the channel material should also be an efficient emitter.[36] A hybrid Qdot LEFET was demonstrated recently, where high luminescent Qdots and solution processed scandium-indium oxide ($Sc:In_2O_3$) semiconductor were vertically aligned and a bright electroluminescence was observed.[39] Here, To equilibrate the electron and hole concentrations, the $Sc:In_2O_3$ layer was employed as the electron transport layer (**Figure 1.6b**).

1.6 Photodetectors

Photodetectors, which translate optical energy to electrical signals are used as key components in a range of multifunctional technologies. Owing to the versatility, they are dedicatedly used in smart technologies, night vision systems, defence security and optical communications. Photoconductivity involves three successive processes, namely generation of excitons (electron hole pairs) due to absorption of incident photon, separation of the charge carriers to the excited state (conduction band) and transport of these carriers to external electrodes. The efficiency of a detector is dependent on several key parameters, such as, absorption coefficient of the active material, carrier trapping and recombination dynamics. With the advancement of nanoscale devices, these criteria could precisely be controlled, which not only led to improved device performance but also met the demands of achieving narrow and specific detection bands, fast response rate, wider detection range and compatibility with flexible device. As for example, ZnO, MgZnO, GaN, Ga_2O_3, ZnS nanocrystals are promising photoactive material for solar blind ultraviolet detection owing to their wide band gap.[40-42] On the contrary, narrow bandgap Qdots such as PbS, PbSe are suitable for infrared detection.[40, 43] Two-dimensional transition metal dichalcogenides (2-D TMD), such as MoS_2, BP and WS_2, having outstanding carrier transport capabilities and strong light- matter interactions, are considered promising alternatives for entire visible as well as some NIR range detection.[40] In comparison to single component detectors, hybrid structures comprising of TMD and photosensitive Qdot exhibit better figure of merit characteristics, such as enhanced photoresponsivity and faster transients. In heterostructured devices, the band levels of TMD and Qdot are aligned in such a way that, p-n heterojunctions, or Schottky junctions develop at the TMD/semiconductor interface, which facilitates charge transfer to improve detector performance.[40] A recent report demonstrated vertically grown MoS_2 nanosheets and p-GaN nanorod heterostructure that exhibited broad spectral detection with promising optical gain in the visible band.[44] Thus, numerous permutations of band alignments possible with the integration of 2D, 1D and 0D nanostructures provide us with potential directions to design and construct novel and commercially viable next generation photodetectors.

1.6.1 Self-Powered Photodetectors

With the growing demands for portable electronic devices, energy consumption by the devices is the main concern and thus the focus is drawn significantly towards low power or no power systems. Uninterrupted functioning of devices in critical environments demands continuous supply of power and thus increases cost of operation and system complexity. Therefore, self-powered devices are the solution to low cost, light weight, pollution free, renewable and sustainable energy sources. In this regard, self-powered detectors have become the research hotspot for zero-powered miniature and flexible technology.

The carrier generation and fundamental charge transfer mechanisms in photodetectors are predominantly determined by the band alignments. In order to expand detection range, and to enhance the responsivity and the response time, various types of heterojunctions, p-n junctions, p-i-n junctions, organic/inorganic junctions and Schottky junctions are realised.

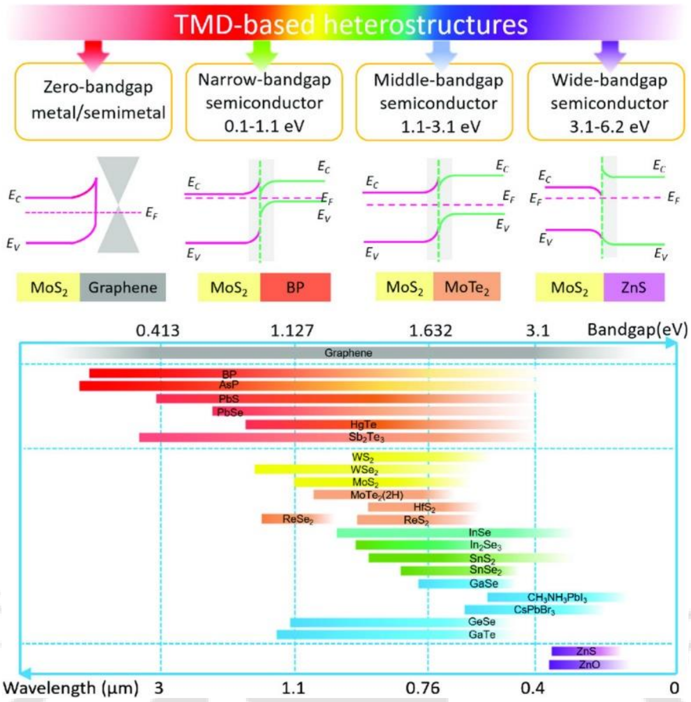

Figure 1.7. Schematic representation of band alignments of zero, narrow, mid and wide bandgap materials with two dimensional MoS_2 layer. (Reprinted with permission from reference 40. Copywrite 2021 John Wiley and Sons).

In comparison to individual photoactive material, hetero-structured designs create built-in electric field due to alignments of individual fermi levels. The difference in the fermi levels enhances the carrier transport and thus increases the photocurrent efficiency at zero bias condition. Two dimensional thin films are brought into hetero-structured photodetector designs with zero bandgap (eg. graphene), narrow bandgap (e.g., PbS Qdots, black phosphorous), mid bandgap (eg. $MoTe_2$) and wide bandgap (eg. ZnS, β-Ga_2O_3, GaN) materials to address the photodetection from UV region to IR region.[40] A representative schematic of band alignments of materials having different band gaps are shown in **Figure 1.7**.

1.7 Tactile Sensors

As the world advances towards the era of artificial intelligence and internet of things, wearable devices have caught global attention and have largely been accepted as physical assistive devices that can produce user interactive information. Such wearable sensors are used as health monitoring unit, artificial skin for robotic interfaces, motion sensors, voice recognition systems etc.[45-49] In this perspective, tactile sensors that can transduce mechanical deformations and physical stimuli to electrical signals, have laid new roadmaps towards diverse applicability as heart rate and breathing sequence monitors, gesture recognition systems, self-powered nanogenerators and pressure sensors, to name a few.[50-52] These sensors can detect external stimuli such as torsion, bending, friction, vibration, pressure and transform these into analog electrical output allowing precise and effective measure of the stimuli.

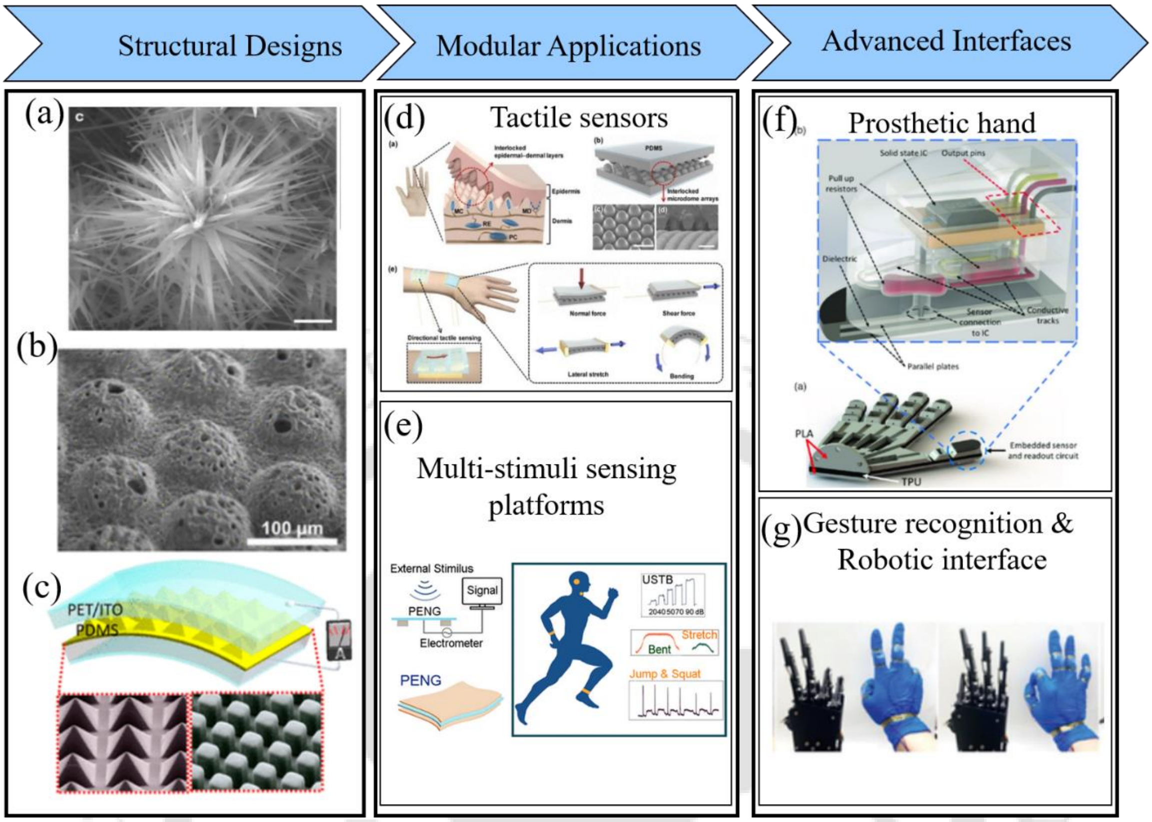

Figure 1.8. Examples of (a) nanostructured spines (Reprinted with permission from reference 54. Copywrite 2018 Nature Communications), (b) nanoporous and microridge structures (Reprinted with permission from reference 55. Copywrite 2018 American Chemical Society) and (c) lithographically patterned microstructures (Reprinted with permission from reference 56. Copywrite 2012 American Chemical Society) embodied in tactile sensors. (d) Tribo-electric effect based tactile sensor (Reprinted with permission from reference 55. Copywrite 2018 American Chemical Society), (e) multi-stimuli sensing platforms (Reprinted with permission from reference 45. Copywrite 2021 American Chemical Society), advanced interfaces such as (f) prosthetic hand (Reprinted with permission from reference 49. Copywrite 2020 John Wiley and Sons) and (g) gesture recognition systems (Reprinted with permission from reference 52. Copywrite 2022 John Wiley and Sons).

The tactile sensors are established upon piezoelectric, piezoresistive, piezocapacitive and triboelectic transduction mechanisms.[53] Surface topography and structural modifications play a crucial role in boosting such responses. Bio inspired nanostructured spines (**Figure 1.8a**),[54] nanoporous and microridge structures (**Figure 1.8b**),[55] lithographically patterned microstructures (**Figure 1.8c**)[56] are often embodied to increase surface roughness in order to increase contact area that plays a vital role in enhancing the efficiency. Such integrations are used as tactile sensors and multi-stimuli sensing platforms for monitoring human physiological conditions (**Figure 1.8d-e**).[45, 55] Tactile sensors are also used in advanced electronic interfaces such as in prosthetic hands and robotic interfaces as gesture recognition systems (**Figure 1.8f-g**).[49, 52]

1.7.1 Piezoelectric Tactile Sensors

Piezoelectric tactile sensors produce a quantitative measure of the external mechanical deformations in terms of change in piezoelectric potential. The piezoelectric effect originates from the displacement of the centres of cations and anions in non-centrosymmetric materials such as lead zirconate titanate (PZT),[57] gallium nitride (GaN)[58] or from the change in the direction of permanent dipole moment inside polymers like polyvinylidene fluoride (PVDF).[59] Polymer nanocomposits with nanoparticles are proven to be efficacious building blocks in designing such sensors. PVDF being a semi-crystalline polymer, exhibits excellent piezoelectric characteristics and has been extensively used with $BaTiO_3$, CNT and trifluoroethylene (TrFE) composites as piezoelectric sensors, voice recognition systems, ultrasound imaging and nanogenerators.[60-64]

1.7.2 Piezoresistive Tactile Sensors

Piezoresistive tactile sensors translate mechanical deformations into change in device resistance, that primarily rely on two major processes described by

$$R=\rho L/A \qquad \mathbf{1.6}$$

Where, ρ corresponds to the resistivity of the material and L corresponds to the length and A corresponds to the cross-sectional area of the sensor. The change in resistance of the device is dictated by the change in resistor geometry (L and A), where L increases and A decreases as a result of the Poisson effect when the resistor is stretched.[65] The second process is based on a change in the material's resistivity, which can be altered by changes in the system's energy band structure, quantum tunnelling, or percolation dynamics.[53]

1.7.3 Piezocapacitive Tactile Sensors

Piezocapacitive tactile sensors translate mechanical deformations into change in capacitance of the dielectric layer sandwiched between two parallel plate electrodes. For a parallel plate capacitor, capacitance C is represented by the following equation.

$$C = \frac{\varepsilon_r \varepsilon_0 A}{d} \quad \textbf{1.7}$$

Where, ε_r corresponds to relative permittivity of the dielectric material, ε_0 corresponds to permittivity of free space, A is the overlapping area between the electrodes and d is the distance between the electrodes. Changes in A contribute to the measurement of strain and shear forces whereas, changes in d estimate the forces in the perpendicular direction such as pressure.[66] Furthermore, incorporating nanostructures[67] and patterned microstructures[68] modulate ε_r targeted towards improving sensitivity and response time. Such sensors exhibit state of the art frequency responses and are responsive over a large dynamic range.

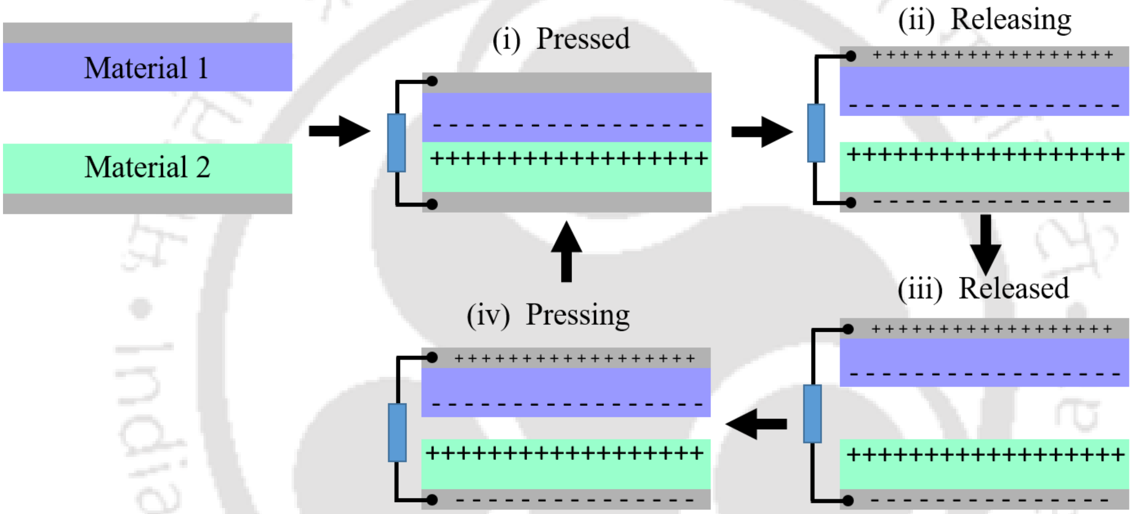

Figure 1.9. Working mechanism of triboelectric sensor.

1.7.4 Triboelectric Tactile Sensors

Triboelectric sensors convert mechanical energy to electrical energy, where triboelectric potentials are generated between two materials in contact by the conjunction of contact electrification and electrostatic induction. Difference in the triboelectric potential between two materials causes transfer of charges between them when in contact and induces opposite charges on the other side of the surfaces. When the surfaces are separated, the compensating charges accumulate that results in a current flow across the electrodes until an equilibrium is attained (**Figure 1.9**). Triboelectric sensors are designed upon flexible and stretchable polymers such as polytetrafluoroethylene,[69] nylon,[70] PDMS[71] and polyimide nanofibers membrane[72]. Nanomaterial composites and hybrid approaches introduce compelling features including broad range of material choice, biocompatibility, improved performance, wide detection range, multimode operation, multifunctional applicability etc.[73-77] Triboelectric nanogenerators were introduced in 2012 by Wang and group with the goal of harvesting mechanical energy to electricity. With this revolutionary idea, comprehensive studies have been carried out to generate electricity from mechanical deformations, wind energy, wave energy, physical activities like walking and running and are also proven to be promising towards smart sports facilities and self-powered wearable gadgets.[78-80]

In spite of excellent developments in the field of intelligent systems, there are still ample room for improvements before they are introduced in the marketplace. Each type of tactile sensors would have its advantages and disadvantages in terms of fabrication and efficienty and a balanced trade-off would make them viable for commercialization. They are susceptible to noise, hysteresis, undesired drift and are also sometimes accompanied with pyroelectric effects. To mimic human skin and to achieve dexterity in robotic interfaces, transparency, biocompatibility, biodegradability, self-healing capability, temperature and humidity are important attributes to be considered while designing a tactile sensor. Material compositions and their permutations along with structural designs would offer a number of options for innovations. Adding multifunctional attributes to a sensor would enhance its on-board intelligence that is capable of detecting specific parameters.

1.8 Perspectives and Outlook

Generally white light emissive devices contain optimised sequence of primary colour emitters, but such fabrication architectures are complex and results in colour instability. White light emission from a single component moiety is always desired to address these issues. With the insights from recent developments in surface complexed Qdots and their physical properties, there is merit in studying their charge carrier transport properties and engineering solid state electronic devices from them. It also provides ample opportunities to study photoexcited carrier generation and recombination dynamics due to transition metal ion doping and surface complexation reactions in Qdots and to fabricate photodetectors targeting specific detection band. Moreover, promising implications of ligand mediated nanoparticle assembly opens up wide arena for developing multi-stimuli and multifunctional flexible sensors.

1.9 Overview of the Current Dissertation

The focus of this dissertation work is to study the electronic properties of nanocrystals such as Qdots and nanoparticles and is targeted towards solid state device fabrication for potential applications in field effect transistors, photodetectors and tactile sensors.

Chapters:

1. A brief introduction was presented on nanomaterials, Qdots and their functional attributes. Different strategies of solid state device fabrication were discussed, where special focus was drawn towards applications such as transistors, photodetector and tactile sensors.
2. White light emitting Qdot complexes (QDC) were synthesised through surface complexation of Mn^{2+} doped ZnS Qdot via ligand interaction with 8-hydroxyquinoline 5 sulphonic acid and the photoluminescence properties were studied. Thin film transistors based on these QDCs were fabricated, where, charge transport characteristics and temperature dependent carrier hopping characteristics were studied.
3. Self-powered ultraviolet photodetectors were fabricated based on the above mentioned QDC, where a shift in the detection band from UVC in as-synthesised Qdot to UVA in surface complexed Qdot was observed. Qdot based UVC detector and QDC based UVA detector was integrated with a microcontroller unit and a portable prototype was demonstrated, where the responses were calibrated to selectively detect UVA and UVC.

Furthermore, the dual emissive property of QDC was utilised as anti-counterfeiting ink for data encryption and decryption.

4. Picolyleamine mediated gold nanoparticle (Au NP) network was synthesised and the piezo-resistive characteristics were explored. A multi-stimuli responsive tactile sensor was demonstrated, where triboelectric contact electrification between a lithographically patterned PDMS layer and the Au NP network enabled the device to respond to compressive and tensile strain, identify variable weight, tapping action and vibration. Physical activities such as jogging, leg movements and standing from sitting postures were recognised. The piezo-phototronic response of the device is another aspect that was explored and visible light detection under different bending angles were illustrated.
5. Finally, conclusions were drawn on the key findings of this dissertation work and insights on the future prospects were presented.

1.10 References

1. Zhan, C.; Chen, X.-J.; Huang, Y.-F.; Wu, D.-Y.; Tian, Z.-Q. Plasmon-Mediated Chemical Reactions on Nanostructures Unveiled by Surface-Enhanced Raman Spectroscopy. *Accounts of Chemical Research.* **2019**, 52, 2784-2792.

2. Miao, J.; Hu, W.; Jing, Y.; Luo, W.; Liao, L.; Pan, A.; Wu, S.; Cheng, J.; Chen, X.; Lu, W. Surface Plasmon-Enhanced Photodetection in Few Layer MoS2 Phototransistors with Au Nanostructure Arrays. *Small.* **2015**, 11, 2392-2398.

3. Thakur, M. K.; Fang, C.-Y.; Yang, Y.-T.; Effendi, T. A.; Roy, P. K.; Chen, R.-S.; Ostrikov, K. K.; Chiang, W.-H.; Chattopadhyay, S. Microplasma-Enabled Graphene Quantum Dot-Wrapped Gold Nanoparticles with Synergistic Enhancement for Broad Band Photodetection. *ACS Applied Materials & Interfaces.* **2020**, 12, 28550-28560.

4. Zhang, Z.; Zhang, C.; Zheng, H.; Xu, H. Plasmon-Driven Catalysis on Molecules and Nanomaterials. *Accounts of Chemical Research.* **2019**, 52, 2506-2515.

5. Zhang, Y.; He, S.; Guo, W.; Hu, Y.; Huang, J.; Mulcahy, J. R.; Wei, W. D. Surface-Plasmon-Driven Hot Electron Photochemistry. *Chemical Reviews.* **2018**, 118, 2927-2954.

6. Kim, D.; Kim, J.; Park, Y. I.; Lee, N.; Hyeon, T. Recent Development of Inorganic Nanoparticles for Biomedical Imaging. *ACS Central Science.* **2018**, 4, 324-336.

7. Saladino, G. M.; Vogt, C.; Li, Y.; Shaker, K.; Brodin, B.; Svenda, M.; Hertz, H. M.; Toprak, M. S. Optical and X-ray Fluorescent Nanoparticles for Dual Mode Bioimaging. *ACS Nano.* **2021**, 15, 5077-5085.

8. Abadeer, N. S.; Murphy, C. J. Recent Progress in Cancer Thermal Therapy Using Gold Nanoparticles. *The Journal of Physical Chemistry C.* **2016**, 120, 4691-4716.

9. Ginting, R. T.; Kaur, S.; Lim, D.-K.; Kim, J.-M.; Lee, J. H.; Lee, S. H.; Kang, J.-W. Plasmonic Effect of Gold Nanostars in Highly Efficient Organic and Perovskite Solar Cells. *ACS Applied Materials & Interfaces.* **2017**, 9, 36111-36118.

10. Huang, C.-B.; Yao, Y.; Montes-García, V.; Stoeckel, M.-A.; Von Holst, M.; Ciesielski, A.; Samorì, P. Highly Sensitive Strain Sensors Based on Molecules–Gold Nanoparticles Networks for High-Resolution Human Pulse Analysis. *Small.* **2021**, 17, 2007593.

11. Olichwer, N.; Leib, E. W.; Halfar, A. H.; Petrov, A.; Vossmeyer, T. Cross-Linked Gold Nanoparticles on Polyethylene: Resistive Responses to Tensile Strain and Vapors. *ACS Applied Materials & Interfaces.* **2012**, 4, 6151-6161.

12. Ketelsen, B.; Yesilmen, M.; Schlicke, H.; Noei, H.; Su, C.-H.; Liao, Y.-C.; Vossmeyer, T. Fabrication of Strain Gauges via Contact Printing: A Simple Route to Healthcare Sensors Based on Cross-Linked Gold Nanoparticles. *ACS Applied Materials & Interfaces.* **2018**, 10, 37374-37385.

13. Yang, Z.; Wang, D.-Y.; Pang, Y.; Li, Y.-X.; Wang, Q.; Zhang, T.-Y.; Wang, J.-B.; Liu, X.; Yang, Y.-Y.; Jian, J.-M.; Jian, M.-Q.; Zhang, Y.-Y.; Yang, Y.; Ren, T.-L. Simultaneously Detecting Subtle and Intensive Human Motions Based on a Silver Nanoparticles Bridged Graphene Strain Sensor. *ACS Applied Materials & Interfaces.* **2018**, 10, 3948-3954.

14. Brus, L. E. Electron–electron and electron-hole interactions in small semiconductor crystallites: The size dependence of the lowest excited electronic state. *The Journal of Chemical Physics.* **1984**, 80, 4403-4409.

15. Rogach, A. L.; Talapin, D. V.; Shevchenko, E. V.; Kornowski, A.; Haase, M.; Weller, H. Organization of Matter on Different Size Scales: Monodisperse Nanocrystals and Their Superstructures. *Advanced Functional Materials.* **2002**, 12, 653-664.

16. Pu, C.; Qin, H.; Gao, Y.; Zhou, J.; Wang, P.; Peng, X. Synthetic Control of Exciton Behavior in Colloidal Quantum Dots. *Journal of the American Chemical Society.* **2017**, 139, 3302-3311.

17. Cao, S.; Zhao, J.; Yang, W.; Li, C.; Zheng, J. Mn2+-doped Zn–In–S quantum dots with tunable bandgaps and high photoluminescence properties. *Journal of Materials Chemistry C.* **2015**, 3, 8844-8851.

18. Brus, L. Electronic wave functions in semiconductor clusters: experiment and theory. *The Journal of Physical Chemistry.* **1986**, 90, 2555-2560.

19. Pandey, A.; Sarma, D. D. Recent Advances in Manganese Doped II-VI Semiconductor Quantum Dots. *Zeitschrift für anorganische und allgemeine Chemie.* **2016**, 642, 1331-1339.

20. Sotelo-Gonzalez, E.; Roces, L.; Garcia-Granda, S.; Fernandez-Arguelles, M. T.; Costa-Fernandez, J. M.; Sanz-Medel, A. Influence of Mn2+ concentration on Mn2+-doped ZnS quantum dot synthesis: evaluation of the structural and photoluminescent properties. *Nanoscale.* **2013**, 5, 9156-9161.

21. Begum, R.; Chattopadhyay, A. Redox-Tuned Three-Color Emission in Double (Mn and Cu) Doped Zinc Sulfide Quantum Dots. *The Journal of Physical Chemistry Letters.* **2014**, 5, 126-130.

22. Jin, Y.-R.; Liu, Y.; Jiang, F.-L. Positive Sorption Behaviors in the Ligand Exchanges for Water-Soluble Quantum Dots and a Strategy for Specific Targeting. *ACS Applied Materials & Interfaces.* **2021**, 13, 51746-51758.

23. Jiang, S.; Song, Y.; Kang, H.; Li, B.; Yang, K.; Xing, G.; Yu, Y.; Li, S.; Zhao, P.; Zhang, T. Ligand Exchange Strategy to Achieve Chiral Perovskite Nanocrystals with a High Photoluminescence Quantum Yield and Regulation of the Chiroptical Property. *ACS Applied Materials & Interfaces.* **2022**, 14, 3385-3394.

24. Lin, Q.; Yun, H. J.; Liu, W.; Song, H.-J.; Makarov, N. S.; Isaienko, O.; Nakotte, T.; Chen, G.; Luo, H.; Klimov, V. I.; Pietryga, J. M. Phase-Transfer Ligand Exchange of Lead Chalcogenide Quantum Dots for Direct Deposition of Thick, Highly Conductive Films. *Journal of the American Chemical Society.* **2017**, 139, 6644-6653.

25. Sun, B.; Vafaie, M.; Levina, L.; Wei, M.; Dong, Y.; Gao, Y.; Kung, H. T.; Biondi, M.; Proppe, A. H.; Chen, B.; Choi, M.-J.; Sagar, L. K.; Voznyy, O.; Kelley, S. O.; Laquai, F.; Lu, Z.-H.; Hoogland, S.;

García de Arquer, F. P.; Sargent, E. H. Ligand-Assisted Reconstruction of Colloidal Quantum Dots Decreases Trap State Density. *Nano Letters.* **2020**, 20, 3694-3702.

26. Liu, Z.; Janes, L. M.; Saniepay, M.; Beaulac, R. Charge Storage and Quantum Confinement Resilience in Colloidal Indium Nitride Nanocrystals. *Chemistry of Materials.* **2018**, 30, 5435-5443.

27. Paek, K.; Yang, H.; Lee, J.; Park, J.; Kim, B. J. Efficient Colorimetric pH Sensor Based on Responsive Polymer–Quantum Dot Integrated Graphene Oxide. *ACS Nano.* **2014**, 8, 2848-2856.

28. Roy, S.; Bhandari, S.; Manna, M.; De, S.; Chattopadhyay, A. The nature of binding of quinolate complex on the surface of ZnS quantum dots. *Physical Chemistry Chemical Physics.* **2019**, 21, 589-596.

29. Bhandari, S.; Roy, S.; Pramanik, S.; Chattopadhyay, A. Chemical Reactions Involving the Surface of Metal Chalcogenide Quantum Dots. *Langmuir.* **2019**, 35, 14399-14413.

30. Pramanik, S.; Roy, S.; Mondal, A.; Bhandari, S. A two-target responsive reversible ratiometric pH nanoprobe: a white light emitting quantum dot complex. *Chemical Communications.* **2019**, 55, 4331-4334.

31. Bhandari, S.; Pramanik, S.; Khandelia, R.; Chattopadhyay, A. Gold Nanocluster and Quantum Dot Complex in Protein for Biofriendly White-Light-Emitting Material. *ACS Applied Materials & Interfaces.* **2016**, 8, 1600-1605.

32. Zaumseil, J.; Sirringhaus, H. Electron and Ambipolar Transport in Organic Field-Effect Transistors. *Chemical Reviews.* **2007**, 107, 1296-1323.

33. Nugraha, M. I.; Kumagai, S.; Watanabe, S.; Sytnyk, M.; Heiss, W.; Loi, M. A.; Takeya, J. Enabling Ambipolar to Heavy n-Type Transport in PbS Quantum Dot Solids through Doping with Organic Molecules. *ACS Applied Materials & Interfaces.* **2017**, 9, 18039-18045.

34. Lee, W. S.; Kang, Y. G.; Woo, H. K.; Ahn, J.; Kim, H.; Kim, D.; Jeon, S.; Han, M. J.; Choi, J.-H.; Oh, S. J. Designing High-Performance CdSe Nanocrystal Thin-Film Transistors Based on Solution Process of Simultaneous Ligand Exchange, Trap Passivation, and Doping. *Chemistry of Materials.* **2019**, 31, 9389-9399.

35. Bederak, D.; Dirin, D. N.; Sukharevska, N.; Momand, J.; Kovalenko, M. V.; Loi, M. A. S-Rich PbS Quantum Dots: A Promising p-Type Material for Optoelectronic Devices. *Chemistry of Materials.* **2021**, 33, 320-326.

36. Kahmann, S.; Shulga, A.; Loi, M. A. Quantum Dot Light-Emitting Transistors—Powerful Research Tools and Their Future Applications. *Advanced Functional Materials.* **2020**, 30, 1904174.

37. Schornbaum, J.; Zakharko, Y.; Held, M.; Thiemann, S.; Gannott, F.; Zaumseil, J. Light-Emitting Quantum Dot Transistors: Emission at High Charge Carrier Densities. *Nano Letters.* **2015**, 15, 1822-1828.

38. Shulga, A. G.; Kahmann, S.; Dirin, D. N.; Graf, A.; Zaumseil, J.; Kovalenko, M. V.; Loi, M. A. Electroluminescence Generation in PbS Quantum Dot Light-Emitting Field-Effect Transistors with Solid-State Gating. *ACS Nano.* **2018**, 12, 12805-12813.

39. He, P.; Jiang, C.; Lan, L.; Sun, S.; Li, Y.; Gao, P.; Zhang, P.; Dai, X.; Wang, J.; Peng, J.; Cao, Y. High-Performance, Solution-Processed Quantum Dot Light-Emitting Field-Effect Transistors with a Scandium-Incorporated Indium Oxide Semiconductor. *ACS Nano.* **2018**, 12, 4624-4629.

40. Liu, R.; Wang, F.; Liu, L.; He, X.; Chen, J.; Li, Y.; Zhai, T. Band Alignment Engineering in Two-Dimensional Transition Metal Dichalcogenide-Based Heterostructures for Photodetectors. *Small Structures.* **2021**, 2, 2000136.

41. Premkumar, S.; Nataraj, D.; Bharathi, G.; Ramya, S.; Thangadurai, T. D. Highly Responsive Ultraviolet Sensor Based on ZnS Quantum Dot Solid with Enhanced Photocurrent. *Scientific Reports.* **2019**, 9, 18704.

42. Wu, C.; He, C.; Guo, D.; Zhang, F.; Li, P.; Wang, S.; Liu, A.; Wu, F.; Tang, W. Vertical α/β-Ga2O3 phase junction nanorods array with graphene-silver nanowire hybrid conductive electrode for high-performance self-powered solar-blind photodetectors. *Materials Today Physics.* **2020**, 12, 100193.

43. Tang, H.; Zhong, J.; Chen, W.; Shi, K.; Mei, G.; Zhang, Y.; Wen, Z.; Müller-Buschbaum, P.; Wu, D.; Wang, K.; Sun, X. W. Lead Sulfide Quantum Dot Photodetector with Enhanced Responsivity through a Two-Step Ligand-Exchange Method. *ACS Applied Nano Materials.* **2019**, 2, 6135-6143.

44. Yang, G.; Gu, Y.; Yan, P.; Wang, J.; Xue, J.; Zhang, X.; Lu, N.; Chen, G. Chemical Vapor Deposition Growth of Vertical MoS2 Nanosheets on p-GaN Nanorods for Photodetector Application. *ACS Applied Materials & Interfaces.* **2019**, 11, 8453-8460.

45. Huang, X.; Qin, Q.; Wang, X.; Xiang, H.; Zheng, J.; Lu, Y.; Lv, C.; Wu, K.; Yan, L.; Wang, N.; Xia, C.; Wang, Z. L. Piezoelectric Nanogenerator for Highly Sensitive and Synchronous Multi-Stimuli Sensing. *ACS Nano.* **2021**, 15, 19783-19792.

46. Zhao, P.; Zhang, R.; Tong, Y.; Zhao, X.; Zhang, T.; Tang, Q.; Liu, Y. Strain-Discriminable Pressure/Proximity Sensing of Transparent Stretchable Electronic Skin Based on PEDOT:PSS/SWCNT Electrodes. *ACS Applied Materials & Interfaces.* **2020**, 12, 55083-55093.

47. Guo, T.-M.; Gong, Y.-J.; Li, Z.-G.; Liu, Y.-M.; Li, W.; Li, Z.-Y.; Bu, X.-H. A New Hybrid Lead-Free Metal Halide Piezoelectric for Energy Harvesting and Human Motion Sensing. *Small.* n/a, 2103829.

48. Dinh Le, T.-S.; An, J.; Huang, Y.; Vo, Q.; Boonruangkan, J.; Tran, T.; Kim, S.-W.; Sun, G.; Kim, Y.-J. Ultrasensitive Anti-Interference Voice Recognition by Bio-Inspired Skin-Attachable Self-Cleaning Acoustic Sensors. *ACS Nano.* **2019**, 13, 13293-13303.

49. Ntagios, M.; Nassar, H.; Pullanchiyodan, A.; Navaraj, W. T.; Dahiya, R. Robotic Hands with Intrinsic Tactile Sensing via 3D Printed Soft Pressure Sensors. *Advanced Intelligent Systems.* **2020**, 2, 1900080.

50. Xu, Q.; Gao, X.; Zhao, S.; Liu, Y.-N.; Zhang, D.; Zhou, K.; Khanbareh, H.; Chen, W.; Zhang, Y.; Bowen, C. Construction of Bio-Piezoelectric Platforms: From Structures and Synthesis to Applications. *Advanced Materials.* **2021**, 33, 2008452.

51. Park, D. Y.; Joe, D. J.; Kim, D. H.; Park, H.; Han, J. H.; Jeong, C. K.; Park, H.; Park, J. G.; Joung, B.; Lee, K. J. Self-Powered Real-Time Arterial Pulse Monitoring Using Ultrathin Epidermal Piezoelectric Sensors. *Advanced Materials.* **2017**, 29, 1702308.

52. Tao, K.; Chen, Z.; Yu, J.; Zeng, H.; Wu, J.; Wu, Z.; Jia, Q.; Li, P.; Fu, Y.; Chang, H.; Yuan, W. Ultra-Sensitive, Deformable, and Transparent Triboelectric Tactile Sensor Based on Micro-Pyramid Patterned Ionic Hydrogel for Interactive Human–Machine Interfaces. *Advanced Science.* n/a, 2104168.

53. Wang, C.; Dong, L.; Peng, D.; Pan, C. Tactile Sensors for Advanced Intelligent Systems. *Advanced Intelligent Systems.* **2019**, 1, 1900090.

54. Yin, B.; Liu, X.; Gao, H.; Fu, T.; Yao, J. Bioinspired and bristled microparticles for ultrasensitive pressure and strain sensors. *Nature Communications.* **2018**, 9, 5161.

55. Ha, M.; Lim, S.; Cho, S.; Lee, Y.; Na, S.; Baig, C.; Ko, H. Skin-Inspired Hierarchical Polymer Architectures with Gradient Stiffness for Spacer-Free, Ultrathin, and Highly Sensitive Triboelectric Sensors. *ACS Nano.* **2018**, 12, 3964-3974.

56. Fan, F.-R.; Lin, L.; Zhu, G.; Wu, W.; Zhang, R.; Wang, Z. L. Transparent Triboelectric Nanogenerators and Self-Powered Pressure Sensors Based on Micropatterned Plastic Films. *Nano Letters.* **2012**, 12, 3109-3114.

57. Jiang, L.; Yang, Y.; Chen, R.; Lu, G.; Li, R.; Li, D.; Humayun, M. S.; Shung, K. K.; Zhu, J.; Chen, Y.; Zhou, Q. Flexible piezoelectric ultrasonic energy harvester array for bio-implantable wireless generator. *Nano Energy.* **2019**, 56, 216-224.

58. Tsai, S.-J.; Lin, C.-Y.; Wang, C.-L.; Chen, J.-W.; Chen, C.-H.; Wu, C.-L. Efficient coupling of lateral force in GaN nanorod piezoelectric nanogenerators by vertically integrated pyramided Si substrate. *Nano Energy*. **2017**, 37, 260-267.

59. Tian, G.; Deng, W.; Gao, Y.; Xiong, D.; Yan, C.; He, X.; Yang, T.; Jin, L.; Chu, X.; Zhang, H.; Yan, W.; Yang, W. Rich lamellar crystal baklava-structured PZT/PVDF piezoelectric sensor toward individual table tennis training. *Nano Energy*. **2019**, 59, 574-581.

60. Jiang, J.; Tu, S.; Fu, R.; Li, J.; Hu, F.; Yan, B.; Gu, Y.; Chen, S. Flexible Piezoelectric Pressure Tactile Sensor Based on Electrospun BaTiO3/Poly(vinylidene fluoride) Nanocomposite Membrane. *ACS Applied Materials & Interfaces*. **2020**, 12, 33989-33998.

61. Yang, C.; Song, S.; Chen, F.; Chen, N. Fabrication of PVDF/BaTiO3/CNT Piezoelectric Energy Harvesters with Bionic Balsa Wood Structures through 3D Printing and Supercritical Carbon Dioxide Foaming. *ACS Applied Materials & Interfaces*. **2021**, 13, 41723-41734.

62. Guan, X.; Xu, B.; Gong, J. Hierarchically architected polydopamine modified BaTiO3@P(VDF-TrFE) nanocomposite fiber mats for flexible piezoelectric nanogenerators and self-powered sensors. *Nano Energy*. **2020**, 70, 104516.

63. Li, B. M.; Ju, B.; Zhou, Y.; Knowles, C. G.; Rosenberg, Z.; Flewwellin, T. J.; Kose, F.; Jur, J. S. Airbrushed PVDF–TrFE Fibrous Sensors for E-Textiles. *ACS Applied Electronic Materials*. **2021**, 3, 5307-5326.

64. You, M.-H.; Wang, X.-X.; Yan, X.; Zhang, J.; Song, W.-Z.; Yu, M.; Fan, Z.-Y.; Ramakrishna, S.; Long, Y.-Z. A self-powered flexible hybrid piezoelectric–pyroelectric nanogenerator based on non-woven nanofiber membranes. *Journal of Materials Chemistry A*. **2018**, 6, 3500-3509.

65. Park, Y.; Chen, B.; Wood, R. J. Design and Fabrication of Soft Artificial Skin Using Embedded Microchannels and Liquid Conductors. *IEEE Sensors Journal*. **2012**, 12, 2711-2718.

66. Kwon, D.; Lee, T.-I.; Shim, J.; Ryu, S.; Kim, M. S.; Kim, S.; Kim, T.-S.; Park, I. Highly Sensitive, Flexible, and Wearable Pressure Sensor Based on a Giant Piezocapacitive Effect of Three-Dimensional Microporous Elastomeric Dielectric Layer. *ACS Applied Materials & Interfaces*. **2016**, 8, 16922-16931.

67. Wang, J.; Jiu, J.; Nogi, M.; Sugahara, T.; Nagao, S.; Koga, H.; He, P.; Suganuma, K. A highly sensitive and flexible pressure sensor with electrodes and elastomeric interlayer containing silver nanowires. *Nanoscale*. **2015**, 7, 2926-2932.

68. Yang, J.; Luo, S.; Zhou, X.; Li, J.; Fu, J.; Yang, W.; Wei, D. Flexible, Tunable, and Ultrasensitive Capacitive Pressure Sensor with Microconformal Graphene Electrodes. *ACS Applied Materials & Interfaces*. **2019**, 11, 14997-15006.

69. Wang, D. Y.; Zhang, D. Z.; Yang, Y.; Mi, Q.; Zhang, J. H.; Yu, L. D. Multifunctional Latex/Polytetrafluoroethylene-Based Triboelectric Nanogenerator for Self-Powered Organ-like MXene/Metal-Organic Framework-Derived CuO Nanohybrid Ammonia Sensor. *Acs Nano*. **2021**, 15, 2911-2919.

70. Qian, J.; He, J.; Qian, S.; Zhang, J.; Niu, X.; Fan, X.; Wang, C.; Hou, X.; Mu, J.; Geng, W.; Chou, X. A Nonmetallic Stretchable Nylon-Modified High Performance Triboelectric Nanogenerator for Energy Harvesting. *Advanced Functional Materials*. **2020**, 30, 1907414.

71. Yun, B. K.; Kim, J. W.; Kim, H. S.; Jung, K. W.; Yi, Y.; Jeong, M.-S.; Ko, J.-H.; Jung, J. H. Base-treated polydimethylsiloxane surfaces as enhanced triboelectric nanogenerators. *Nano Energy*. **2015**, 15, 523-529.

72. Kim, Y.; Wu, X.; Oh, J. H. Fabrication of triboelectric nanogenerators based on electrospun polyimide nanofibers membrane. *Scientific Reports*. **2020**, 10, 2742.

73. He, W.; Qian, Y.; Lee, B. S.; Zhang, F.; Rasheed, A.; Jung, J.-E.; Kang, D. J. Ultrahigh Output Piezoelectric and Triboelectric Hybrid Nanogenerators Based on ZnO

Nanoflakes/Polydimethylsiloxane Composite Films. *ACS Applied Materials & Interfaces*. **2018**, 10, 44415-44420.

74. Chowdhury, A. R.; Abdullah, A. M.; Hussain, I.; Lopez, J.; Cantu, D.; Gupta, S. K.; Mao, Y.; Danti, S.; Uddin, M. J. Lithium doped zinc oxide based flexible piezoelectric-triboelectric hybrid nanogenerator. *Nano Energy*. **2019**, 61, 327-336.

75. Meng, L.; Xu, Q.; Dan, L.; Wang, X. Single-Walled Carbon Nanotube Based Triboelectric Flexible Touch Sensors. *Journal of Electronic Materials*. **2019**, 48, 7411-7416.

76. Singh, H. H.; Khare, N. Flexible ZnO-PVDF/PTFE based piezo-tribo hybrid nanogenerator. *Nano Energy*. **2018**, 51, 216-222.

77. Ma, X.; Wang, C.; Wei, R.; He, J.; Li, J.; Liu, X.; Huang, F.; Ge, S.; Tao, J.; Yuan, Z.; Chen, P.; Peng, D.; Pan, C. Bimodal Tactile Sensor without Signal Fusion for User-Interactive Applications. *ACS Nano*. **2022**.

78. Zhang, J.; Sun, Y.; Yang, J.; Jiang, T.; Tang, W.; Chen, B.; Wang, Z. L. Irregular Wind Energy Harvesting by a Turbine Vent Triboelectric Nanogenerator and Its Application in a Self-Powered On-Site Industrial Monitoring System. *ACS Applied Materials & Interfaces*. **2021**, 13, 55136-55144.

79. Xu, Y.; Yang, W.; Lu, X.; Yang, Y.; Li, J.; Wen, J.; Cheng, T.; Wang, Z. L. Triboelectric Nanogenerator for Ocean Wave Graded Energy Harvesting and Condition Monitoring. *ACS Nano*. **2021**, 15, 16368-16375.

80. Luo, J.; Gao, W.; Wang, Z. L. The Triboelectric Nanogenerator as an Innovative Technology toward Intelligent Sports. *Advanced Materials*. **2021**, 33, 2004178.

Chapter 2

Charge Transport Characteristics of Surface Complexed Quantum Dot in a Thin Film Transistor

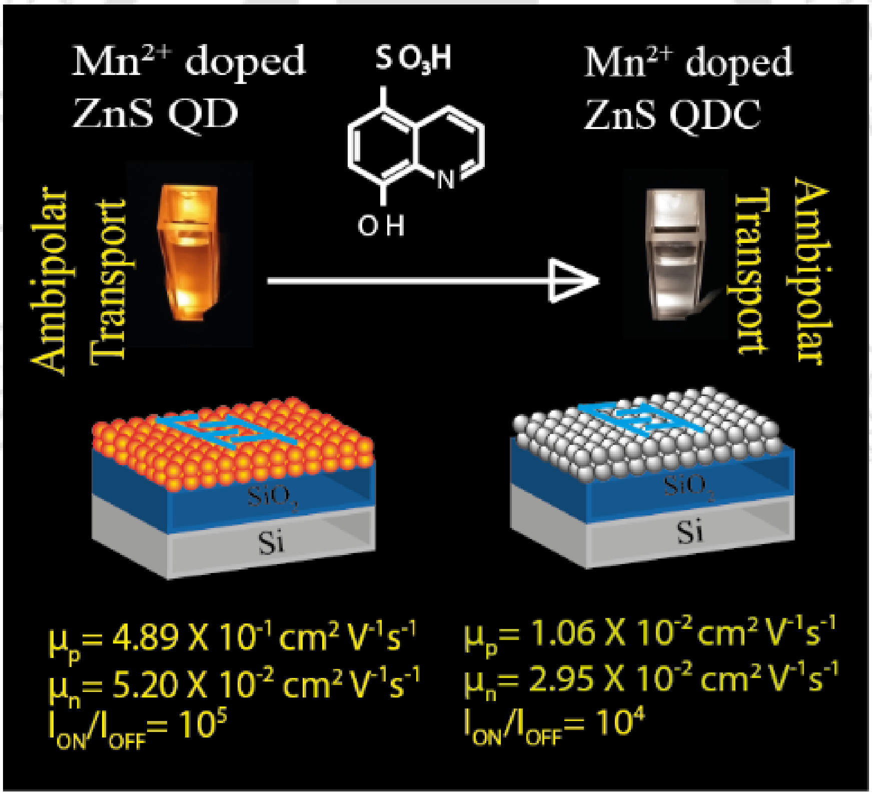

[K. Gogoi, S. Pramanik, A. Chattopadhyay, Advanced Materials Interfaces. 2020, 7, 1901665]

Chapter 2

Charge Transport Characteristics of Surface Complexed Quantum Dot in a Thin Film Transistor

Abstract

Abstract Ambipolar transport characteristics of thin film transistors fabricated from non-toxic white light emitting quantum dot complexes (QDC) are herein reported to exhibit efficient carrier mobilities. The QDC are synthesized by forming bluish green emitting zinc quinolate complex on the surface of orange emitting Mn^{2+} doped ZnS quantum dots (Qdots) using 8-hydroxyquinoline 5-sulphonic acid as the chelating ligand. The device exhibits efficient ambipolar transport characteristics with high I_{ON}/I_{OFF} ratio of 10^4 and electron mobility and hole mobility of 2.95×10^{-02} $cm^2V^{-1}s^{-1}$ and 1.06×10^{-02} $cm^2V^{-1}s^{-1}$, respectively. The Subthreshold Slope of QDC-TFT increases from that of Qdot-TFT from 0.35 $V.dec^{-1}$ to 0.79 $V.dec^{-1}$ in p-FET and 0.59 $V.dec^{-1}$ to 0.97 $V.dec^{-1}$ in n-FET operations, which annotates an increase in trap state density due to surface complexation of the Qdot. Our results suggest that white light emitting QDC can be used as an efficient transport as well as an emissive material, which would open up new paradigm for advanced optoelectronic applications.

2.1 Introduction

Light emitting thin film transistors (LETFT) have emerged as a promising candidate for the next generation electronics due to the dual integration of switching capacity of a transistor and light emission characteristics of a light emitting diode.[1-3] This unique characteristic of LETFT enhances its application potential in advanced electronics such as electric pump lasers,[4, 5] display pixels[6, 7] and optical communications.[8] High carrier mobilities, nature of trap states and carrier density are vital parameters for fabricating LETFT.[9] For light emitting devices, semiconductor material should possess high photoluminescence quantum yield as well as excellent carrier mobility and should also facilitate a balanced ambipolar conduction (both electron and hole conduction), which is crucial for efficient exciton recombination through radiative pathways.[5, 10] However, there is always a trade-off between carrier mobility and luminescence in case of organic semiconductors.[11] Colloidal semiconductor nanocrystal or quantum dots (Qdots) are reported to be excellent light emitters and have exhibited high charge transport capability.[12-15]

Importantly, Qdot integrated light emitting transistors are efficient in terms of both emissive and switching properties.[9, 13] However most of the devices are based on toxic metal chalcogenides such as PbS, PbSe and CdSe Qdots.[14, 16-18] These heavy metals cause adverse oxidative stress in human body.[19, 20] The toxic nature of these Qdots puts limitations to their practical usability and thus supports the development of environmentally benign ones. The principal bottleneck for the fabrication of devices using Qdots is single step deposition of high quality and defect free layer. Generally, Qdots capped with insulating long organic chains, induce a potential barrier to proficient charge transport and electronic coupling between Qdots in thin films and thus restrict their application in the field of electronics.[21] To reduce the interdot spacing and enhance the electronic coupling between the Qdots, a large number of surface modification strategies have been already employed and among them ligand exchange with halides,[22, 23] pseudohalides,[24, 25] chalogenides,[26] oxo-anion,[27] chalcogenideometallate complex and halometallates is popular. It has been established that the nature of the capping ligand controls the mobility of carriers and transport characteristics. Typically the type of ligand might influence the type of channel - whether n-type, p-type or ambipolar - in field effect transistors.[23, 28] The ambipolar nature of the transistor is due to near - intrinsic doping of the Qdot. Recently, tetrabutylammonium iodide (TBAI)-treated PbS Qdots,[13] metal chalcogenide complex ($Na_4Sn_2S_6·14H_2O$, $Na_4Sn_2Se_6$, and $KInSe_2$) capped CdSe Qdots[14] and 3-mercaptopropionic acid (MPA) ligand exchanged PbS Qdots[9] have been used in thin film transistors to achieve efficient charge transport and high carrier mobilities. However, ligand exchange with compact organic or inorganic ligands in Qdots do not always assure high carrier mobility and better charge transport in Qdots thin films. On the other hand, the ligand exchange may introduce additional trap states and recombination centres within the band gap of Qdots,[29] which may cause multiple trapping and release of carriers, resulting in low carrier mobilities in devices,[30] lower photoluminescent quantum yield (PLQY) and shift in emission wavelength.

In this context, recently introduced surface complexation of Qdots could provide a better option for enhancing the electronic coupling between Qdots and increase the electrical performance by inducing a conductive network in Qdots. Surface complexation i.e., the formation of luminescent inorganic complex(es) on the surface of a metal chalcogenide Qdot is a much simpler and cost-effective surface modification approach. It has been used for phase transfer of hydrophobic Qdots, targeted cellular imaging, pH sensing and fabrication of single component non-toxic white light emitting nanocomposite.[31-33] Recently, white light emitting (WLE) Qdots have gained intense interest in the context of replacing the existing WLE solid state devices. Pioneering researches in WLE devices have been implemented by multi-layered structures of individual primary color (blue, green, red) emitter nanocrystals. White colour emitter devices from single nanocrystals however offer numerous advantages over multiple emitter devices, such as reduced self-absorption, deviation from the chromaticity colour coordinates and non-radiative decay processes.[34] Therefore, it will be of substantial significance to study the charge transport behaviour, carrier mobility and defect state dynamics in white light emitting single component nanomaterials in the perspective of developing light emitting transistors.

Herein, bluish green emitting zinc quinolate complex has been synthesised on the surface of orange emitting Mn^{2+} doped ZnS Qdot by using 8-hydroxyquinoline-5-sulfonic acid (HQS) as chelating agent in order to fabricate a single component white light emitting (WLE) QDC. These WLE QDCs were incorporated in a bottom gate/top contact structured thin film transistor to study the charge transport characteristics in nano-structured thin films. It was found that the Qdot complex integrated thin film transistor (QDC-TFT) exhibited ambipolar transport characteristics with hole mobility and electron mobility of 1.06×10^{-02} $cm^2.V^{-1}.s^{-1}$ and 2.95×10^{-02} $cm^2.V^{-1}.s^{-1}$ respectively and an I_{ON}/I_{OFF} ratio of 10^4. The transport characteristics and subthreshold trap states of this device was compared with Mn^{2+} doped ZnS Qdot integrated thin film transistor (Qdot-TFT). The subthreshold slopes increased from 0.35 $V.dec^{-1}$ in Qdot-TFT to 0.79 $V.dec^{-1}$ in QDC-TFT in p-FET operation and 0.59 $V.dec^{-1}$ to 0.97 $V.dec^{-1}$ in n-FET operations, which suggest that additional carrier trap states were created because of surface complexation.

2.2 Materials and Methods

Materials: 8-Hydroxyquinoline-5-sulfonic acid (HQS, Merck), zinc acetate dihydrate (99%, Merck), manganese acetate tetrahydrate (99%, Merck), sodium sulphide (58%, Merck), methanol (Merck) and Mili-Q grade water were used for all synthesis and other experiments.

Synthesis of Mn^{+2} doped ZnS quantum dots: Water-soluble Mn^{2+} doped ZnS colloidal quantum dots (Qdots) having orange coloured (580 nm) emission were synthesized and purified in aqueous medium using a previously reported method.[35-38] Typically, a mixture of 1 mM solution of manganese acetate tetrahydrate and 5.0 mM solution of zinc acetate dihydrate was continuously stirred in aqueous medium at 80 - 90 ^{0}C. To this reaction mixture, 5.0 mM solution of sodium sulphide was added after 5 min of constant stirring. The reaction mixture was kept in reflux condition for 3 h at 120 ^{0}C. The colloidal dispersion thus obtained was centrifuged at 15000 rpm for 20 min and the resultant pellet was dispersed and sonicated in 50 mL Mili-Q water. Another cycle of centrifugation and sonication was performed to remove the unreacted precursor materials and to obtain a purer form of Mn^{+2} doped ZnS Qdot pellet. The pellet thus obtained after two cycles of centrifugation and redispersion was then dispersed in 50 mL methanol and the colloidal dispersion was used for further experiments.

Preparation of ligand solution: To prepare 1 mM HQS solution, a mixture of 6 mL water and 4 mL methanol was prepared to which 2.24 mg of pure 8-hydroxyquinoline-5 sulphonic acid (HQS) was added and the mixture was then ultrasonicated for 5 min.

Synthesis of quantum dot complex (QDC): For the synthesis of QDC, 3 μL of as prepared 1.0 mM HQS solution was added sequentially to 3.0 mL of as synthesised Mn^{+2} doped ZnS Qdot dispersion. The photoluminescence spectrum of Qdot was recorded on sequential addition of HQS ligand and optimal quantity of HQS ligand required for the formation of white light emitting QDC was examined. The optimum amount of HQS ligand required for the formation of QDC was ascertained to be 5.96 μM in 3.0 mL of Qdot dispersion. The resultant colloidal dispersion was centrifuged at 15000 rpm for 20 min. The pellet thus obtained was redispersed in methanol followed by another round of centrifugation and redispersion to obtain purified QDC. UV-Visible spectroscopy, powder X-ray diffraction, transmission electron microscopy, were also performed on the QDC to ascertain its formation.

Fabrication of thin film transistor: A highly doped p-type silicon with 300 nm thick SiO_2 dielectric was used as a substrate for device fabrication. The substrate was ultrasonically cleaned successively with acetone, isopropyl alcohol and Mili-Q grade water for 5 min each. The substrate was then dried under nitrogen flow followed by ozone treatment for 15 min at 25 ^{0}C to remove organic impurities and to attain a hydrophilic surface. To develop a thin layer of Mn^{2+} doped ZnS Qdot, 10 mg of Qdots was dispersed in 1 mL methanol and it was sonicated for 45 min to obtain a homogeneous dispersion. The dispersion was then spin coated on Si/SiO_2 substrate at 1000 rpm for 40 s twice and heat treated at 120 ^{0}C for 15 min on a hot plate in ambient air condition. Finally, source and drain electrodes were deposited by thermally evaporating 99.99% pure aluminium through a shadow mask with a channel width of 3000 μm and channel length of 100 µm. Thermal evaporation was carried out at a deposition rate of 10-14 Å per second at 6 $\times 10^{-6}$ mbar chamber pressure. Finally, the Qdot-TFT was annealed at 120 °C in a hot plate for 30 min. In a similar fashion QDC-TFT was fabricated by spin coating well dispersed QDC (10 mg/mL) followed by thermal evaporation of electrodes. The thickness of the thin film was examined from FESEM images of cross-sectional view of the device.

2.3 Instruments Used

Optical Characterization: Jasco V-360 spectrophotometer was used to record the absorption spectra of Qdots and QDCs. For observing photoluminescence spectra, Horiba JOBIN YVON Fluorolog spectrofluorimeter was used.

Morphological Characterization: JEOL JEM-2100F transmission electron microscope (TEM), operating at maximum acceleration voltage 200 kV, was used to record the transmission electron microscopic images, high resolution transmission electron microscope (HRTEM) images and selected area electron diffraction (SAED) patterns of the samples. Phase identification of both Qdots and QDCs were obtained from X-ray diffraction measurements, which was carried out using Bruker D2 Advance X-ray diffractometer.

Thickness Measurements: JEOL JSM-7610F field emission scanning electron microscope (FESEM) system was used to capture the cross sectional view of transistors to obtain film thickness.

Electrical Characterization: All electrical measurements were performed in darkness at room temperature. The thin film transistor characterisations (transfer characteristics curves and output curves) were carried out in Keithley 4200A SCS parameter analyser.

2.4 Materials Characterization

The Mn^{2+} doped ZnS Qdots of average size 3.2±0.4 nm were synthesised following an earlier reported method,[32, 39] details of which are presented in the experimental section. The characteristics of the Qdots were established from transmission electron microscopy (TEM), powder X-ray diffraction (XRD) patterns, photoluminescence (PL) and UV-visible spectral analyses. The UV-vis spectrum of Qdots exhibited characteristic shoulder in 330 nm wavelength due to the excitonic absorption of the host ZnS (**Figure 2.1a**). Mn^{2+} doped ZnS Qdots, when irradiated with light of 330 nm wavelength, a sharp emission peak at 595 nm was observed owing to the transitions from $^4T_1$ excited state of Mn^{2+} ions to $^6A_1$ state and a comparatively weaker peak was observed at 440 nm due to host ZnS[32] (**Figure 2.1b**). These Qdots when allowed to react with 8-hydroxyquinoline 5-sulphonic acid (HQS), the ligand interacted with the surface cations of the Qdots to form bluish green emitting (λ_{em}=480 nm) zinc quinolate ($Zn(QS)_2$) complex on the surface. With increase in the concentration of HQS ligand gradual increase of emission peak at 480 nm and gradual quenching of 595 nm peak was observed (**Figure 2.1b**).

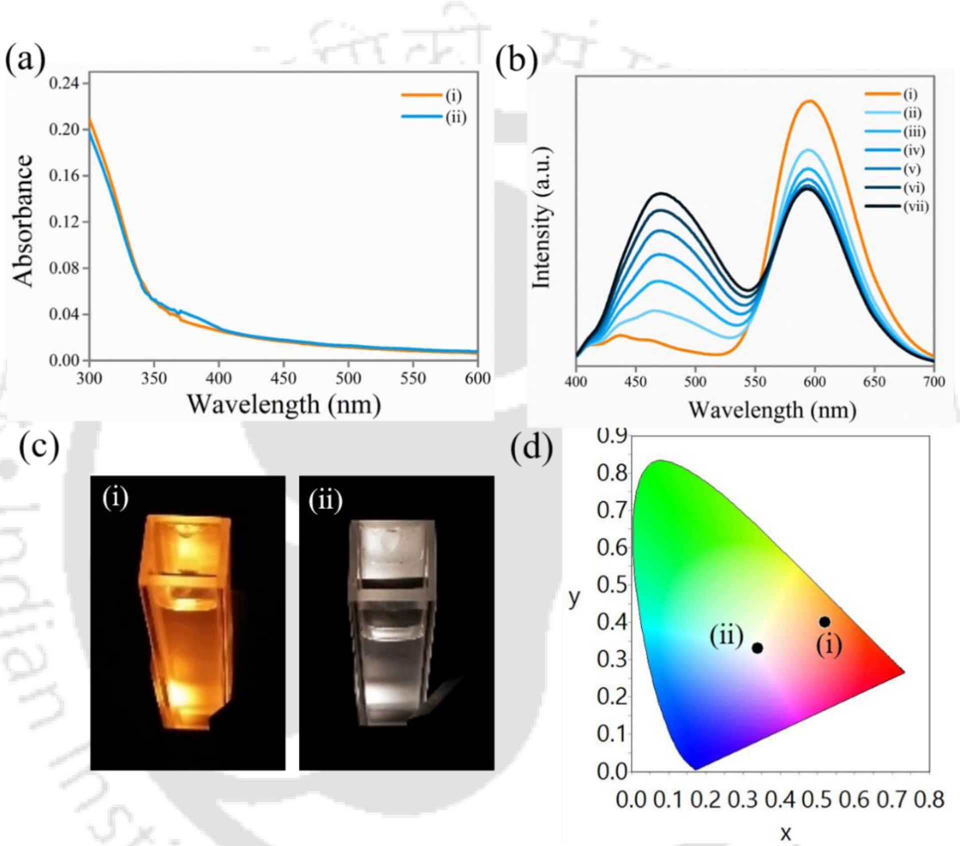

Figure 2.1. (a) UV-vis spectra of (i) Mn^{2+} doped ZnS Qdots and (ii) HQS added Mn^{2+} doped ZnS Qdot., (b) Emission spectra (λ_{ex}= 330nm) of (i) 00, (ii) 0.99 µM, (iii) 1.99 µM, (iv) 2.99 µM, (v) 3.98 µM, (vi) 4.97 µM, (vii) 5.96 µM, HQS added to Mn^{2+}doped ZnS Qdot, (c) digital photograph and (d) chromaticity color coordinates in CIE Diagram of (i) Mn^{2+} doped ZnS Qdots and (ii) HQS added Mn^{2+} doped ZnS Qdot.

The optimum amount of HQS ligand required for the formation of QDC was ascertained to be 5.96 µM in 3.0 mL of Qdot dispersion. The combined emission of the complex and the Qdot resulted in the appearance of white light emission when excited with UV light. This complex conjugated Qdot was termed as QDC. The digital photographs of Qdot and QDC are shown in **Figure 2.1c**. It is to be mentioned here that the optimum concentration of HQS ligand was chosen based on the white light parameters (CIE, CRI and CCT values) to achieve near to perfect white light emission from QDC. The WLE QDC exhibited the CIE coordinates, CRI and CCT values as (0.34, 0.33), 78 and 5220 K, respectively (**Figure 2.1d, Figure A2.1 and Table A1, Appendix A**), which signifies the bright cool white light emitting nature of the synthesized QDC. The PL emission spectrum of QDC demonstrated two emission bands centred at 480 nm and 595 nm at an excitation wavelength of 330 nm. The emission peak at 480 nm is attributed to the electronic transitions between the HOMO- LUMO levels of the $Zn(QS)_2$ complex formed on the surface of Mn^{2+} doped ZnS Qdots.

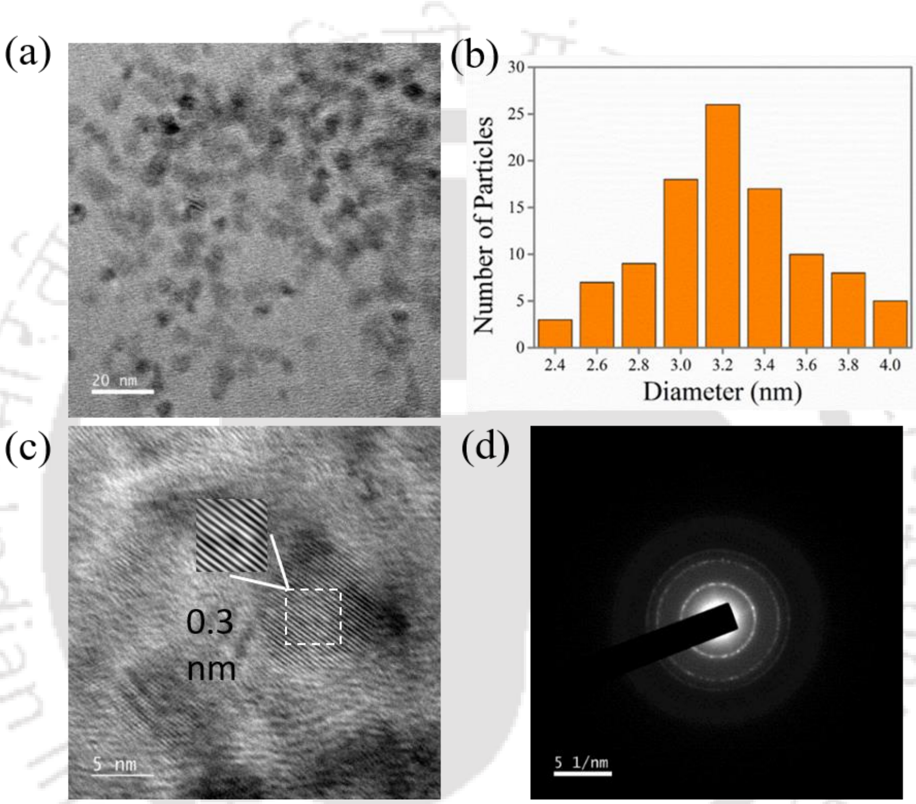

Figure 2.2. (a) TEM images (scale bar = 20 nm), (b) corresponding particle size distribution, (c) HRTEM image (scale bar = 5 nm) (inset: IFFT image of corresponding marked area) with lattice fringe spacing 0.3 nm and (d) SAED pattern of the as - synthesized Mn^{2+} doped ZnS Qdot.

In addition to the absorption band edge at 330 nm, appearance of an absorption peak at 365 nm confirmed the formation of $Zn(QS)_2$ complex on the surface Qdot (**Figure 2.1a**). Further, Qdot and QDC exhibited excitation peaks at 330 and 365 nm for their corresponding emission maxima at 595 nm and 480 nm respectively (**Figure A2.2, Appendix A**). This observation also supported the formation of $Zn(QS)_2$ complex on the surface of Qdot. The measurements of photoluminescence quantum yields (PLQY) was calculated using the equation represented in Eq A1 and it revealed that Qdot and QDC exhibited almost 1.2% PLQY (**Eq A2.1, Appendix A**). In addition, formation of Mn^{2+} doped ZnS Qdots having average particle size of 3.2 ± 0.4

nm could also be elucidated from the TEM analysis (**Figure 2.2a, b**). The high resolution transmission electron microscopy (HRTEM) analysis suggested the crystallinity of the Qdot core and 0.3 nm lattice fringe spacing of (111) crystal planes of cubic ZnS.[32] was confirmed from the selected area electron diffraction (SAED) patterns of Qdots (**Figure 2.2c, d**). Characteristic peaks at 2θ value of 28.30°, 47.40° and 56.40° due to (111), (220) and (311) lattice planes of cubic ZnS was observed in the powder XRD analysis (**Figure 2.3**).[32] No change in morphology or the crystallinity of the Qdots was observed after formation of surface complexes (**Figure 2.3, Figure A2.3. Appendix A**)

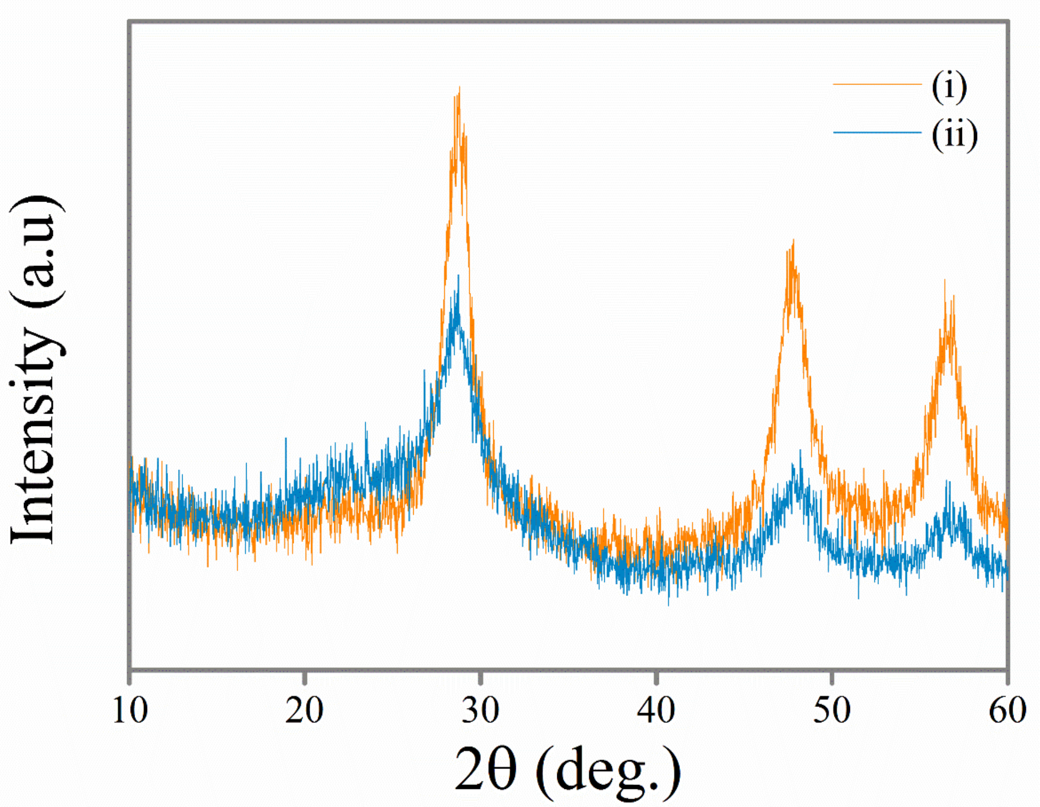

Figure 2.3. Powder X-ray diffraction patterns of (i) Mn^{2+} doped ZnS Qdot and (ii) HQS surface complexed Mn^{2+} doped ZnS Qdot (i.e., QDC). (characteristic peaks were observed at 2θ value 28.30º, 47.40º and 56.40º)

2.5 Thin Film Transistor Characteristics

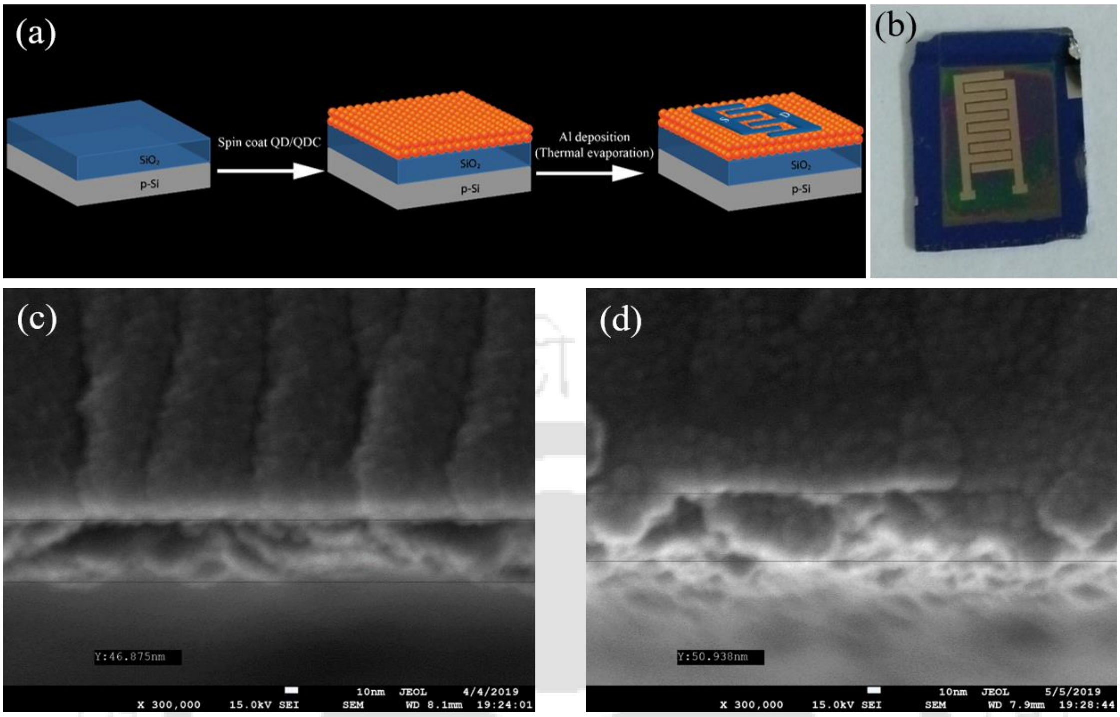

Figure 2.4. (a) Schematic representation of fabrication of thin film transistor. (b) Digital photograph of a thin film transistor. FESEM image of cross-sectional view of (c) QDC-TFT (thickness 46.9 nm) and (d) Qdot-TFT (thickness 50.9 nm).

To explore the charge transport characteristics of Mn^{2+} doped ZnS Qdots and WLE Mn^{2+} doped ZnS QDC, they were incorporated in a bottom gate/top contact thin film transistor (TFT) design as per the schematic shown in **Figure 2.4a, b,** details of which are presented in experimental section. Briefly, 10 mg/mL of colloidal dispersion of WLE QDC was spin coated onto Si/SiO_2 substrates at a speed of 1000 rpm for 40 s twice to obtain meaningful electrical output and the second round of deposition improved the quality of the output. A ~46 nm thick layer of QDC was deposited onto the substrates, which was confirmed from the field emission scanning electron microscope (FESEM) image of cross-sectional view of the device (**Figure 2.4c**). Interdigitated electrodes were deposited by thermal evaporation of aluminium through a shadow mask for source and drain contacts. To extract the transfer characteristic curves (drain current (I_d) vs gate voltage (V_g)) the device was biased in both p-FET and n-FET biasing conditions at drain voltage 5V and -5 V, respectively (**Figure 2.5a, b**). The "V" shaped nature in the linear region of the transfer characteristic curves illustrated ambipolar charge transport behaviour in QDC-TFT, which means both electrons and holes can contribute to the conduction based on the biasing conditions. The type of charge transport can be interpreted from the slope

$\partial I_d/\partial V_g$ of the linear region of the transfer characteristic curve. The transfer characteristic curves of QDC-TFT indicated a relatively symmetric ambipolar conduction with an I_{ON}/I_{OFF} ratio of ~10^4 and threshold voltage, $V_{th(n)}$ of 5.09 V and $V_{th(p)}$ of -3.6 V in n-FET and p-FET operations, respectively.

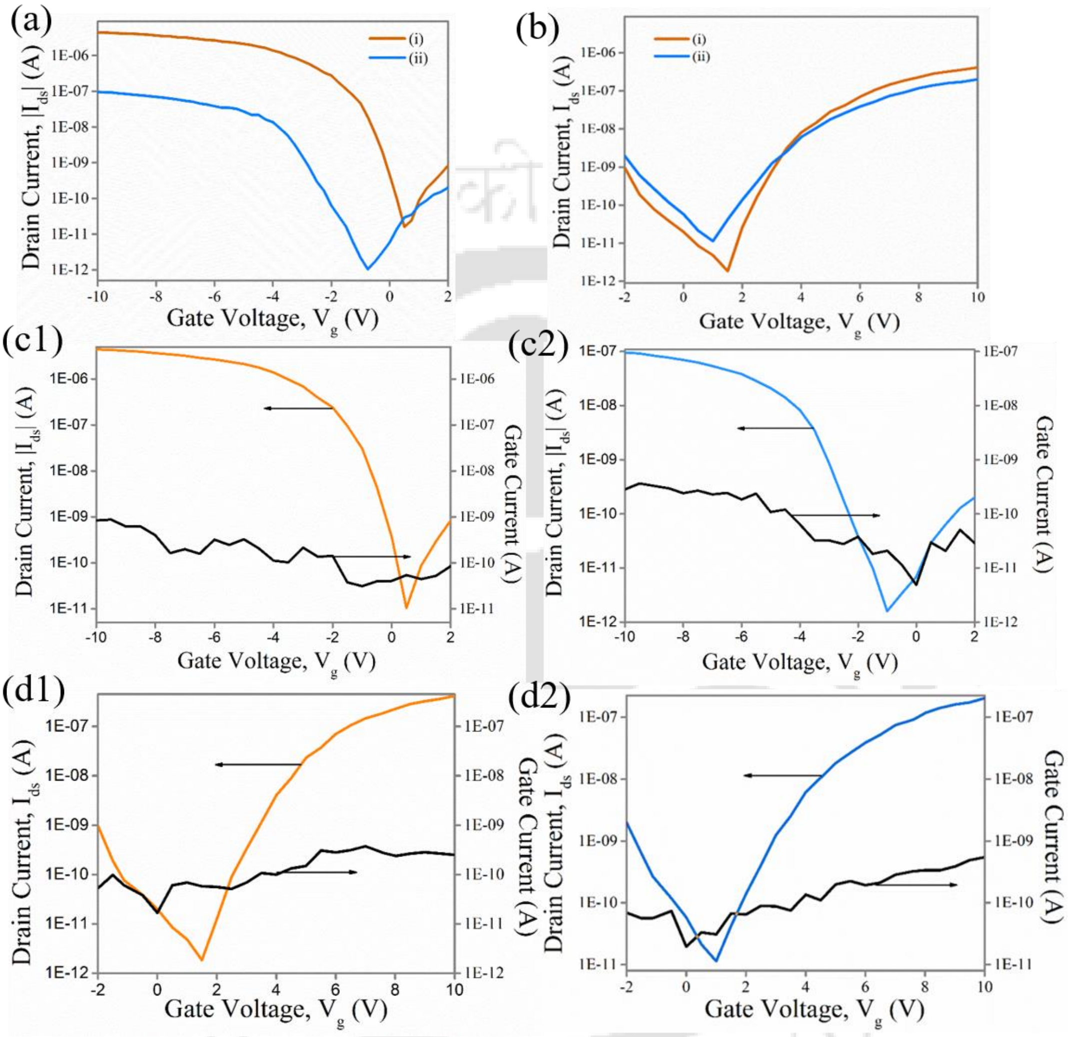

Figure 2.5. Transfer characteristics of (i) Mn^{2+} doped ZnS Qdots and (ii) HQS complexed Mn^{2+} doped ZnS Qdots when operated as (a) p-FET (Vd=-5V) and (b) n-FET (Vd=+5V). Comparison of leakage current to drain current (c1) Qdot-TFT (p-FET) and (c2) QDC-TFT (p-FET), (d1) Qdot-TFT (n-FET) and (d2) QDC-TFT (n-FET).

I_{ON}/I_{OFF} ratios of these devices are significant enough for constructing high performance ambipolar transistors. The n-FET, p-FET or ambipolar transport in Qdot thin films is considerably dependent on stoichiometry of Qdot, synthesis conditions and nature of capping ligands.[28, 40] Further, systematic investigation on the transport properties of Mn^{2+} doped ZnS Qdots without surface complexation was also carried out to compare with that of surface complexed Qdots. Approximately, 50 nm thick layer (obtained from the FESEM image of the cross- sectional view of the device, **Figure 2.4d**) of orange light emitting Qdots was used as the active material for fabricating Qdot thin film transistor (Qdot-TFT) device. Qdot-TFT exhibited ambipolar carrier transport characteristics (**Figure 2.5a, b**) with an I_{ON}/I_{OFF} ratio of 10^5 in both n-channel and p-channel operations at drain voltage +5V and -5V, respectively. Linear gate voltage (V_g) vs logarithmic and square root of drain current (I_d) of Qdot –TFT and QDC-TFT are shown in **Figure A2.4, Appendix A**. An asymmetric "V" shape in the linear region of the transfer characteristic curve was observed, which may be attributed to unequal electron and hole transport in Qdot thin films.

Structural parameters such as contact area and gate dielectric layer on the gate leakage current are key determinants in the performance of TFTs. Unidirectional gate current outflows from gate terminal to source/drain terminal because of the tunnelling of charge carriers at higher gate voltages, as it induces strong vertical electric field across the thin dielectric layer.[41] The interference of this current at drain terminal deteriorate the device performance. A comparison of leakage current to drain current for both Qdot-TFT and QDC-TFT were established (**Figure 2.5c1-d2**) to ensure that the SiO_2 gate dielectric blocks the tunnelling of electrical charge carriers between gate electrode and the top contacts. Gate leakage current in the range of 1nA was observed and the same is anticipated to arise because of larger source drain electrode pads of the thin film transistors. On the other hand, the measured drain currents were high enough in comparison to gate leakage currents to investigate the device performances.

The output characteristic curves of Qdot-TFT with $V_{th(p)}$ -2.15 V and $V_{th(n)}$ 5.12 V show p-channel characteristics superior (higher drain current, I_d) to that of n-channel characteristics (**Figure 2.6 a1, b1**). Zinc sulphide, being a II-VI compound semiconductor and having direct and wide band gap of 3.6 eV, facilitates both n-type and p-type doping. The type of doping is described to arise either due to donation of free electrons to host system or due to substitutional doping at Zn^{2+} defect sites. In p-doped ZnS, the dopant atoms occupy the Zn^{2+} substitutional sites that are proposed to promote hole transport.[42] Such kinds of p-type conductivity are also known to occur in Mn^{2+} doped ZnO, As and Sb doped ZnS and ZnSe.[43-45] In Mn^{2+} doped ZnS Qdots, Mn^{2+} ions occupy the Zn^{2+} lattice cites and S^{2-} ions tetrahedrally coordinate the Mn^{2+} ion. Therefore, a p-type doping can be anticipated in Mn^{2+} doped ZnS, which – in the current case – would result in a superior p-channel device than n-channel device.

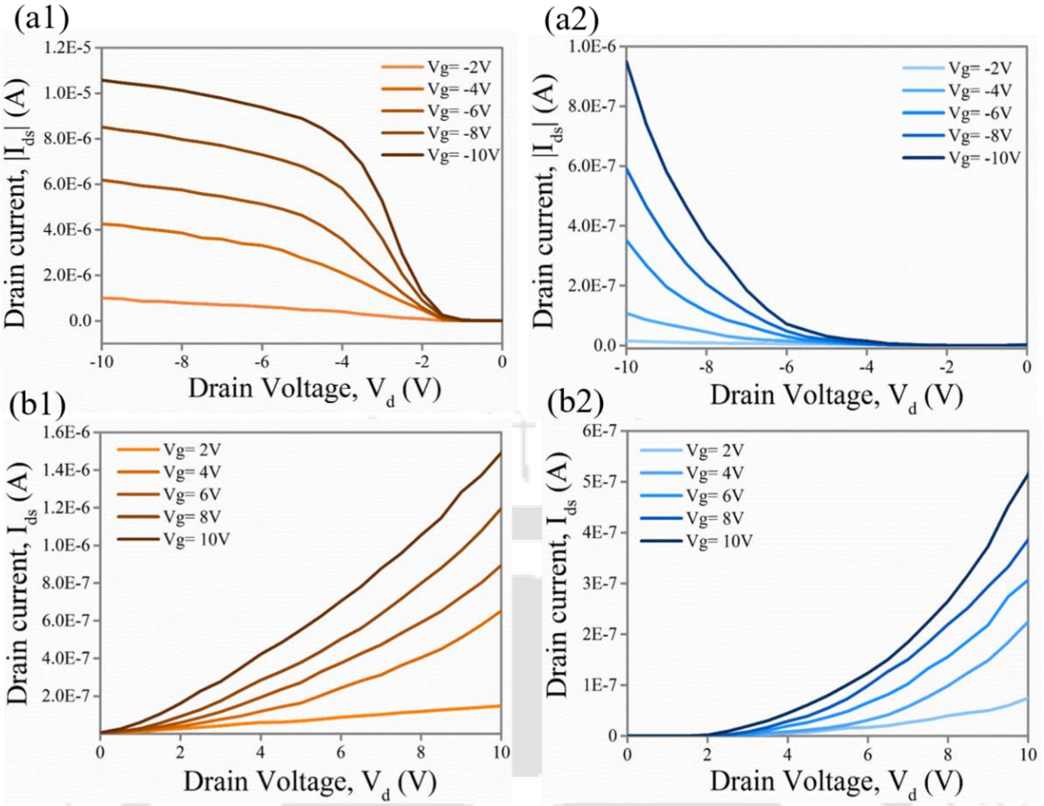

Figure 2.6. Output characteristic curve in (a1) p-channel Qdot-TFT, (a2) p-channel QDC-TFT, (b1) n-channel Qdot-TFT and (b2) n-channel QDC-TFT.

However, a reduction in the drain current was observed in p-channel QDC-TFT, which may be attributed to the complexation of HQS ligands on the surface of Qdots. However, the drain current in n-channel transport of QDC-TFT did not change significantly (**Figure A2.6 a2, b2**). It has already been established that polyquinolines and polyquinoline copolymers, metal chilates containing quinolone moiety such as AlQ_3, InQ_3 and ZnQ_2 (which are used in a plethora of OLED applications) act as superior electron injection and transport materials.[46-48] ZnQ_2 is better known for its electron injection and electron transport because of stronger π-π overlap between the ligands and the extended electronic states in its tetrameric form.[46-48] So similar transport characteristics can be expected when HQS is allowed to react with the surface cation of Qdot, to form $Zn(QS)_2$ complex on the surface of Qdot, It has been already reported that, interligand distance of 3.37 Å among 8-hydroxyquinoline (HQ) ligands in ZnQ_2 give rise to a strong pi-pi interaction, making them notable candidates for electron transport material with efficient electron mobilities.[46-48] On the other hand, the inter QDC spacing would depend on the geometry of the complex on the surface. Our earlier observations indicated the formation of an octahedral complex,[31-33, 47] which would make the inter particle separation shorter in comparison to other arrangements of ligand attachment on the surface. Hence, we anticipate that the reduction in hole mobility and relatively better electron transport in QDC-TFT is because of attachment of HQS ligand to the surface of Qdot in a geometry similar to 8-hydroxyquinoline (HQ) i.e., octahedral.[49-51] The ambipolar nature in the output curves of both the devices can be observed clearly in **Figure A2.5, Appendix A**.

To get a better insight into the charge transports in Qdots and QDCs in solid state, field effect carrier mobilities in linear region were calculated from the transfer characteristic curves of the operating TFT, using gradual channel approximations. The following equation was used to calculate the linear electron mobility and linear hole mobility.

$$\mu_{linear} = \left(\frac{\partial I_d}{\partial V_g}\right) . {}^{L}/_{W C_i V_d} \qquad \textbf{2.1}$$

Where μ_{linear} is the linear mobility of charge carrier, L is the channel length, W is the channel width, C_i is the parallel plate dielectric capacitance of SiO_2 layer per unit area (10 $nF.cm^{-2}$ for 300 nm SiO_2), V_d is the applied drain voltage, I_d is the linear drain current and V_g is the applied gate voltage. Using these values, the Qdot-TFT was characterised with hole mobility (μ_p) of 4.89×10^{-01} $cm^2V^{-1}s^{-1}$ and electron mobility (μ_n) of 5.20×10^{-02} $cm^2V^{-1}s^{-1}$. A higher mobility of holes in Qdot-TFT supported the observed larger drain current in p-FET operational mode of the same device. The μ_n and μ_p of QDC-TFT were found to be 2.95×10^{-02} $cm^2V^{-1}s^{-1}$ and 1.06×10^{-02} $cm^2V^{-1}s^{-1}$ respectively (**Figure A2.6, Appendix A**). These values of mobilities are comparable with previously reported Qdot based devices. A comparative review study on different Qdot based thin film transistors are tabulated in **Table A2** (**Appendix A**). Reduced carrier mobilities in QDC-TFT may be attributed to the surface disorders and increased carrier trap states in QDC thin films.

Ligand exchange prototypes to improve inter dot packing and mobility in Qdot thin films do not always ensure high mobility. On the other hand, they may introduce carrier trap states in nanocrystal thin films. Strategies to map trap state densities in thin films are highly desired in order to improve optoelectronic device performances. The subthreshold slope of transfer characteristic curve, demarcated by V_{th} of the device, provide crucial information about shallow trap states within the band gap of Qdot. In the subthreshold regime (pre-conductive regime), $\log(I_d)$ increases sharply with linear increase in V_g. Subthreshold slope of a thin film transistor indicates how much the gate voltage has to be increased to obtain a 10-fold increase in the drain current. For mapping of electronic trap states, both Qdot and QDC devices were analysed in the subthreshold region. In case of Qdot-TFT, the subthreshold swing was found to be 0.35 $V.dec^{-1}$ in p-channel operation and 0.59 $V.dec^{-1}$ in n-channel operation. Additionally, the subthreshold slopes of QDC-TFT were found to be 0.79 $V.dec^{-1}$ and 0.97$V.dec^{-1}$ in p-FET and n-FET operations, respectively (**Figure A2.7, Appendix A**). This broadening of subthreshold regime indicates introduction of additional carrier traps at the band edges of surface complexed Qdots. Trap states in colloidal Qdots triggers non-radiative recombination and may affect the carrier mobility when in-gap trap states are filled by charge carriers. Furthermore, to get a better idea of the thin film device performance, we have estimated trap state density (D_{it}) in the device using subthreshold slope formula (**Eq A2.2, Appendix A**). The trap state densities of Qdot-TFT and QDC-TFT are tabulated in **Table A3 (Appendix A).** The carrier trap state density in Qdot-TFT was 2.97×10^{11} $cm^{-2}.eV^{-1}$ and 5.59×10^{11} $cm^{-2}.eV^{-1}$ when operated in p-FET and n-FET configuration respectively. Increased D_{it} values of 9.24×10^{11} $cm^{-2}.eV^{-1}$ in p-FET and 9.40×10^{11} $cm^{-2}.eV^{-1}$ n-FET operations of QDC-TFT imply that the complexation of Mn^{2+} doped ZnS Qdot surfaces by HQS ligands might have introduced additional carrier trap states, which resulted in a broader subthreshold slop and reduced carrier mobility. As mentioned before, the HQS formed an inorganic complex on the surface of the Qdot with plausible octahedral geometry. This may provide a new species to the QDC where the complex acted as a trap state independent of the trap states of the Qdot.

2.6 Time-Resolved Photoluminescence Spectral Analysis

To study the excited state lifetimes of the samples, time-resolved photoluminescence spectral analyses were carried out. The QDC exhibited average emission life times of 14.73 ns and 8.76 ns at λ_{em}= 480 nm and λ_{ex}=336 nm (diode source) excitations, in colloidal phase and thin film, respectively. The same samples exhibited average lifetimes of 15.02 ns and 8.46 ns in colloidal phase and thin film, respectively at λ_{em}= 480 nm and λ_{ex}=375 nm (laser source) excitations. On the other hand, at λ_{em}= 595 nm and λ_{ex}=330 nm (pulsed xenon lamp source) excitations, the same QDC showed the average emission lifetimes of 1.50 ms in colloidal phase and 1.17 ms in thin film, whereas the as synthesized Mn^{2+} doped ZnS Qdot exhibited average emission lifetimes of 1.47 ms (colloidal) and 1.24 ms (thin film) under same experimental conditions (λ_{em}= 595 nm and λ_{ex}=330 nm (pulsed xenon lamp source) (**Figure 2.7**, **Table A4**, **Appendix A**). The longer emission life time of Mn^{2+} doped ZnS Qdot arises because of the spin forbidden transition between $^4T_1$-$^6A_1$ state in the 3d subshell of Mn^{2+} dopant.[52-54]

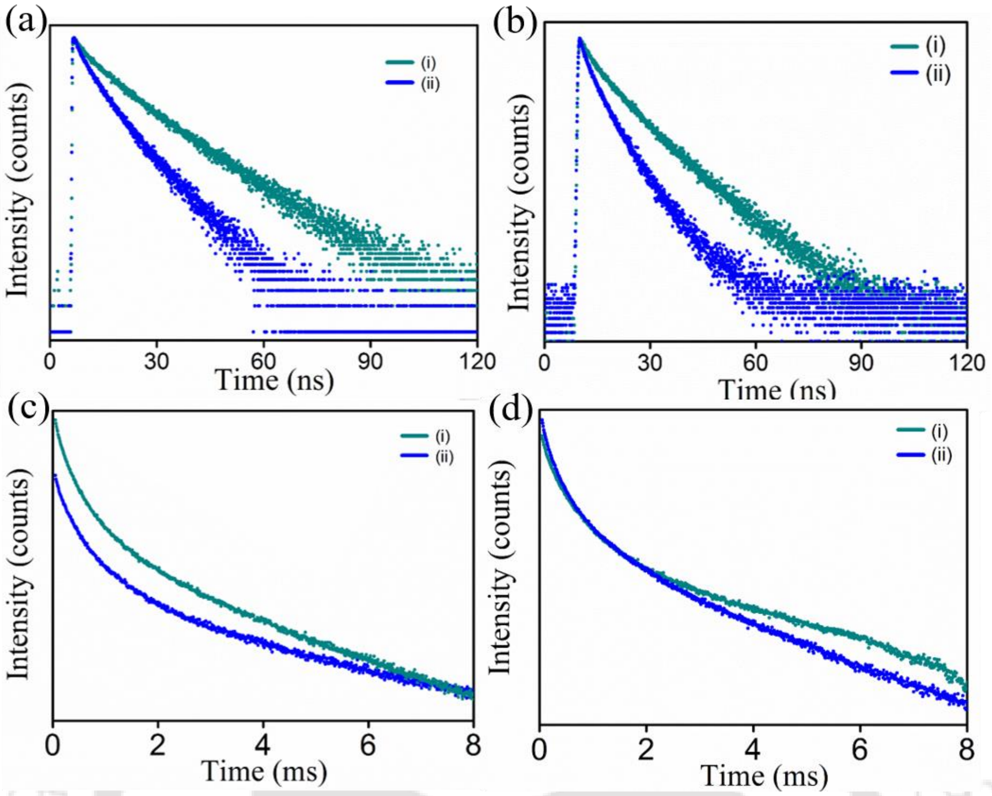

Figure 2.7. Time-resolved photoluminescence spectra of (a) QDC at λ_{ex} of 375 nm (laser source) and λ_{em} of 480 nm, (b) QDC at λ_{ex} of 336 nm (diode source) and λ_{em} of 480 nm, (c) Mn^{2+} doped ZnS Qdot, at λ_{ex} of 330 nm (pulsed xenon lamp) and λ_{em} of 595 nm, (d) QDC, at λ_{ex} of 330 nm (pulsed xenon lamp) and λ_{em} of 595 nm in (i) colloidal dispersion and (ii) thin film.

This longer emission lifetime (λ_{em} = 595 nm) remains nearly unaffected after attachment of HQS ligand to the surface of Qdot. This observation is also supported from the previously reported results that the emission lifetime of Mn dopant remains the same following attachment of thiol ligand to the surface of Mn doped CdS/ZnS nanocrystal.[54] On the other hand, the shorter emission lifetime (λ_{em} = 480 nm) of $Zn(QS)_2$ surface complex matches with our earlier reported value, which clearly indicated the formation of complex on the surface of Qdots.[31, 33, 49] However, the emission of Qdot at 595 nm was quenched significantly after formation of $Zn(QS)_2$ complex with no considerable changes in the emission lifetime of Qdot at λ_{em} = 595 nm. This may be due to the static quenching process occurring between the Qdot and surface complex, where $Zn(QS)_2$ complex acts as a quencher to the dopant emission of Qdot.[32, 49] It is to be mentioned here that, there is an overlapping region between the emission spectrum of surface $Zn(QS)_2$ and absorption spectrum of Qdot, which may create the possibility of energy transfer between the two species.[33, 49]

2.7 Carrier Hopping Characteristics

Transport mechanism in Qdots is rather complex and can be explored by their temperature dependent transport studies. Carrier Transport in weakly coupled Qdots is established to occur through hopping of charge carriers from one site to another (Qdot to Qdot) whereas strongly coupled nanocrystal solids exhibit band like transport pattern. To study the transport mechanisms in Mn^{2+} doped Qdot and QDC (Mn^{2+} doped Qdot, surface complexed with HQS), we have extracted the transfer characteristic curves of both the device over the temperature range of 77K-357K (**Figure 2.8 a, b**). The transfer curves of ambipolar nature were obtained at a drain bias voltage V_d of 10V. It is observed that, in case of QD-TFT the hole current increased with increasing temperature over the entire temperature range. However, no significant change in the electron current was observed in the same device. Interestingly, regular increase in the electron as well as hole current was observed in case of QDC-TFT. Conductance in semiconductor nanocrystals are described by the equation $G=G_0\exp(-T_0/T)^p$, where p is dependent on the type of hopping and T_0 is dependent on material properties. The above equation can be rewritten as $\mu=\mu_0\exp(-T_0/T)^p$, where μ is the mobility. In hopping transport in semiconductor nanocrystals, a single hoping event can be described by the probability function $P \sim \exp\left(-\frac{2R}{a} - \frac{\varepsilon}{kT}\right)$, where r is the distance between two hopping states, a is the electron or hole localization length, ε is the energy difference associated with the hopping sites and k is the Boltzman constant. From this it can be interpreted that, at higher temperature i.e., when $2R/a >> \varepsilon/kT$, the hoping mechanism is independent of the energy difference between the hoping sites and thus carrier hopping occurs between nearest neighbors known as nearest-neighbor hopping (NNH). This type of hopping exhibits Arrhenius like characteristics (p=1). However, at lower temperature the conductance deviates from Arrhenius behavior and hoping between sites with equivalent energy is prevalent. Thus hopping distance varies at low temperature regime and such conduction is termed as variable range hopping (VRH).[13, 55, 56] To analyze these transport characteristics, in our device mobility vs temperature plot was analyzed. In case of Qdot device, the hole mobility decreased with decreasing temperature. The mobility versus temperature curve in this can be fitted to nearest neighbor hopping model from 257 K to 357 K and from temperature 77 K to 217 K the graph can be fitted to VRH model. Likewise, in QDC-TFT both electron and hole mobilities can be fitted to VRH model between 77 K to 217 K and to NNR model between 257 K to 357 K. The temperature dependent carrier mobilities are plotted in **Figure 2.8 c, d**. It was also observed that the QDC incorporated device exhibited larger hysteresis than that of Qdot incorporated device.

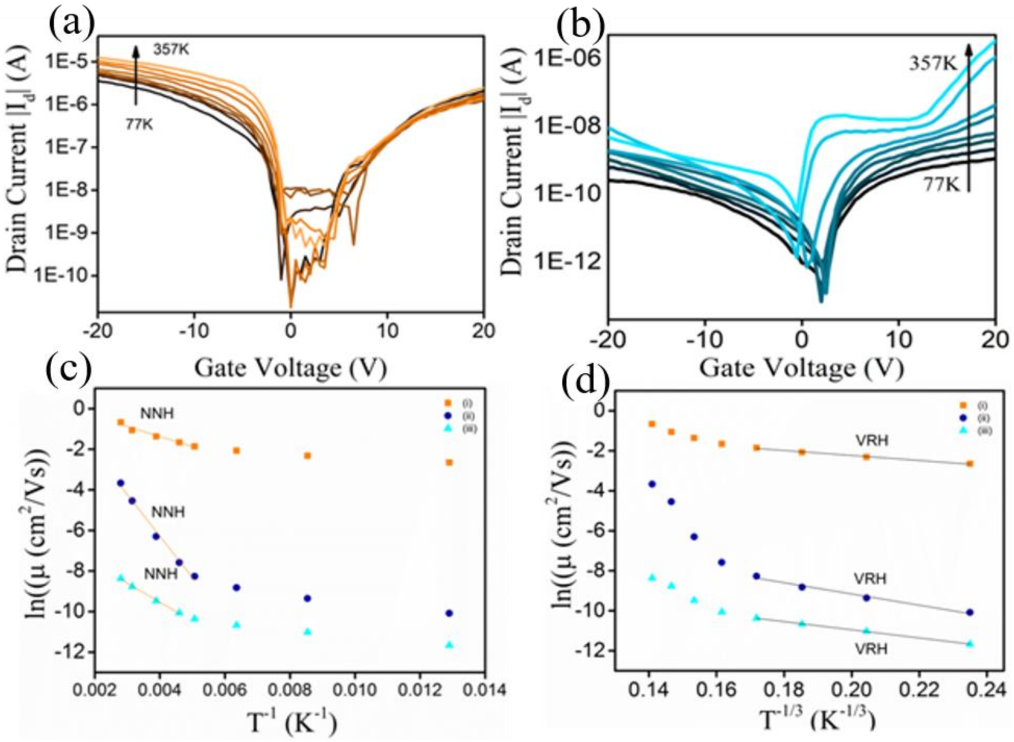

Figure 2.8. Transfer curves taken over temperature range of 77 K to 357 K at drain bias voltage of 10 V of (a) Qdot-TFT and (b) QDC-TFT. Carrier Mobilities over the entire temperature range are fitted to (c) nearest neighbor hopping model and (d) variable range hopping model for (i) hole carrier mobility of Qdot, (ii) electron carrier mobility of QDC and (iii) hole carrier mobility of QDC.

Interestingly, at an elevated temperature (375 K) both the devices exhibited higher hysteresis than at a low temperature (77 K) (**Figure A2.8, Appendix A**). Higher rate of hopping at elevated temperature may have led to trapping of carriers into deeper trap states within the band gap of the system. At low temperature these trap states however are likely filled by charge carriers and hence lesser hysteresis was observed. These results support the higher subthreshold slope observed in QDC-TFT devices.

2.8 Conclusions

In a nutshell, we have studied the charge transport characteristics of environmentally benign white light emitting surface complexed Mn^{2+} doped ZnS Qdots (QDC) implemented in a TFT design. The device exhibited excellent ambipolar transport characteristics with high I_{ON}/I_{OFF} ratio of 10^4 and a fairly high electron mobility of 2.95×10^{-02} $cm^2V^{-1}s^{-1}$ and hole mobility of 1.06×10^{-02} $cm^2V^{-1}s^{-1}$. To understand the charge transport mechanisms in the surface complexed Qdot, a comparison was drawn between performances of Qdot-TFT and QDC-TFT. The higher value of subthreshold slope in QDC-TFT (0.79 V.dec^{-1} and 0.97 V.dec^{-1} in p-FET and n-FET operations, respectively) than Qdot-TFT indicated that additional carrier trap states were created in QDC-TFT, which may be attributed to the formation of Zn(QS)$_2$ complex on the Qdot surface. Electron mobility in Qdot system can be fitted to NNH model at elevated temperature and VRH model at low temperature. However, both hole mobility and electron mobility in QDC system can be fitted to NNH model between 257 K to 357 K and to VRH model between 77 K to 217 K. The white light emitting feature and its excellent ambipolar carrier transport characteristics with fairly high carrier mobilities make it a suitable emitter and transport material for white light emitting diodes and transistors and thus would provide a new entrant in advanced optoelectronics.

2.9 References

1. He, P. H.; Jiang, C. B.; Lan, L. F.; Sun, S.; Li, Y. Z.; Gao, P. X.; Zhang, P.; Dai, X. Q.; Wang, J.; Peng, J. B.; Cao, Y. High-Performance, Solution-Processed Quantum Dot Light-Emitting Field-Effect Transistors with a Scandium-Incorporated Indium Oxide Semiconductor. *Acs Nano.* **2018**, 12, 4624-4629.

2. Liu, X.; Kuang, W. J.; Ni, H. B.; Tao, Z.; Chang, J. H.; Liu, Q. Q.; Ge, J. X.; Li, C.; Dai, Q. High Efficiency Light-Emitting Transistor with Vertical Metal-Oxide Heterostructure. *Small.* **2018**, 14.

3. Maddalena, F.; Chin, X. Y.; Cortecchia, D.; Bruno, A.; Soci, C. Brightness Enhancement in Pulsed-Operated Perovskite Light-Emitting Transistors. *Acs Applied Materials & Interfaces.* **2018**, 10, 37316-37325.

4. Natali, M.; Quiroga, S. D.; Passoni, L.; Criante, L.; Benvenuti, E.; Bolognini, G.; Favaretto, L.; Melucci, M.; Muccini, M.; Scotognella, F.; Di Fonzo, F.; Toffanin, S. Simultaneous Tenfold Brightness Enhancement and Emitted-Light Spectral Tunability in Transparent Ambipolar Organic Light-Emitting Transistor by Integration of High-k Photonic Crystal. *Advanced Functional Materials.* **2017**, 27.

5. Dinelli, F.; Capelli, R.; Loi, M. A.; Murgia, M.; Muccini, M.; Facchetti, A.; Marks, T. J. High-mobility ambipolar transport in organic light-emitting transistors. *Advanced Materials.* **2006**, 18, 1416-+.

6. Capelli, R.; Toffanin, S.; Generali, G.; Usta, H.; Facchetti, A.; Muccini, M. Organic light-emitting transistors with an efficiency that outperforms the equivalent light-emitting diodes. *Nature Materials.* **2010**, 9, 496-503.

7. McCarthy, M. A.; Liu, B.; Donoghue, E. P.; Kravchenko, I.; Kim, D. Y.; So, F.; Rinzler, A. G. Low-Voltage, Low-Power, Organic Light-Emitting Transistors for Active Matrix Displays. *Science.* **2011**, 332, 570-573.

8. Bisri, S. Z.; Sawabe, K.; Imakawa, M.; Maruyama, K.; Yamao, T.; Hotta, S.; Iwasa, Y.; Takenobu, T. Organic Single-Crystal Light-Emitting Transistor Coupling with Optical Feedback Resonators. *Scientific Reports.* **2012**, 2.

9. Schornbaum, J.; Zakharko, Y.; Held, M.; Thiemann, S.; Gannott, F.; Zaumseil, J. Light-Emitting Quantum Dot Transistors: Emission at High Charge Carrier Densities. *Nano Letters.* **2015**, 15, 1822-1828.

10. Liu, C. F.; Liu, X.; Lai, W. Y.; Huang, W. Organic Light-Emitting Field-Effect Transistors: Device Geometries and Fabrication Techniques. *Advanced Materials.* **2018**, 30.

11. Liu, J.; Zhang, H. T.; Dong, H. L.; Meng, L. Q.; Jiang, L. F.; Jiang, L.; Wang, Y.; Yu, J. S.; Sun, Y. M.; Hu, W. P.; Heeger, A. J. High mobility emissive organic semiconductor. *Nature Communications.* **2015**, 6.

12. Litvin, A. P.; Martynenko, I. V.; Purcell-Milton, F.; Baranov, A. V.; Fedorov, A. V.; Gun'ko, Y. K. Colloidal quantum dots for optoelectronics. *Journal of Materials Chemistry A.* **2017**, 5, 13252-13275.

13. Shulga, A. G.; Kahmann, S.; Dirin, D. N.; Graf, A.; Zaumseil, J.; Kovalenko, M. V.; Loi, M. A. Electroluminescence Generation in PbS Quantum Dot Light-Emitting Field-Effect Transistors with Solid-State Gating. *Acs Nano.* **2018**, 12, 12805-12813.

14. Jung, S. M.; Kang, H. L.; Won, J. K.; Kim, J.; Hwang, C.; Ahn, K.; Chung, I.; Ju, B. K.; Kim, M. G.; Park, S. K. High-Performance Quantum Dot Thin-Film Transistors with Environmentally Benign Surface Functionalization and Robust Defect Passivation. *Acs Applied Materials & Interfaces.* **2018**, 10, 3739-3749.

15. Nugraha, M. I.; Hausermann, R.; Bisri, S. Z.; Matsui, H.; Sytnyk, M.; Heiss, W.; Takeya, J.; Loi, M. A. High Mobility and Low Density of Trap States in Dual-Solid-Gated PbS Nanocrystal Field-Effect Transistors. *Advanced Materials.* **2015**, 27, 2107-2112.

16. Liu, Y.; Tolentino, J.; Gibbs, M.; Ihly, R.; Perkins, C. L.; Liu, Y.; Crawford, N.; Hemminger, J. C.; Law, M. PbSe Quantum Dot Field-Effect Transistors with Air-Stable Electron Mobilities above 7 cm(2) V-1 s(-1). *Nano Letters.* **2013**, 13, 1578-1587.

17. Balazs, D. M.; Rizkia, N.; Fang, H. H.; Dirin, D. N.; Momand, J.; Kooi, B. J.; Kovalenko, M. V.; Loi, M. A. Colloidal Quantum Dot Inks for Single-Step-Fabricated Field-Effect Transistors: The Importance of Postdeposition Ligand Removal. *Acs Applied Materials & Interfaces.* **2018**, 10, 5626-5632.

18. Koh, W. K.; Saudari, S. R.; Fafarman, A. T.; Kagan, C. R.; Murray, C. B. Thiocyanate-Capped PbS Nanocubes: Ambipolar Transport Enables Quantum Dot Based Circuits on a Flexible Substrate. *Nano Letters.* **2011**, 11, 4764-4767.

19. Zhang, H.; Hu, N.; Zeng, Z. P.; Lin, Q. L.; Zhang, F. J.; Tang, A. W.; Jia, Y.; Li, L. S.; Shen, H. B.; Teng, F.; Du, Z. L. High-Efficiency Green InP Quantum Dot-Based Electroluminescent Device Comprising Thick-Shell Quantum Dots. *Advanced Optical Materials.* **2019**, 7.

20. Ayoubi, M.; Naserzadeh, P.; Hashemi, M. T.; Rostami, M. R.; Tamjid, E.; Tavakoli, M. M.; Simchi, A. Biochemical mechanisms of dose-dependent cytotoxicity and ROS-mediated apoptosis induced by lead sulfide/graphene oxide quantum dots for potential bioimaging applications. *Scientific Reports.* **2017**, 7.

21. Liu, Y.; Gibbs, M.; Puthussery, J.; Gaik, S.; Ihly, R.; Hillhouse, H. W.; Law, M. Dependence of Carrier Mobility on Nanocrystal Size and Ligand Length in PbSe Nanocrystal Solids. *Nano Letters.* **2010**, 10, 1960-1969.

22. Gu, M. F.; Wang, Y. J.; Yang, F.; Lu, K. Y.; Xue, Y.; Wu, T.; Fang, H. H.; Zhou, S. J.; Zhang, Y. N.; Ling, X. F.; Xu, Y. L.; Li, F. C.; Yuan, J. Y.; Loi, M. A.; Liu, Z. K.; Ma, W. L. Stable PbS quantum dot ink for efficient solar cells by solution-phase ligand engineering. *Journal of Materials Chemistry A.* **2019**, 7, 15951-15959.

23. Nugraha, M. I.; Kumagai, S.; Watanabe, S.; Sytnyk, M.; Heiss, W.; Loi, M. A.; Takeya, J. Enabling Ambipolar to Heavy n-Type Transport in PbS Quantum Dot Solids through Doping with Organic Molecules. *Acs Applied Materials & Interfaces.* **2017**, 9, 18039-18045.

24. Fafarman, A. T.; Koh, W. K.; Diroll, B. T.; Kim, D. K.; Ko, D. K.; Oh, S. J.; Ye, X. C.; Doan-Nguyen, V.; Crump, M. R.; Reifsnyder, D. C.; Murray, C. B.; Kagan, C. R. Thiocyanate-Capped Nanocrystal Colloids: Vibrational Reporter of Surface Chemistry and Solution-Based Route to Enhanced Coupling in Nanocrystal Solids. *Journal of the American Chemical Society.* **2011**, 133, 15753-15761.

25. Jo, C. H.; Kim, J. H.; Kim, J.; Kim, J.; Oh, M. S.; Kang, M. S.; Kim, M. G.; Kim, Y. H.; Ju, B. K.; Park, S. K. Low-temperature annealed PbS quantum dot films for scalable and flexible ambipolar thin-film-transistors and circuits. *Journal of Materials Chemistry C.* **2014**, 2, 10305-10311.

26. Liu, W. Y.; Lee, J. S.; Talapin, D. V. III-V Nanocrystals Capped with Molecular Metal Chalcogenide Ligands: High Electron Mobility and Ambipolar Photoresponse. *Journal of the American Chemical Society.* **2013**, 135, 1349-1357.

27. Huang, J.; Liu, W. Y.; Dolzhnikov, D. S.; Protesescu, L.; Kovalenko, M. V.; Koo, B.; Chattopadhyay, S.; Shenchenko, E. V.; Talapin, D. V. Surface Functionalization of Semiconductor and Oxide Nanocrystals with Small Inorganic Oxoanions (PO43-, MoO42-) and Polyoxometalate Ligands. *Acs Nano.* **2014**, 8, 9388-9402.

28. Oh, S. J.; Berry, N. E.; Choi, J. H.; Gaulding, E. A.; Lin, H. F.; Paik, T.; Diroll, B. T.; Muramoto, S.; Murray, C. B.; Kagan, C. R. Designing High-Performance PbS and PbSe Nanocrystal Electronic Devices through Stepwise, Post-Synthesis, Colloidal Atomic Layer Deposition. *Nano Letters.* **2014**, 14, 1559-1566.

29. Kahmann, S.; Sytnyk, M.; Schrenker, N.; Matt, G. J.; Spiecker, E.; Heiss, W.; Brabec, C. J.; Loi, M. A. Revealing Trap States in Lead Sulphide Colloidal Quantum Dots by Photoinduced Absorption Spectroscopy. *Advanced Electronic Materials.* **2018**, 4.

30. Stadler, P.; Sutherland, B. R.; Ren, Y.; Ning, Z. J.; Simchi, A.; Thon, S. M.; Hoogland, S.; Sargent, E. H. Joint Mapping of Mobility and Trap Density in Colloidal Quantum Dot Solids. *Acs Nano.* **2013**, 7, 5757-5762.

31. Bhandari, S.; Roy, S.; Pramanik, S.; Chattopadhyay, A. Surface Complexation Reaction for Phase Transfer of Hydrophobic Quantum Dot from Nonpolar to Polar Medium. *Langmuir.* **2014**, 30, 10760-10765.

32. Pramanik, S.; Roy, S.; Mondal, A.; Bhandari, S. A two- target responsive reversible ratiometric pH nanoprobe: a white light emitting quantum dot complex. *Chemical Communications.* **2019**, 55, 4331-4334.

33. Bhandari, S.; Khandelia, R.; Pan, U. N.; Chattopadhyay, A. Surface Complexation-Based Biocompatible Magnetofluorescent Nanoprobe for Targeted Cellular Imaging. *Acs Applied Materials & Interfaces.* **2015**, 7, 17552-17557.

34. Roushan, M.; Zhang, X.; Li, J. Solution-Processable White-Light-Emitting Hybrid Semiconductor Bulk Materials with High Photoluminescence Quantum Efficiency. *Angewandte Chemie-International Edition.* **2012**, 51, 436-439.

35. Wu, P.; Miao, L. N.; Wang, H. F.; Shao, X. G.; Yan, X. P. A Multidimensional Sensing Device for the Discrimination of Proteins Based on Manganese-Doped ZnS Quantum Dots. *Angewandte Chemie-International Edition.* **2011**, 50, 8118-8121.

36. Zhou, W. B.; Baneyx, F. Aqueous, Protein-Driven Synthesis of Transition Metal-Doped ZnS Immuno-Quantum Dots. *Acs Nano.* **2011**, 5, 8013-8018.

37. Geszke-Moritz, M.; Piotrowska, H.; Murias, M.; Balan, L.; Moritz, M.; Lulek, J.; Schneider, R. Thioglycerol-capped Mn-doped ZnS quantum dot bioconjugates as efficient two-photon fluorescent nano-probes for bioimaging. *Journal of Materials Chemistry B.* **2013**, 1, 698-706.

38. Gonzalez, C. M.; Wu, W. C.; Tracy, J. B.; Martin, B. Photochemical synthesis of size-tailored hexagonal ZnS quantum dots. *Chem Commun (Camb).* **2015**, 51, 3087-90.

39. Lu, X. D.; Yang, J.; Fu, Y. Q.; Liu, Q. Q.; Qi, B.; Lu, C. L.; Su, Z. M. White light emission from Mn2+ doped ZnS nanocrystals through the surface chelating of 8-hydroxyquinoline-5-sulfonic acid. *Nanotechnology.* **2010**, 21.

40. Talapin, D. V.; Lee, J. S.; Kovalenko, M. V.; Shevchenko, E. V. Prospects of Colloidal Nanocrystals for Electronic and Optoelectronic Applications. *Chemical Reviews.* **2010**, 110, 389-458.

41. Lee, J.; Lim, K. H.; Kim, Y. S. Effects of Unusual Gate Current on the Electrical Properties of Oxide Thin-Film Transistors. *Scientific Reports.* **2018**, 8.

42. D'Amico, P.; Calzolari, A.; Ruini, A.; Catellani, A. New energy with ZnS: novel applications for a standard transparent compound. *Scientific Reports.* **2017**, 7.

43. May, J. W.; McMorris, R. J.; Li, X. S. Ferromagnetism in p-Type Manganese-Doped Zinc Oxide Quantum Dots. *Journal of Physical Chemistry Letters.* **2012**, 3, 1374-1380.

44. Song, H. S.; Zhang, W. J.; Yuan, G. D.; He, Z. B.; Zhang, W. F.; Tang, Y. B.; Luo, L. B.; Lee, C. S.; Bello, I.; Lee, S. T. p-type conduction in arsenic-doped ZnSe nanowires. *Applied Physics Letters.* **2009**, 95.

45. Peng, Q. A.; Jie, J. S.; Xie, C.; Wang, L.; Zhang, X. W.; Wu, D.; Yu, Y. Q. Nano-Schottky barrier diodes based on Sb-doped ZnS nanoribbons with controlled p-type conductivity. *Applied Physics Letters.* **2011**, 98.

46. Kulkarni, A. P.; Tonzola, C. J.; Babel, A.; Jenekhe, S. A. Electron transport materials for organic light-emitting diodes. *Chemistry of Materials.* **2004**, 16, 4556-4573.

47. Li, S. D.; Lu, J.; Xu, J.; Dang, S. L.; Evans, D. G.; Duan, X. Bis(8-hydroxyquinolate-5-sulfonate)zinc intercalated layered double hydroxide and its controllable luminescent properties. *Journal of Materials Chemistry.* **2010**, 20, 9718-9725.

48. Sapochak, L. S.; Benincasa, F. E.; Schofield, R. S.; Baker, J. L.; Riccio, K. K. C.; Fogarty, D.; Kohlmann, H.; Ferris, K. F.; Burrows, P. E. Electroluminescent zinc(II) bis(8-hydroxyquinoline): Structural effects on electronic states and device performance. *Journal of the American Chemical Society.* **2002**, 124, 6119-6125.

49. Bhandari, S.; Roy, S.; Pramanik, S.; Chattopadhyay, A. Double Channel Emission from a Redox Active Single Component Quantum Dot Complex. *Langmuir.* **2015**, 31, 551-561.

50. Soroka, K.; Vithanage, R. S.; Phillips, D. A.; Walker, B.; Dasgupta, P. K. Fluorescence Properties of Metal-Complexes of 8-Hydroxyquinoline-5-Sulfonic Acid and Chromatographic Applications. *Analytical Chemistry.* **1987**, 59, 629-636.

51. Mitra, S.; Pak, Y.; Alaal, N.; Hedhili, M. N.; Almalawi, D. R.; Alwadai, N.; Loganathan, K.; Kumarasan, Y.; Lim, N.; Jung, G. Y.; Roqan, I. S. Novel P-Type Wide Bandgap Manganese Oxide Quantum Dots Operating at Deep UV Range for Optoelectronic Devices. *Advanced Optical Materials.* **2019**, 7, 1900801.

52. Zheng, J. J.; Ji, W. Y.; Wang, X. Y.; Ikezawa, M.; Jing, P. T.; Liu, X. Y.; Li, H. B.; Zhao, J. L.; Masumoto, Y. Improved Photoluminescence of MnS/ZnS Core/Shell Nanocrystals by Controlling Diffusion of Mn Ions into the ZnS Shell. *Journal of Physical Chemistry C.* **2010**, 114, 15331-15336.

53. Cao, S.; Li, C. M.; Wang, L.; Shang, M. H.; Wei, G. D.; Zheng, J. J.; Yang, W. Y. Long-lived and Well-resolved Mn2+ Ion Emissions in CuInS-ZnS Quantum Dots. *Scientific Reports.* **2014**, 4.

54. Maiti, S.; Chen, H. Y.; Park, Y.; Son, D. H. Evidence for the Ligand-Assisted Energy Transfer from Trapped Exciton to Dopant in Mn-Doped CdS/ZnS Semiconductor Nanocrystals. *Journal of Physical Chemistry C.* **2014**, 118, 18226-18232.

55. Whitham, K.; Yang, J.; Savitzky, B. H.; Kourkoutis, L. F.; Wise, F.; Hanrath, T. Charge transport and localization in atomically coherent quantum dot solids. *Nat Mater.* **2016**, 15, 557-63.

56. Han, L.; Balazs, D. M.; Shulga, A. G.; Abdu-Aguye, M.; Ma, W. L.; Loi, M. A. PbSe Nanorod Field-Effect Transistors: Room- and Low-Temperature Performance. *Advanced Electronic Materials.* **2018**, 4.

Appendix A

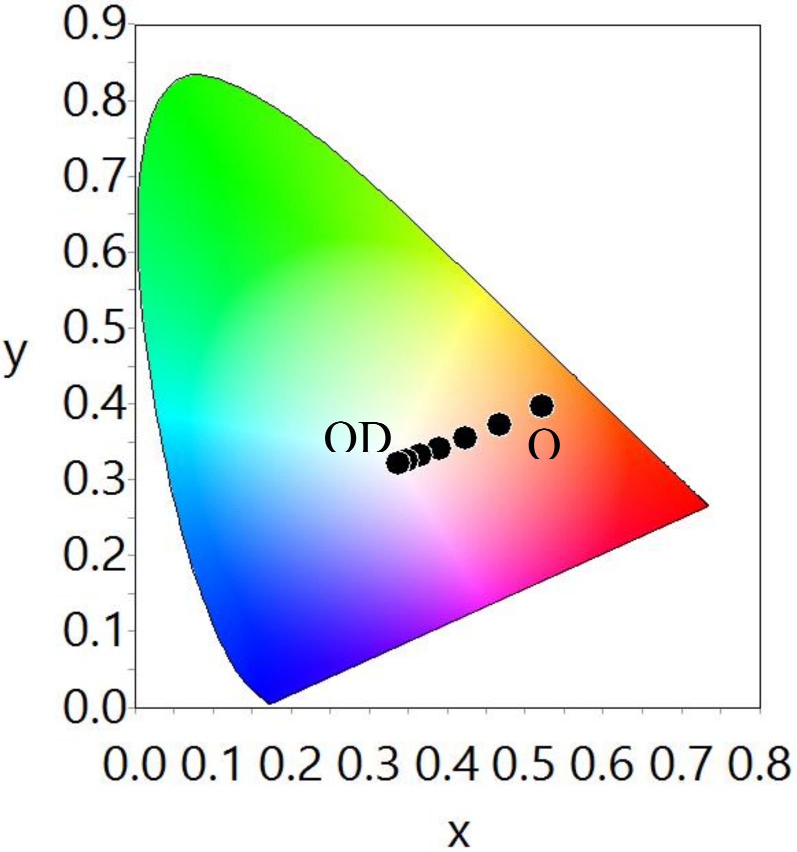

Figure A2.1. CIE diagram of (i) 00, (ii) 0.99 µM, (iii) 1.99 µM, (iv) 2.99 µM, (v) 3.98 µM, (vi) 4.97 µM, (vii) 5.96 µM, HQS added to Mn^{2+}doped ZnS Qdot.

Table A1. Tabulated form of white light emission parameters (CIE, CRI and CCT) of (i) 0.0, (ii) 0.99 µM, (iii) 1.99 µM, (iv) 2.99 µM, (v) 3.98 µM, (vi) 4.97 µM, (vii) 5.96 µM HQS treated Mn^{2+} doped ZnS Qdot

Sample	**CIE**	**CRI**	**CCT (K)**
Qdot	0.52, 0.40	41	1939
Qdot + 0.99 µM HQS	0.47 , 0.37	55	2305
Qdot + 1.99 µM HQS	0.42, 0.35	64	2785
Qdot + 2.99 µM HQS	0.39, 0.34	71	3399
Qdot + 3.98 µM HQS	0.37, 0.33	75	4060
Qdot + 4.97 µM HQS	0.35, 0.32	77	4719
Qdot + 5.96 µM HQS	0.34, 0.33	78	5220

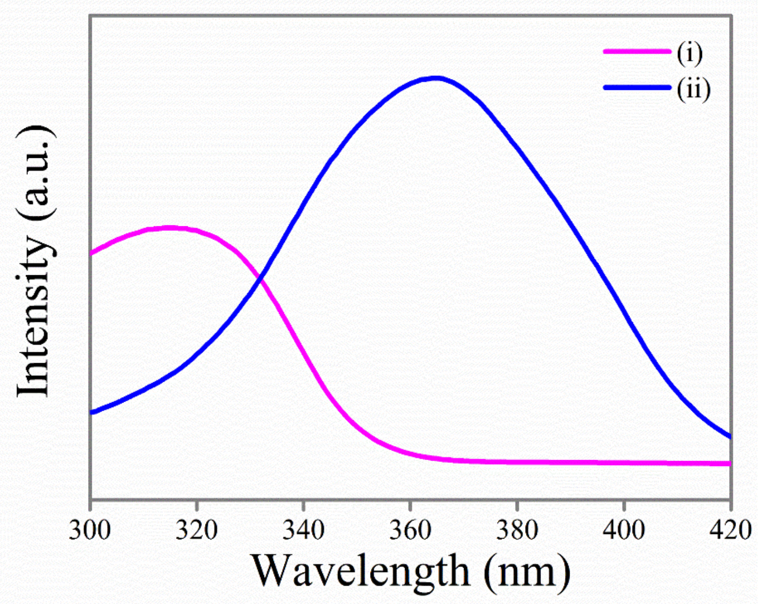

Figure A2.2. Excitation spectra of (i) Mn^{2+} doped ZnS Qdot and (ii) HQS surface complexed Mn^{2+} doped ZnS Qdot for emission maxima at 595 nm and 480 nm respectively.

Quantum yield

The following formula was used to calculate the quantum yields (QYs) of quantum dot and quantum dot complex where quinine sulphate was used as the reference

$$Q_S = Q_R \times \frac{I_S}{I_R} \times \frac{A_R}{A_S} \times \frac{\eta^2{}_S}{\eta^2{}_R} \qquad \textbf{(A2.1)}$$

Where, Q_S is the quantum yield of the sample; Q_R = quantum yield of the reference; I_S = area under emission curve of sample; I_R = area under emission curve of reference; A_R = absorbance of reference; A_S = absorbance of sample; η_s = refractive index of sample; η_R = refractive index of reference. QY of quinine sulphate = 0.54 (54 %). The concentration of quinine sulphate and the samples were adjusted so as to achieve an absorbance of 0.1 ± 0.01 when irradiated with excitation wavelength of 330 nm and all the emission spectra were recorded between 400-700 nm.

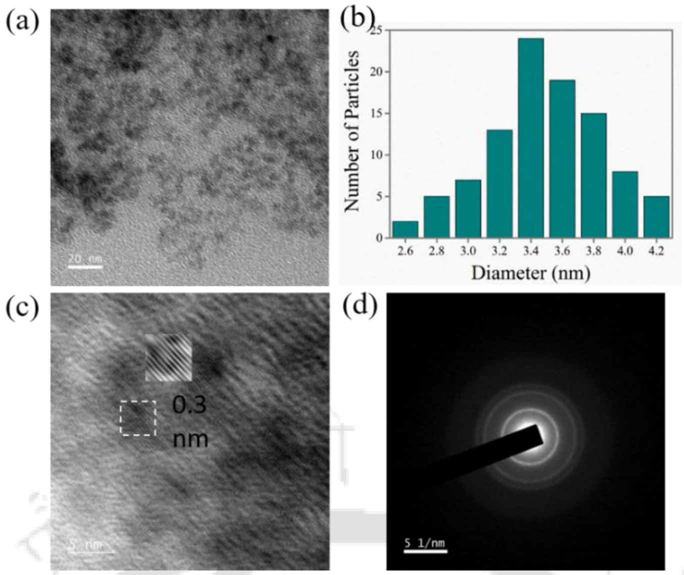

Figure A2.3. (a) TEM image (scale bar 20 nm), (b) corresponding particle size distribution and (c) HRTEM image (scale bar 5nm) (inset: IFFT image of corresponding marked area) with lattice fringe spacing 0.3 nm and (d) SAED pattern of 5.96 µM HQS added Mn^{2+}doped ZnS Qdot.

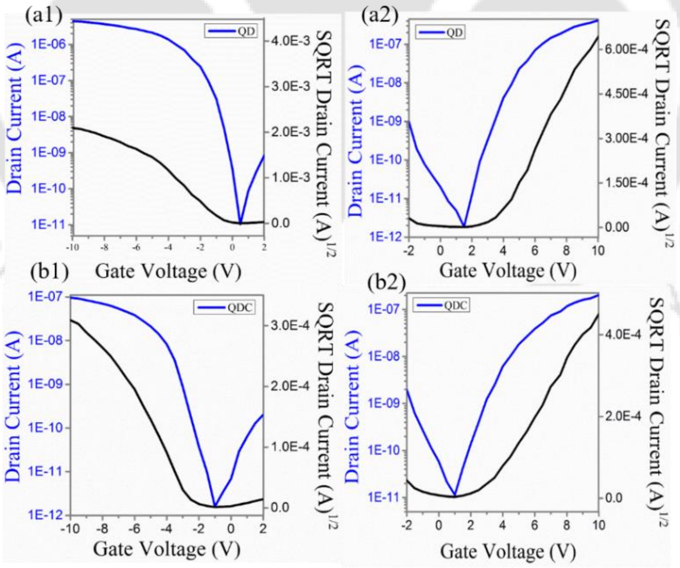

Figure A2.4. Transfer characteristic curves of (a) Qdot-TFT and (b) QDC-TFT when operated as a (1) p-FET and (2) n-FET in logarithmic drain current and square root of drain current (vertical axis) vs linear gate voltage. (corresponding to the data of Figure 2.5 a,b).

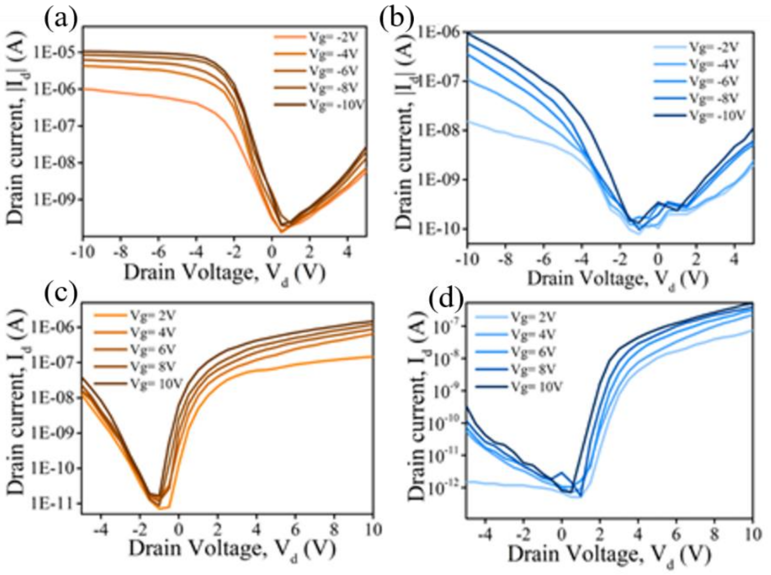

Figure A2.5. Comparison of Output curves of (a) Qdot-TFT (p-FET), (b) QDC-TFT (p-FET), (c) Qdot-TFT (n-FET) and (b) QDC-TFT (n-FET).

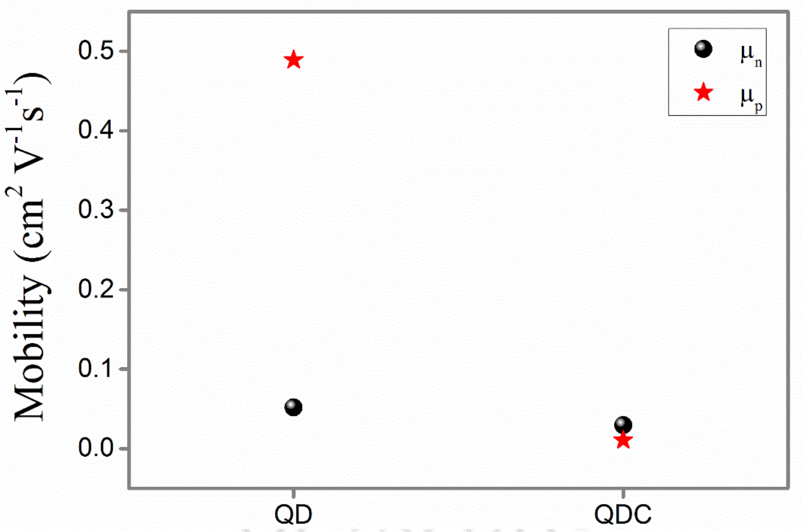

Figure A2.6. Comparison of carrier mobility of Qdot-TFT ($\mu_n = 5.20\times10^{-02}$ and $\mu_p = 4.89\times10^{-01}$ $cm^2V^{-1}s^{-1}$) and QDC-TFT. ($\mu_n = 2.95\times10^{-02}$ $cm^2V^{-1}s^{-1}$ and $\mu_p = 1.06\times10^{-02}$ $cm^2V^{-1}s^{-1}$).

Table A2. Comparison of different quantum dot transistors

Ref. No.	Type of Dot	Type of transport	Mobility ($cm^2 V^{-1}.s^{-1}$)	I_{ON}/I_{OFF}	Subthreshold swing (V.dec^{-1})	Toxicity
This Work	Mn^{2+} doped ZnS Qdot	Ambipolar	4.89E-01 (μ_p) 5.20E-02 (μ_n)	10^5	0.355(p-channel) 0.595(n-channel)	Non-toxic
	Mn^{2+} doped ZnS QDC	Ambipolar	1.06E-02 (μ_p) 2.95E-02 (μ_n)	10^4	0.798(p-channel) 0.970(n-channel	Non-toxic
1	PbS Qdot	Ambipolar	0.06 (μ_n)	10^4	-	toxic
2	CdSe Qdots $In_2Se_4^{2-}$ ligand	n-type	44 (μ_n)	10^5	-	Toxic
3	PbS/HMDS treated Qdot	Ambipolar	0.2 (μ_n) 8X10^{-5}(μ_p)	10^5 /10^6	2.71	toxic
4	PbSe Qdots	Ambipolar	7 (μ_n) 0.6(μ_p)	10^3	-	Toxic
5	PbS colloidal Qdot	Ambipolar	0.12(μ_n) 10^{-5}(μ_p)	$10^6/10^3$	-	Toxic
6	PbS Qdot (thiocyanate caped)	Ambipolar	0.13 / 0.33	-	-	toxic
7	benzyl viologen doped PbS Qdot	n-type	0.64	-	-	toxic
8	PbS Qdot (Thiocyanate treated)	Ambipolar	0.43 0.47	10^3	-	toxic
9	PbS Qdot	Ambipolar		10^4	0.250 - 0.450	Toxic

Subthreshold Swing

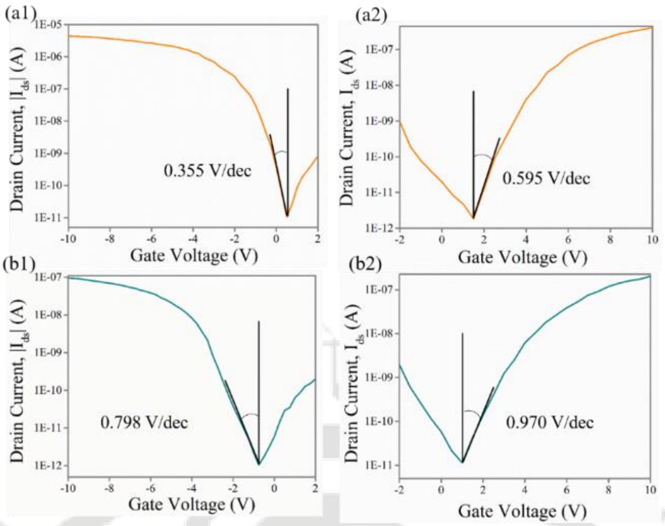

Figure A2.7. Subthreshold slopes of (a1) Qdot-TFT (p-channel), (a2) Qdot-TFT (n-channel), (b1) QDC-TFT (p-channel) and (b2) QDC-TFT (n-channel).

The following formula was used to calculate the density of trap states in the transistors from the subthreshold swing obtained from the experimental data

$$\text{Subthreshold Swing (SS)} = \ln(10)\frac{kT}{q}\left(1+\frac{q^2D_{it}}{C_i}\right) \qquad \textbf{(A2.2)}$$

Where k is the Boltzmann constant; q is the elementary charge; T is the absolute temperature; C_i is the unit area dielectric capacitance and D_{it} is the density of interface trap states.

Table A3. Trap state densities of Qdot-TFT and QDC-TFT

	Trap state density (D_{it} (cm^{-2}.eV^{-1})	
Samples	p-FET	n-FET
Qdot-TFT	2.97×10^{11}	5.59×10^{11}
QDC-TFT	9.24×10^{11}	9.40×10^{11}

Decay parameters of the samples were fitted (tri-exponentially) and average life time of the samples were calculated by using the equation (3) and (4) respectively

$$I(t) = \sum_i \alpha_i \exp\left(-{}^{t}/_{\tau_i}\right) \qquad \textbf{(A2.3)}$$

$$\tau_{av} = \frac{\sum_i \propto_i \tau_i^{2}}{\sum_i \propto_i \tau_i} \qquad \textbf{(A2.4)}$$

Where, α and τ, are the exponential coefficients and excited-state lifetime of the component. Time-resolved photoluminescence studies were carried out using life-Spec-II spectrofluorometer (Edinburgh Instrument) and HORIBA-Fluoromax4 spectrofluorometer.

Table A4. Average life time of Qdot and QDC in colloidal phase and thin film.

λ_{ex} (nm)	λ_{em} (nm)	Qdot colloid	Qdot Thin Film	QDC colloid	QDC Thin Film
336	480	-	-	14.73 ns	8.76 ns
375	480			15.02 ns	8.46 ns
330	595	1.47 ms	1.24 ms	1.50 ms	1.17 ms

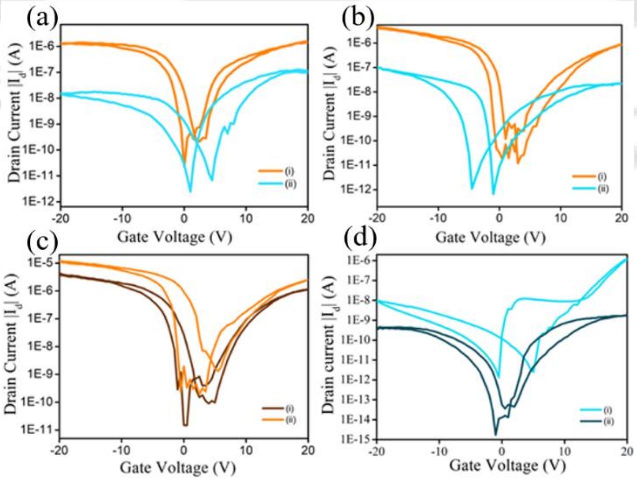

Figure A2.8. Hysteresis plot of (i) Qdot and (ii) QDC at room temperature for (a) V_d=+10V and (b) V_d= -10V. Hysteresis plot for V_d= +10V at (i) 77K and (ii) 357K of (c) Qdot-TFT and (d) QDC-TFT.

References

1. Shulga, A. G.; Kahmann, S.; Dirin, D. N.; Graf, A.; Zaumseil, J.; Kovalenko, M. V.; Loi, M. A. Electroluminescence Generation in PbS Quantum Dot Light-Emitting Field-Effect Transistors with Solid-State Gating. *Acs Nano*. 2018, 12, 12805-12813.
2. Jung, S. M.; Kang, H. L.; Won, J. K.; Kim, J.; Hwang, C.; Ahn, K.; Chung, I.; Ju, B. K.; Kim, M. G.; Park, S. K. High-Performance Quantum Dot Thin-Film Transistors with Environmentally Benign Surface Functionalization and Robust Defect Passivation. *Acs Applied Materials & Interfaces*. 2018, 10, 3739-3749.
3. Nugraha, M. I.; Hausermann, R.; Bisri, S. Z.; Matsui, H.; Sytnyk, M.; Heiss, W.; Takeya, J.; Loi, M. A. High Mobility and Low Density of Trap States in Dual-Solid-Gated PbS Nanocrystal Field-Effect Transistors. *Advanced Materials*. 2015, 27, 2107-2112.
4. Liu, Y.; Tolentino, J.; Gibbs, M.; Ihly, R.; Perkins, C. L.; Liu, Y.; Crawford, N.; Hemminger, J. C.; Law, M. PbSe Quantum Dot Field-Effect Transistors with Air-Stable Electron Mobilities above 7 cm(2) V-1 s(-1). *Nano Letters*. 2013, 13, 1578-1587.
5. Balazs, D. M.; Rizkia, N.; Fang, H. H.; Dirin, D. N.; Momand, J.; Kooi, B. J.; Kovalenko, M. V.; Loi, M. A. Colloidal Quantum Dot Inks for Single-Step-Fabricated Field-Effect Transistors: The Importance of Postdeposition Ligand Removal. *Acs Applied Materials & Interfaces*. 2018, 10, 5626-5632.
6. Koh, W. K.; Saudari, S. R.; Fafarman, A. T.; Kagan, C. R.; Murray, C. B. Thiocyanate-Capped PbS Nanocubes: Ambipolar Transport Enables Quantum Dot Based Circuits on a Flexible Substrate. *Nano Letters*. 2011, 11, 4764-4767.
7. Nugraha, M. I.; Kumagai, S.; Watanabe, S.; Sytnyk, M.; Heiss, W.; Loi, M. A.; Takeya, J. Enabling Ambipolar to Heavy n-Type Transport in PbS Quantum Dot Solids through Doping with Organic Molecules. *Acs Applied Materials & Interfaces*. 2017, 9, 18039-18045.
8. Jo, C. H.; Kim, J. H.; Kim, J.; Kim, J.; Oh, M. S.; Kang, M. S.; Kim, M. G.; Kim, Y. H.; Ju, B. K.; Park, S. K. Low-temperature annealed PbS quantum dot films for scalable and flexible ambipolar thin-film-transistors and circuits. *Journal of Materials Chemistry C*. 2014, 2, 10305-10311.
9. Stadler, P.; Sutherland, B. R.; Ren, Y.; Ning, Z. J.; Simchi, A.; Thon, S. M.; Hoogland, S.; Sargent, E. H. Joint Mapping of Mobility and Trap Density in Colloidal Quantum Dot Solids. *Acs Nano*. 2013, 7, 5757-5762.

Chapter 3

Surface Engineering of Quantum Dot for Self-Powered Ultraviolet Photodetection and Information Encryption

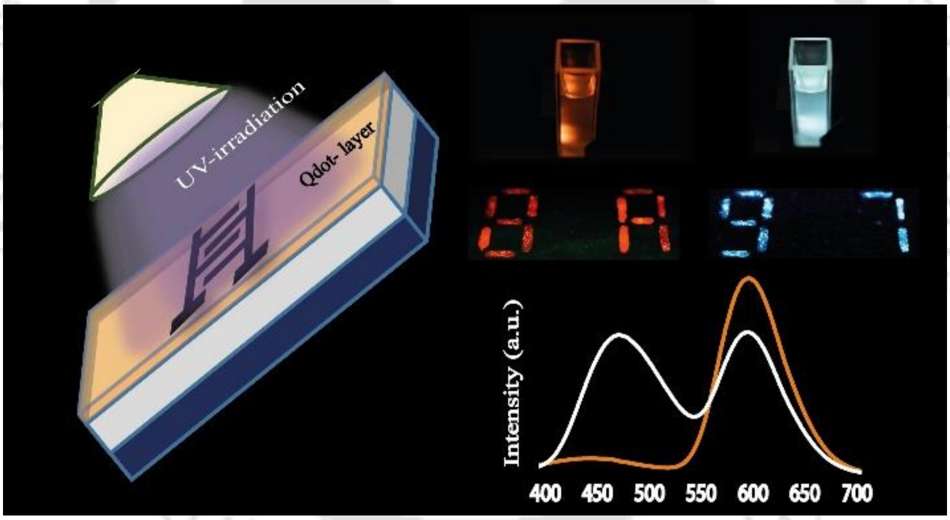

[K. Gogoi, A. Chattopadhyay, Langmuir. 2022, 38, 2668-2676]


भारतीय प्रौद्योगिकी संस्थान गुवाहाटी
Indian Institute of Technology Guwahati

Chapter 3

Surface Engineering of Quantum Dot for Self-Powered Ultraviolet Photodetection and Information Encryption

Abstract

We demonstrate fabrication of photodetectors in the UVC and UVA regions, based on surface engineering of Mn^{2+} doped ZnS Qdot. Mn^{2+} doped ZnS Qdot, exhibited UVC detection with responsivity 0.3±0.02 $A.W^{-1}$ and detectivity 1.7±0.2 10^{11} Jones. Following this, the Qdot was surface modified with 8-hydroxyquinoline 5-sulphonic acid ligand, which resulted in the formation of bluish green zinc quinolate complex ($Zn(QS)_2$) at the Qdot surface (defined as quantum dot complex; QDC) exhibiting overall white photoluminescence. The detector developed with QDC as the photoactive material, exhibited responsivity of 0.2±0.02 $A.W^{-1}$ and detectivity of 1.2±0.2 10^{11} Jones in UVA band. This shift in the detection band from UVC in Qdot to UVA in QDC, through surface complexation mechanism is a new approach for tuning spectral detection featured in this work. Besides, the self-powered response of both the detectors exhibited attractive photoelectric characteristics. The detectors were incorporated in a portable prototype to show their potential application towards selective UVC and UVA spectral detection. Additionally, the dual- mode emission of the QDC was used for data encryption and decryption.

3.1 Introduction

Easy fabrication and commercially viable ultraviolet (UV) photodetectors - that are selective to different bands of UV radiations - could make significant difference to a plethora of applications. They are especially important in remote control devices, defence safety gears, ozone layer monitoring, flame detection, secured space communications, UV-phototherapy and personal monitoring devices.[1-4] Recent results suggest that wide bandgap nanoscale materials - with strong absorption in the UV region - such as GaN nanofibres[5], Ga_2O_3,[6] $Ga_2In_4S_9$[7], single walled carbon nanotube,[8] TiO_2 nanorod,[9] ZnO nanocrystals[10] and ZnS nanobelts[11] may provide important options for fabrication of optoelectronic UV detectors.[12] A promising detector element ought to be able to generate - following UV exposure – long lived exciton(s) and at the same time serve as efficient charge carrier in the device. Current developments in zero - dimensional quantum dot (Qdot) based UV photodetectors have exhibited superior performance over one dimensional nanocrystals because of their added advantage of increased surface to volume ratio and multiple exciton generation.[2, 13, 14] Further, the photoexcited carriers with energy higher than the band gap of the photoactive material generate secondary excitons, which in turn increases the photocurrent yield. Significant improvements in carrier drift towards external electrodes and thus the device performance have been achieved by integrating Qdots with 2D films such as that of graphene or MoS_2 in hetero-structured design, with graphene and MoS_2 being excellent agents for high mobility charge transport.[15-17]

ZnS Qdots, a potential candidate for solar blind nears deep (265 nm) ultraviolet detection, showed improved performance for detection of 290 nm light when incorporated into graphene heterstructure.[17] Self-powered detectors based on nanostructured ZnS caught tremendous interest, where asymmetric Schottky contacts reportedly facilitated zero voltage operation due to the built in electric field. Commonly studied self-powered UV photodetectors implement p-n junctions,[6] heterojunctions,[18] Schottky junctions,[19] or organic/polymer hybrid junction[20] structures, which rapidly separate the photoexcited electrons and holes due to the built-in electric field.[3, 21, 22] Schottky junctions in metal-semiconductor-metal (MSM) detectors, the simplest of all the kind in the context of fabrication complexity, have shown tremendous improvement in detector performance.[3] Additionally, transition metal ions when doped in Qdot crystal introduce intermediate electronic states in the band gap, which help improve the charge separation and recombination dynamics in the photoactive material.[23, 24] However, the effect of Mn^{2+} doping in ZnS Qdot to enhance the photodetector performance under self-powered operation is not reported before.

Importantly, ligand exchange methods, in addition to surface passivation, facilitate fast electron injection, improves photoluminescence efficiency and interdot coupling and device stability.[25-29] In addition, they provide control over exciton dynamics, detection range and improve electrode to excitonic barrier for wide range of device interfaces and thus have improved performance significantly over high quantum yield photodetectors.[30, 31] . On the other hand, species such as molecular complexes when incorporated on the surface of Qdots not only would help passivate the surface but also improve the versality and performance of the device.[27, 32] We have recently defined such a composite as quantum-dot-complex (QDC) and have shown that they possess physical properties superior to the component Qdot or the complex.[33, 34] It could be plausible that a QDC would exhibit different charge transport properties as compared to the Qdot or the complex and thus may help fabricate superior photodetectors.[35] Such an approach in bringing versatility to the optoelectronic properties of Qdots through the complexation on their surfaces has not been reported yet.

Herein, we report fabrication of MSM photodetectors with Mn^{2+} doped ZnS Qdot and QDC as the photoactive materials. We report tuning of detection band from UVC in Qdot detector to UVA in QDC detector by modulating absorption and excitation dynamics through surface engineering. The Qdot- photodetector (Qdot-PD) have exhibited maximum as-measured detection at 255 nm wavelength (UVC) with responsivity of 0.3±0.02 $A.W^{-1}$ and detectivity of 1.7±0.2 10^{11} Jones whereas the QDC-photodetector (QDC-PD) has exhibited maximum photoresponse at 365 nm (UVA) with responsivity of 0.2±0.02 $A.W^{-1}$ and detectivity of 1.2±0.2 10^{11} Jones. The detectors were analysed under self-biased conditions, which produced responsivity 9 mA/W in Qdot-PD and 4 mA/W in QDC-PD. Both detectors were then integrated together with a microcontroller unit to build a portable prototype where the photocurrent generated from the detectors are calibrated so as to selectively detect UVA and UVC radiations. Thus. we propose here that surface complexation with ligands on quantum dot surfaces provides a new tool to engineer charge carrier dynamics to tune detection band. In addition, the dual-mode photoluminescence properties of QDC was utilized for a novel information encryption.

3.2 Materials and Methods

Materials

zinc acetate dihydrate (Merck), manganese acetate tetrahydrate (Merck), sodium sulphide (Merck), 8-hydroxyquinoline-5-sulfonic acid (Merck), methanol (Merck) and Mili-Q grade water.

Mn^{2+} doped ZnS quantum dot (Qdot) Synthesis: A reported synthesis protocol was followed for the preparation of Mn^{2+} doped ZnS quantum dots which is characteristic of orange emission (595 nm) at $\lambda_{ex=}$330 nm.[33] In detail, 40 mL homogeneous aqueous mixture of zinc acetate dehydrate and manganese acetate tetrahydrate with concentration of 5mM and 1mM respectively were constantly stirred for 10 min at 80 °C. Following this, 10mL solution of 5.0 mM sodium sulphide was added to the mixture and allowed to undergo reaction for 4 h at 120 °C under reflux conditions. The so obtained, milky white dispersion was centrifuged for 20 min at 15000 rpm. The resultant palette was dispersed in Milli Q water, and centrifuged-keeping the rotational speed and duration constant. The resultant palette was re-dispersed in 50 mL methanol for further experiments.

Preparation of HQS ligand: The solvent used for preparation of the ligand is water and methanol mixed at a ratio of 6:4 by volume. To this, 2.24 mg of 8-hydroxyquinoline-5 sulphonic acid (HQS) was added and sonicated to obtain 1mM solution of the ligand.

Preparation of quantum dot complex (QDC): 3.0 µL of 1.0 mM solution of HQS ligand was cumulatively added to the as-synthesised Qdot dispersion. Formation of QDC was confirmed with the appearance of gradually increasing emission peak at 480 nm in photoluminescence spectrum on successive addition of 1 mM HQS solution along with the emission peak of as-synthesised Qdot at 595 nm at $\lambda_{ex=}$330nm. An optimum amount of 15.0 µL of 1.0 mM HQS (5.96 µM) was required to a volume of 3.0 mL Qdot dispersion (with absorption at 320 nm) to ascertain the formation of white light emitting QDC. This colloidal dispersion was then purified by carrying out two rounds of centrifugation at 15000 rpm for 20 min.

Photodetector fabrication: A 1x1 cm piece of Si/SiO_2 substrate was cleaned ultrasonically with acetone, isopropyl alcohol and Mili-Q water sequentially. The cleaned wafer was further treated in ozone plasma for 20 min at room temperature to obtain a hydrophilic surface. A homogeneous dispersion of Qdot was prepared by sonicating 100 mg Qdot palette in 1 mL methanol for 1 h. 100 µL of this dispersion was spin-coated onto properly cleaned Si/SiO_2 wafer at 1000 rpm for 60 s to obtain thin layer of Qdot. It was then heated at 120 °C in a hot plate at ambient air and yellow light condition. Interdigitated electrodes (IDT) were patterned over the quantum dot thin layer by thermal evaporation of 99.99% pure aluminium at 6×10^{-6} mbar chamber pressure through a shadow mask using thermal evaporation system. IDT patterned shadow masks with 100 µm gap between the electrodes were used for Al electrode patterning. The device was then heated at 120 °C in a hot plate at ambient air and yellow light condition.

The QDC photodetector was also fabricated in a similar fashion. Briefly, 100 µL of uniformly dispersed QDC, prepared by sonicating 100 mg of QDC palette in 1mL methanol was spin coated on Si/SiO_2 substrates at 1000 rpm for 60 s to obtain a thin uniform layer of QDC. Thermally evaporated Aluminium electrodes were patterned through shadow masks to obtain the desired optoelectronic output from the photodetectors.

3.3 Instruments Used

Optical Characterization: UV-Vis and photoluminescence spectra of Qdot and QDC were recorded in Jasco V-360 spectrophotometer and Horiba jobin Yvon FluoroMax-4 spectrofluorimeter, respectively.

Morphological Characterization*:* For Transmission electron microscope, high resolution transmission electron microscope (HRTEM) and selected area electron diffraction (SAED) analysis, JEOL JEM-2100F transmission electron microscope was used. Bruker D2 Advance X-ray diffractometer was used to obtain Powder X-ray diffraction patterns. AFM imaging was carried out in Innova SPM, Bruker and FESEM was carried out in JEOL JSM-7610F.

Electrical Characterization: Time dependent photodetector responses were measured in dark room environment at room temperature using Keithley 4200A SCS parameter analyser. Wavelength dependent responses were recorded using Keithley 2400 integrated with Horiba Jobin YVON Fluorolog spectrofluorimeter

3.4 Materials Characterization

Deep UV detectors illustrated in this work were fabricated using solution processed quantum sized Mn^{2+} doped ZnS nanocrystals as the active material. These Qdots exhibited absorbance band edge at 330 nm and a strong absorbance at UVC due to host ZnS (**Figure 3.1a**). Photoluminescence peak at 595 nm observed in the as-synthesized Qdot is attributed to electronic transition of Mn^{2+} dopant from $^4T_1$ state to $^6A_1$ state of Qdot. Appearance of a weaker peak at 440 nm is attributed to the photoluminescence of the host ZnS Qdots (**Figure 3.1b**). The average particle size of Qdot obtained from the transmission electron microscopy (TEM) images was 3.2 ± 0.2 nm along with a lattice fringe spacing of 0.3 nm due to (111) lattice plane of cubic ZnS (**Figure 3.1c-f**). (111), (220) and (311) lattice planes of cubic ZnS were confirmed based on the 2θ peaks at 28.30°, 47.40°, and 56.40°, respectively, observed in the powder X-ray diffraction analysis (**Figure B3.1, Appendix B**). Subsequently, to the colloidal dispersion of Qdot, 8-hydroxyquinoline-5-sulphonic acid (HQS) ligand was added to obtain Qdot complex (QDC).[33] Addition of this ligand to Qdot dispersion involved reaction with the surface cations of Qdot resulting in the formation of zinc quinolate complex ($Zn(QS)_2$) at the Qdot surface, which was confirmed from the emission peak at 480 nm in addition to 595 nm at λ_{ex}= 330 nm. Emission peak at 480 nm is due to electronic transition between highest occupied molecular orbital (HOMO) and lowest unoccupied molecular orbital (LUMO) levels of the surface complex formed.[33] The dual emission peak of QDC makes it white in appearance under 330 nm excitation (**Figure 3.1b, Figure B3.2, Appendix B**).

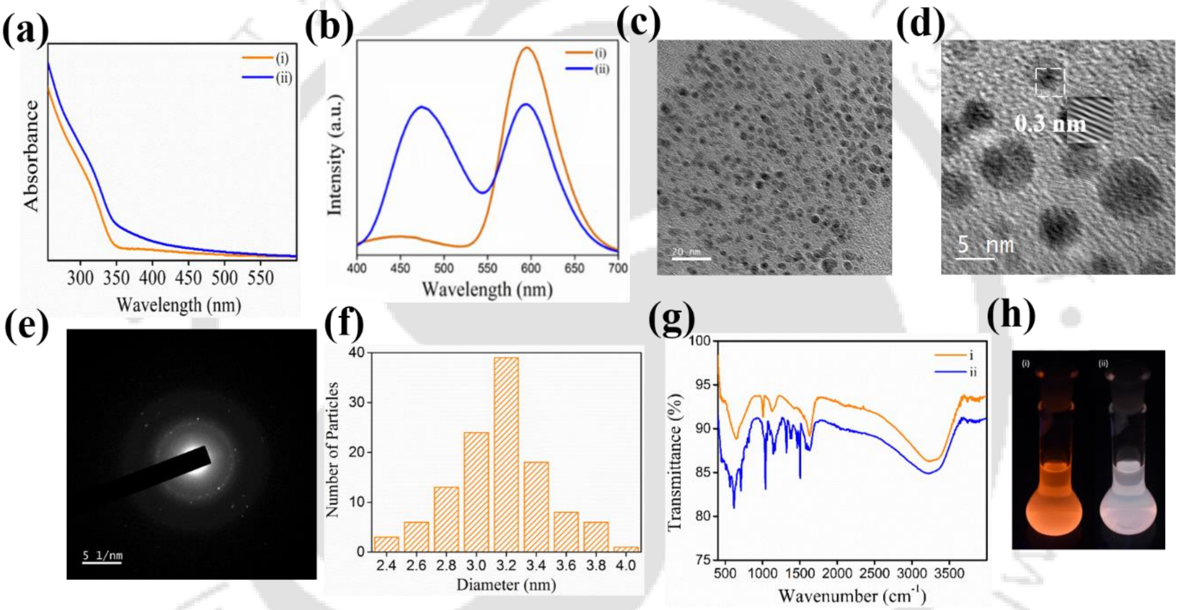

Figure 3.1. (a) UV-vis and (b) photoluminescence spectra of (i) Qdot and (ii) QDC. (c) Transmission Electron Microscopy image (scale bar - 20 nm), (d) high resolution transmission electron microscope image (scale bar - 5 nm) (inset: marked are IFFT image) with lattice fringe spacing 0.3 nm and (e) SAED pattern (f) corresponding particle size distribution of as-synthesized Qdots. (g) Fourier transformed infrared (FTIR) spectra and (h) digital photograph of (i) Mn^{2+} doped ZnS Qdot and (ii) Mn^{2+} Doped ZnS -HQS QDC.

Appearance of an additional hump at 365 nm in the UV-vis spectrum confirmed the attachment of HQS ligand to the bonding sites (**Figure 3.1a**). The Zn^{2+} complexation involved in the quinolate binding on Qdot surface is further confirmed from Fourier transform infrared (FTIR) spectra of QDC (**Figure 3.1g**) and the characteristic peaks at 1602 and 1580 cm^{-1} corresponding to C-C/C-N stretching, 1501 and 1462 cm^{-1} corresponding to pyridyl and phenyl rings, 1320 cm^{-1} corresponding to C-H bending peaks, 819 and 741 cm^{-1} corresponding C-H out plane wagging and 615 cm^{-1} corresponding to in-plane ring deformation were observed. The nature of binding of the quinolate complex on Qdot surface has been previously reported by our group.[36, 37] No change in the average particle size, crystallinity or morphology was observed in the powder XRD analysis and TEM imaging of QDC (**Figure B3.1 and B3.3, Appendix B**). Digital photographs of Qdot and QDC are included in **Figure 3.1h**. The orange emitting Mn^{2+} doped ZnS Qdots and white light emitting QDC were used as the photoactive material to fabricate the Qdot-photodetector (Qdot-PD) and QDC-photodetector (QDC-PD). The colloidal dispersion of Qdots and QDCs were spin coated over a cleaned Si/SiO_2 substrate and interdigitated electrodes were patterned over the active layer using thermal evaporation method. The MSM structured photodetector fabrication process is described in the experimental details.

3.5 Photodetector Characterization

A schematic diagram and the picture of the photodetector is presented in **Figure 3.2a, b**. The surface morphology of the spin coated thin films were studied from the atomic force microscopy (AFM) images and field emission scanning electron microscopy images (FESEM) (**Figure 3.2c-f**). Surface roughness parameters, R_a (roughness average) and R_q (RMS roughness) of the Qdot thin film were found to be 8.69 nm and 10.9 nm, and those of QDC thin film were 6.35 nm and 7.98 nm, respectively. Photoactive materials, when irradiated with energy higher than their band gap produce photogenerated excitons. These excitons then disassociate to electrons and holes and drift toward opposite electrodes under applied electric field resulting in photocurrent yield. The Current (μA) vs Voltage (V) response of Qdot photodetector under UVA, UVC and white light irradiation was obtained for a voltage range from -5V to +5 V as shown in **Figure 3.3a**. From the I-V characteristics, it was clearly observed that, the maximum amount of photocurrent was generated under 255 nm (UVC), followed by 365 nm (UVA) exposer. When exposed to white light, it produced lowest photocurrent compared to the above-mentioned cases. Unlike other reported results, UV-LEDs were used as the illumination source instead of LASER source and incident optical power was kept constant at 0.6 mW/cm^2 throughout all the experiments. To examine repeatability of the detector, it was exposed to 10 ON-OFF cycle of UVC, UVA and white light at a fixed bias voltage of +3V (**Figure 3.3b**). The dark current of the Mn^{2+} doped ZnS Qdot photodetector was measured as 5 x 10^{-7} A. When irradiated, the photocurrent abruptly increased and reached saturation at high conductive state, and exhibited fast decay to a low conductive state when the light source was turned off.

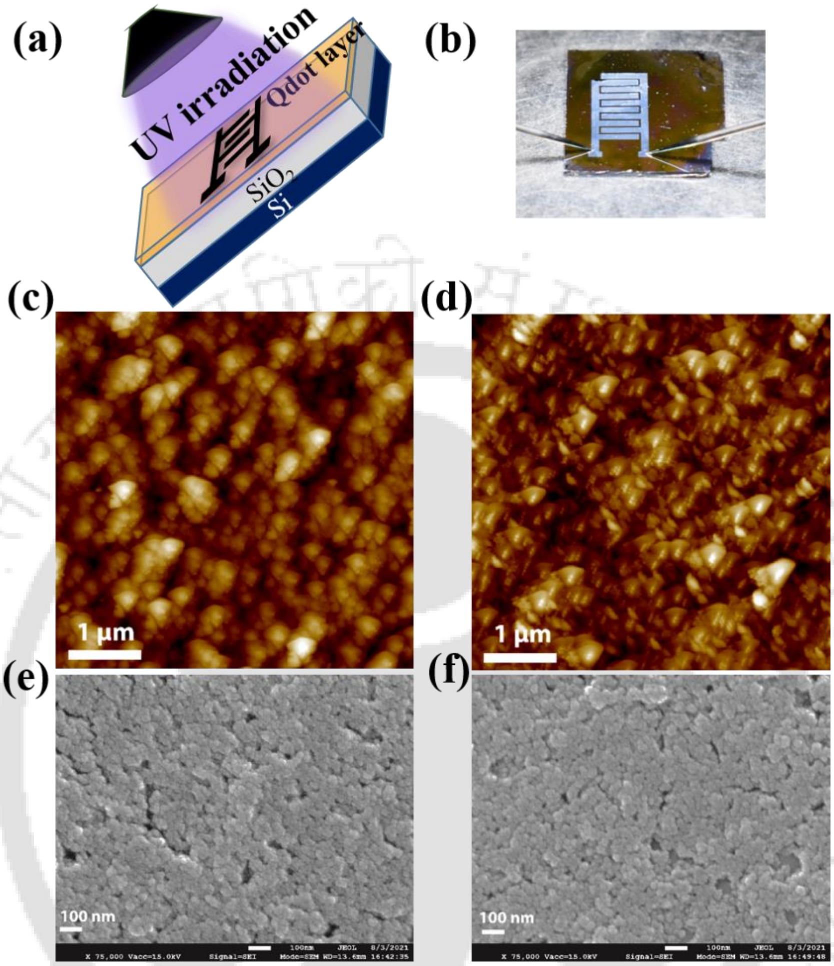

Figure 3.2. (a) Schematic of the fabricated photodetector. (b) A photograph of a typical photodetector. AFM image of spin-cast (c) QD thin film and (d) QDC thin film. FESEM image of spin-cast (e) QD thin film and (f) QDC thin film.

The performance of optoelectronic photodetector is evaluated in terms of two figure of merit parameters, namely, responsivity (R) and specific detectivity (D*). Responsivity quantitatively measures how efficiently a photodetector responds to an optical signal and detectivity represents the capacity of the device to detect the weakest signal. The responsivity and specific Detectivity of photodetector can be calculated using the following equations –

$$Responsivity\ (R) = \frac{I_{ph}}{P_{in}.A} \qquad \textbf{(3.1)}$$

I_{ph} is ($I_{light,ON} - I_{light\ OFF}$), P_{in} represents the total optical power, A represents device area.

The specific Detectivity (D*) of photodetector was calculated using the formula

$$\text{Detectivity, } (D^*)=\frac{A^{1/2}R}{(2qI_d)^{1/2}} \qquad \textbf{(3.2)}$$

A represents device area, R represents responsivity, q represents elementary charge, I_d represents detector dark current.

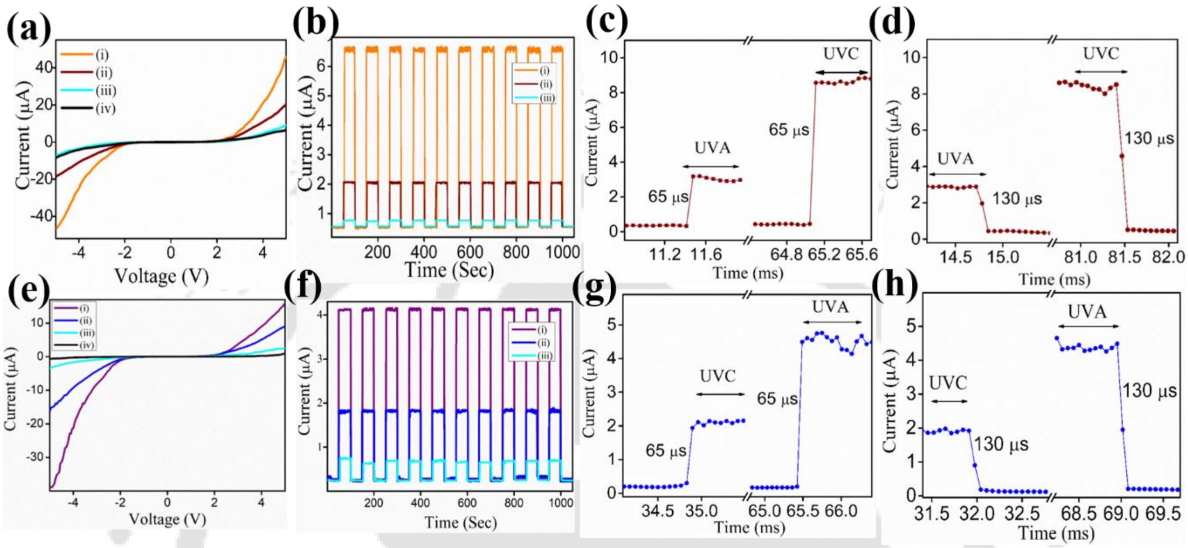

Figure 3.3. (a) I-V curves representing the photoresponses of Qdot-PD upon (i) UVC, (ii) UVA and (iii) white light exposer and (iv) dark current. (b) Photoresponse under ten ON-OFF cycle of (i) UVC, (ii) UVA and (iii) white light exposer. (c) Response time and (d) decay time characteristics of Qdot-PD. (e) I-V curves representing the photoresponses of QDC-PD upon (i) UVA, (ii) UVC and (iii) white light exposer and (iv) dark current. (f) Photoresponse under ten ON-OFF cycle of (i) UVA, (ii) UVC and (iii) white light exposer. (g) Response time and (h) decay time characteristics of QDC-PD.

Upon UVC irradiation with the input optical power 0.6mW/cm^2, the responsivity was found to be 0.3±0.02 A.W^{-1} and upon UVA irradiation it produced a responsivity of 87±23 mA.W^{-1}. The specific detectivity of the detector to UVC exposer is 1.7±0.2 10^{11} Jones in contrast to the smaller value of 4±1 10^{10} Jones to UVA exposer. The transient response of the detector (**Figure 3.3c, d**) showed an average response time of 65μs and a decay time of 130μs to UVC exposer. The response time of 65μs and decay time of 130μs were recorded from the same device under the same biasing condition, when exposed to UVA radiation. The response time (t_r) is the time required for the detector to rise from 10% to 90% of its maximum response whereas decay time (t_d) is the time required time to fall from 90% to 10% of its maximum value. In addition, the detector was not completely blind to visible light as the absorption tail of Qdot extends towards visible light and thus small amount of photocurrent generation was recorded under white light irradiation. The photoresponse of the Qdot-PD is dependent mainly on the drift of photogenerated carriers, therefore the transport of charge carrier in QDot thin film determines the response speed. In solid state Qdot thin films, the transport is dominantly through hopping of the carriers. This leads to low mobility and limited photoresponse transients in Qdot detectors.[38]

To draw a comparison of the photoresponse behaviour, the QDC- PD was tested under the same experimental conditions. I-V characteristics of the QDC-PD were obtained from -5 V to +5 V under UVA, VUC, white light and dark environment (**Figure 3.3e**). The dark current, I_{dark} obtained was 2.1 x 10^{-7} A at +3 V. In contrast to Qdot-PD, QDC-PD exhibited maximum photoresponse under UVA illumination. A stable photocurrent of 4.21 x 10^{-6} A was obtained under this condition. When irradiated with UVC, the photocurrent generated was 1.82 x 10^{-6} A. The responsivity and detectivity of the detector to UVA was 0.2±0.02 A.W^{-1} and 1.2±0.2 10^{11} Jones and to UVC it was 81±10 mA.W^{-1} and 5±1 10^{10} Jones respectively. No degradation of photocurrent was recorded after 10 ON-OFF cycles of UVA and UVC exposer in the detector (**Figure 3.3f**). The average response time and decay time were 65µs and 130µs to UVA and 65µs and 130µs s to UVC exposers, respectively (**Figure 3.3g, h**). Thus it can be ascertained that QDC-PD is a proficient UVA detector with maximum photogenerated current. The detector was not completely visible blind but, the white light response of it ($I_{whitelight}/I_{UVA}$) was found out to be 80% lower in comparison to UVA radiation response. Further, to observe the stability of both the detectors, photoresponse was recorded after 30 days. During this period, they were kept in ambient environment without encapsulation (**Figure 3.4**). The Qdot device retained 80% efficiency whereas QDC device retains 75 % of the initial efficiency, indicating prolonged durability of both the detectors. The excellent durability of detectors can be attributed to highly stable Qdot and QDC.

The photoresponse of ZnS Qdots was measured to analyse the impact of Mn^{2+} dopant on photoconduction. The photoconduction of ZnS Qdot under 255 nm excitation was more than that of 365 nm excitation. Under 365 nm excitation the photocurrent increased and vanished even though the irradiation source was ON. The reason may be that a fraction of the photo-generated excitons dissociated and drifted toward the external electrodes, but majority of the carriers recombined fast and thus did not contribute to photocurrent generation (**Figure B3.4, Appendix B**). The observations depicted that, ZnS Qdot exhibited I_{light}/I_{dark} ratio of 1.13 and doping manganese to ZnS Qdot increased the photocurrent by 11.5 fold. Creation of new electronic states due to Mn^{2+} dopant in the Qdot alters the charge dissociation and recombination dynamics in the material. Previous reports have illustrated long lifetime of Mn^{2+} doped ZnS Qdot in the range of milliseconds due to spin-forbidden d-d transition, $^4T_1$-$^6A_1$ of Manganese[39]. These long lived photogenerated carriers due to Mn^{2+} dopant also introduce a sluggish charge recombination dynamics and thus the enhancement in the resulting photodetector performance. Photoresponse of three representative devices and responsivity as well as detectivity of eight devices are shown in **Figure B3.5, B3.6 and B3.7**, respectively (**Appendix B**).

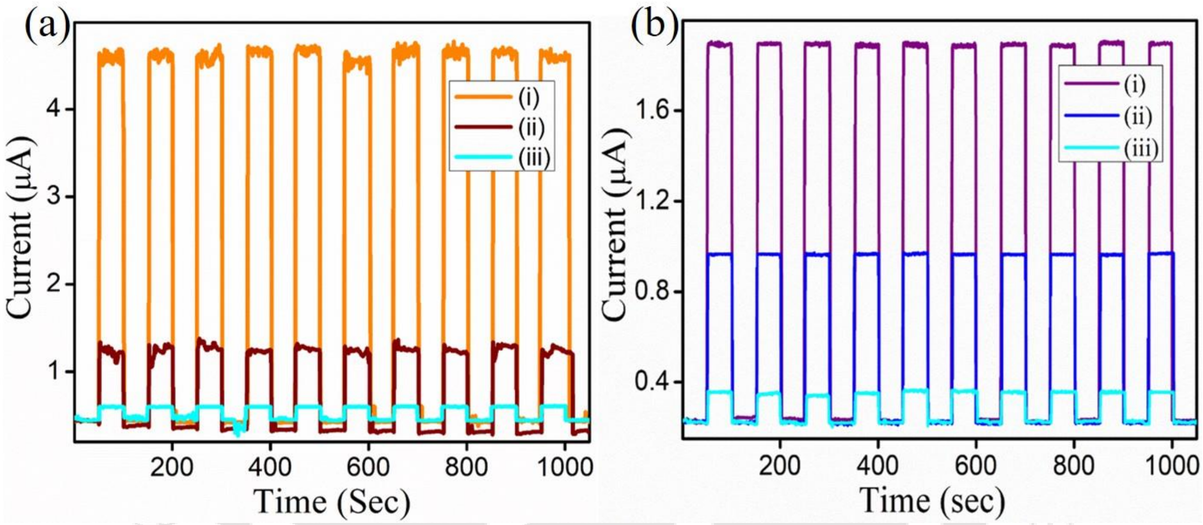

Figure 3.4. (a) Photoresponse of (a) Qdot-PD obtained after 30 days upon (i) UVC, (ii) UVA and (iii) white light illuminations. (b) Photoresponse of (a) QDC-PD obtained after 30 days upon (i) UVA, (ii) UVC and (iii) white light illuminations.

ZnS Qdot being a wide band gap material, exhibits strong absorbance in the UV region. Thus, following illumination with short UV (255 nm) radiation in Mn^{2+} doped ZnS Qdot, excitons are created in the host ZnS, which upon consecutive recombination, transfers the energy to the doping level and creates excited Mn^{2+} ions. These energetic ions can provide energy for the generation of hot carriers at the ZnS conduction band.[40, 41] Another plausible pathway of hot-carrier generation is through Auger de-excitation process where energy is transferred from the excited dopant to a charge carrier leaving the carrier in the excited state and the dopant in ground state.[42, 43] Thus, Mn^{2+} doped ZnS Qdot in a photodetector platform exhibited maximum photocurrent yield on 255 nm exposure. These Qdots when excited with λ_{ex}=365 nm (UVA) produce less photocarriers as the excitation as well as the absorbance at this wavelength is low (**Figure 3.5a**). This is consistent with the observed high photocurrent of 6.59 μA under UVC irradiation compared to a lower value of 2.05 μA under UVA irradiation.

On the other hand, when HQS ligand was sequentially added to the Qdot dispersion, the photoluminescence at 595 nm, when excited with λex= 255 nm (UVC), and owing to the formation of surface complex moiety ($Zn(QS)_2$) on Qdot,[44] was gradually quenched (**Figure B3.8b, Appendix B**), whereas, photoluminescence at 480 nm due to the surface complex moiety with excitation maximum at 365 nm, gradually increased (**Figure B3.8 c, Appendix B**). Excitation spectral plot for both Qdot and QDC are shown in **Figure 3.5a**. As the LUMO level of $Zn(QS)_2$ is close to the conduction band of the doped ZnS,[45] there may be possible energy transfer to the complex. Also, there are two possible channels of recombination, leading to reduction of hot-carrier population in QDC for which excitation maxima was at 365 nm. Due to the presence of surface complex $Zn(QS)_2$, at this wavelength of radiation, the surface complex moiety generates photoexcited carriers, and hence the photocurrent yield. Complex formed from the zinc metallo-8-hydroxyquinolate (ZnQ_2) and ($Zn(QS)_2$ with an electron-withdrawing substituent at 5-position in 8-hydroxyquinoline are reported to be highly photoluminescent and are used as biological probes[46, 47] as well as electroluminescent material for diode and photoswitch applications.[45] Therefore, the complex on the surface of QDC might have acted in efficient charge generation and carrying abilities as observed here. On the other hand, the low photocurrent generated by the QDC at 255 nm was possibly due to efficient energy transfer to the surface complex from the Qdot leading to luminescence by the complex, as is also evident from the excitation spectrum (**Figure 3.5a, Figure B3.8a, Appendix B**). The weaker responsivity in the short UV (255 nm) range may also be attributed to surface charge diffusion barrier and plausible recombinations, limiting charge collection at the electrodes due to formation of surface complexes.[48] Hence, we observe lower responsivity at 255 nm in comparison to 365 nm in QDC-PD. This observation was evident from wavelength dependent responsivity analysis shown in **Figure 3.5b**. From the wavelength-responsivity plot it can be observed that Qdot-PD showed maximum responsivity at UVC region (with continuous increase from longer wavelength, whereas, QDC-PD, exhibited maximum responsivity upon UVA irradiation. This shift in the detection band from UVC in Qdot-PD to UVA in QDC-PD thus can be attributed to the surface complexation of Qdot.

3.6 Self-Powered Operations

In order to validate the self-powered operation of the MSM structured detectors, I-V characteristics of both the detectors were studied. Photocurrent generation in our device can be attributed to the hot carrier generation due to the Mn^{2+} dopant. Due to the rapid transfer of energy between excitons and the Mn^{2+} ions, excitons could be up-converted to hot carrier. These photoexcited hot carriers possessing high kinetic energy, can escape to the electrode producing current even at low intensity photoexcitation without any applied voltage. Photo-generated hot electrons, due to Mn^{2+} dopant potentially exhibits energy above conduction band and even could escape to the vacuum level. Reportedly, they have been potentially used for current generation[49] as well as in photo-catalytic applications.[50] A schematic illustration of hot carrier generation is shown in **Figure 3.6**.

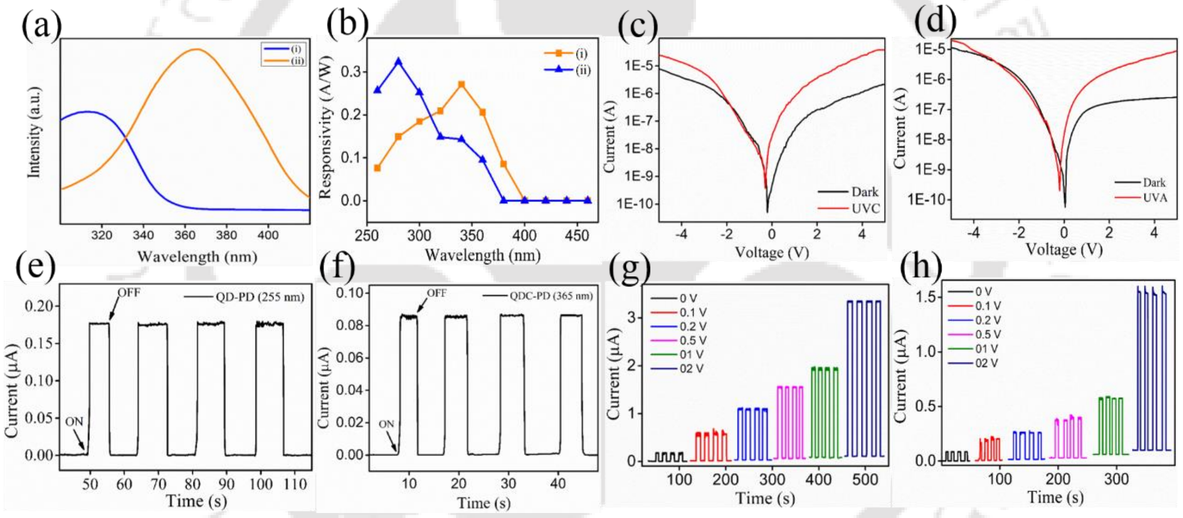

Figure 3.5. (a) Excitation spectra of (i) Qdot (λ_{em}= 595 nm) and (ii) HQS surface complexed Qdot (λem= 480 nm). (b) Wavelength-responsivity curve of (i) QDC-PD and (ii) Qdot-PD. The dark current and photoresponse of (c) Qdot and (d) QDC. Self-powered photoresponse of (e) Qdot and (f) QDC. Photoresponse of (g) Qdot and (h) QDC at different operating voltages.

In addition to this, when the device is operated in ambient conditions, native oxygen molecules get adsorbed at the Mn^{2+} doped ZnS Qdot surface. These oxygen molecules can capture free electrons from the photoactive layer $[O_2(g) + e^- \rightarrow O_2{}^-(ad)]$ and a thin depletion layer is formed at the surface, resulting in an upward band bending at the interface. Upon light illumination, the photoexcited holes migrate to the surface and the negatively charged oxygen is discharged $[O_2{}^-(ad) + h^+ \rightarrow O_2(g)]$ and finally de-adsorbed from the surface. The unpaired free electrons move towards the electrodes resulting in the photocurrent generation. Thus, Oxygen adsorption and de-adsorption process enhances the charge separation at the interface.[3, 22, 51, 52] The dark current and photoresponse of the detectors can be observed in **Figure 3.5c, d**. The device transients are studied at self-powered mode by periodically switching optical signals ON and OFF (**Figure 3.5e, f**).

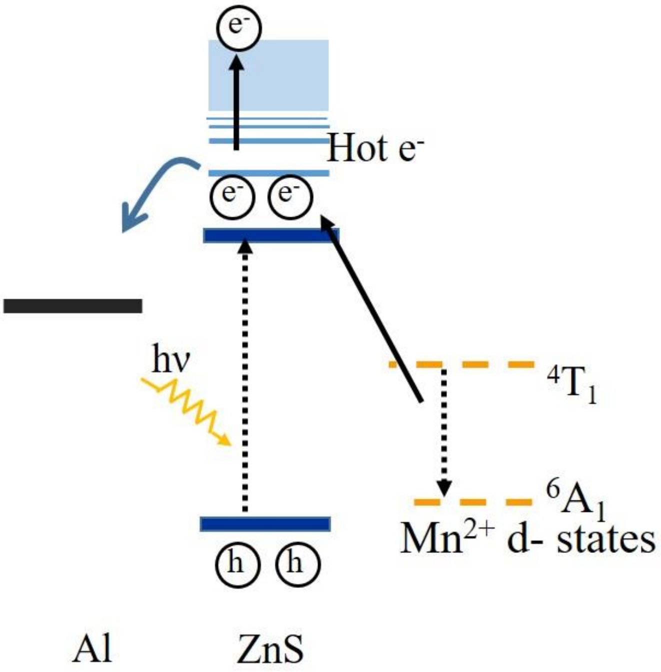

Figure 3.6. Schematic illustration of hot carrier generation in Mn^{2+} doped ZnS-PD.

The self-powered dark current and photocurrent of Qdot-PD were observed to be 5x 10^{-10}A and 1.7x 10^{-7}A and that of QDC-PD was 1x10^{-10}A and 8x10^{-8}A, respectively. Responsivities of 9 mA/W in Qdot-PD and 4 mA/W in QDC-PD were observed under self-biased condition. Detector responses at different operating voltages are shown in **Figure 3.5g, h**. and transient responses under self- biased mode are shown in **Figure B3.9, Appendix B**. The performance parameters of Qdot and QDC are tabulated in **Table B1, Appendix B**. A comparison of performance parameters of recently reported UV photodetectors vis-à-vis the current ones are tabulated in **Table B2, Appendix**.

3.7 Portable Prototype

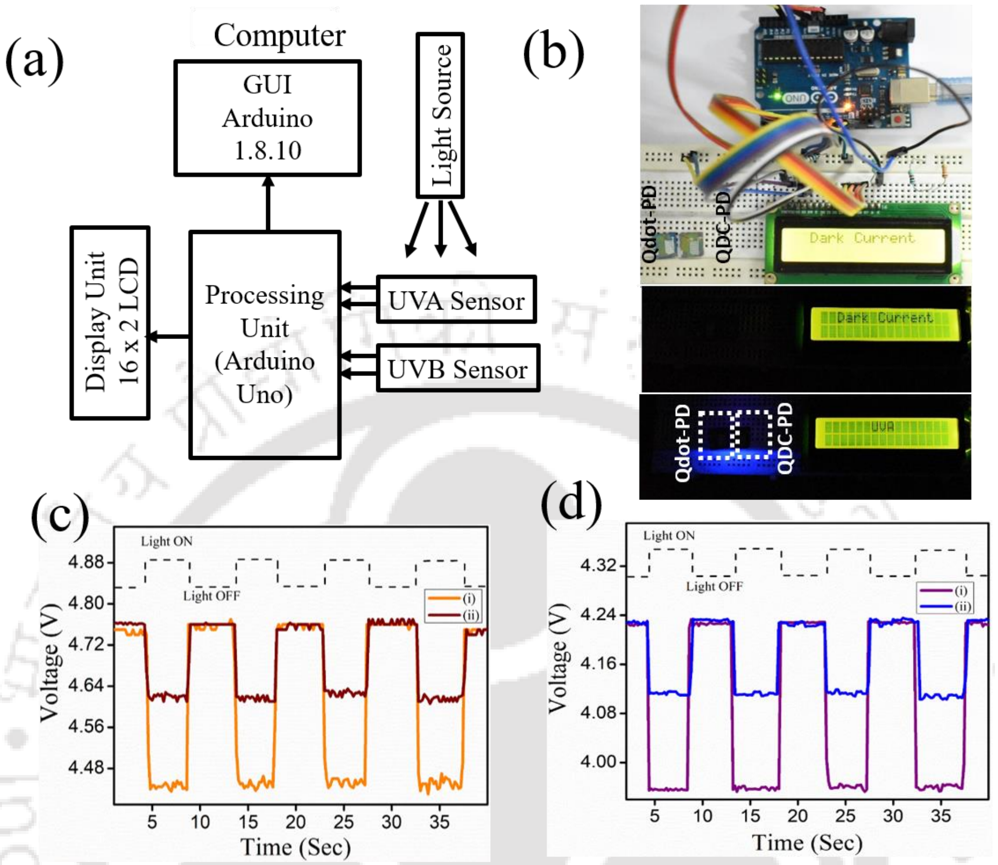

Figure 3.7. (a) Block representation of the connection of the sensors to Arduino UNO and (b) photograph of the integrated device. Time vs Voltage response obtained from the fabricated device using Arduino UNO implementation for (c) Qdot sample with (i) 255 nm and (ii) 365 nm optical irradiations and (d) QDC sample with (i) 365 nm and (ii) 255 nm optical irradiations.

Next, to build a portable working prototype and to obtain the real time responses of the detectors, both the photodetectors were connected to a microcontroller unit. The prototype consisted of a processor (ARDUINO UNO), a computer for graphical user interface and power supply to the controller, a16 x 2 bit LCD and the fabricated UVA and UVC photodetectors. The ratio of voltage change from the detectors were calibrated to display the type of radiation in the display unit. **Figure 3.7a, b** show the block representation and photograph of the prototype. The detectors were connected through voltage divider circuit to the controller unit. The real time response of the detectors in terms of change in voltage across the detectors on exposer to UV radiations were obtained through a graphical user interface. On irradiation of Qdot-PD with UVC radiation, the photocurrent produced was maximum, which reduced the resistance across the detector, and in turn resulted in reduction in voltage across it. The ratio of the voltage across the detector from dark state to light (V_{dark}/ V_{light}) was 1.06 (**Figure 3.7c**). Similarly, when the QDC device was exposed to UVA, it gave a V_{dark}/ V_{light} ratio of 1.07 whereas when exposed to UVC it showed V_{dark}/ V_{light} of 0.86 (**Figure 3.7d**). These observations supported our previous experimental results. Thus, the QDC not only was able to detect UVA radiation in comparison to UVC but also was capable of producing significant difference in signal upon exposure to radiations of two different wavelengths in a commercially viable prototype.

3.8 Information Encryption and Decryption

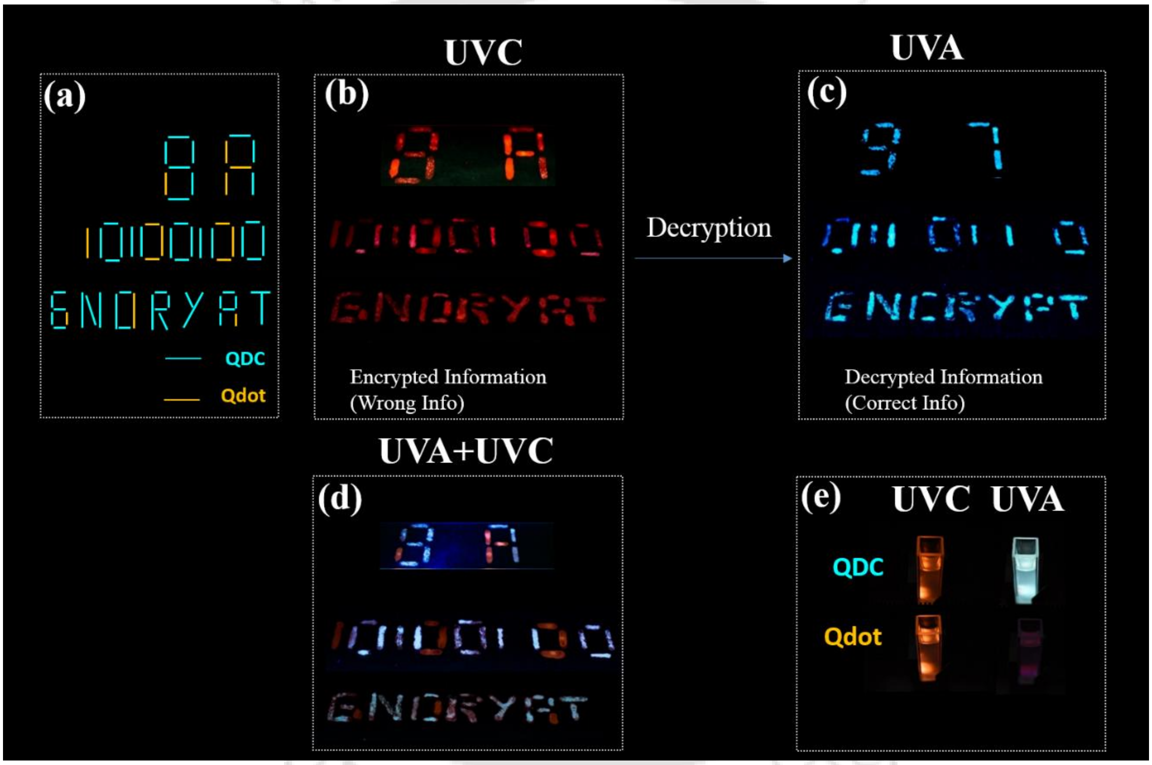

Figure 3.8. (a) Representation of cifertexts written with Qdot and QDC. Digital photographs of (b) encrypted information observed under UVC and (c) decrypted information observed under UVA. (d) Cifertexts observed under combined exposer of UVA and UVC. (e) Digital photographs of dispersions of Qdot and QDC under UVC and UVA.

Using the feature of white light emission from the QDC under 365 nm excitation, and orange emission at 255 nm excitation, an example of data encryption and decryption is shown in **Figure 3.8a-e**. The photoluminescence characteristics of Qdot and QDC in 255 nm and 365 nm are shown in **Figure B3.8, Appendix B**. An alpha numeric ciphertext "8A" was written with QDC and Qdot. Qdot (orange emission at 255 nm excitation) was used as an interfering agent. Under UVC irradiation, 8A - the encrypted information, could be observed, which appeared orange due to the photoluminescence properties of QDC as well as Qdot under 255 nm.

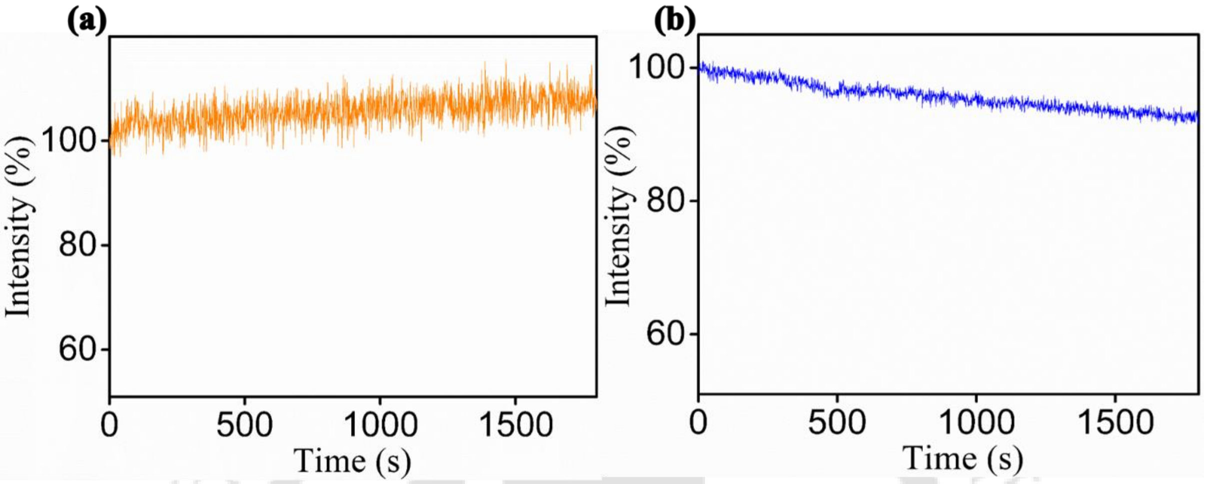

Figure 3.9. Photostability of dual-emitting QDC observed for (a) emission maximum 595 nm at λex=255 nm (UVC) and that for (b) emission maximum 480 nm at λex=365 nm (UVA).

However, when UVA source was turned ON, white colored number "97", which was the decrypted information, could be easily recognized by the naked eye. In the same manner, encryption of binary numbers "0110110" in "10100100" and "ENCRYPT" in "6N0RYAT" are shown in **Figure 3.8b, c**. The ciphertexts observed under combined effects of UVA and UVC are shown in **Figure 3.8d**. Here it can be observed that the parts of the texts written with Qdot appeared orange and the parts written with QDC appeared white. This feature can be used for dual encryption of secured information or printing QR codes with Qdot as the interfering agent. **Figure 3.8e** shows the digital photographs of Qdot and QDC dispersion under UVC and UVA. Additionally, photostability of dual emitting QDC was studied where percentage variation of luminescence intensity for emission peak at 595 nm and 480 nm was observed for a time duration of 1800 s. Nearly 90% of the luminescence intensity was retained for 480 nm emission under continuous excitation with 365 nm (UVA) light, whereas, no significant decay was observed for 595 nm emission under 255 nm (UVC) excitation (**Figure 3.9**). These observations suggest that the so prepared QDC from Mn^{2+} doped ZnS Qdot can be used as a promising anti-counterfeiting ink for data encryption.

3.9 Conclusions

We have demonstrated MSM ultraviolet photodetector based on Mn^{2+} doped ZnS Qdot exhibiting maximum responsivity under UVC radiations with responsivity 0.3±0.02 $A.W^{-1}$ and detectivity 1.7±0.2 10^{11} Jones. Interestingly, photodetectors with similar MSM structure, where surface complexed Mn^{2+} doped ZnS Qdots (QDC) was used as an active material, exhibited shift in the detection band and showed maximun responsivity in UVA region with responsivity 0.2±0.02 $A.W^{-1}$ and detectivity of 1.2 ±0.2 10^{11} Jones. Moreover, the devices could also be operated in self-biased mode due to the fast separation of excitons driven by the built-in electric field. Detector were then incorporated together in a portable device that demonstrated selective detections of UVA and UVC. The strategy of ligand specific surface complexation reaction in order to influence absorption and exciton dynamics in Qdot bears great potential to facilitate selective spectral detection from a single moiety, in a broader stretch of device interfaces and thus could provide new digital vision to optoelectronic industries. In addition, the white light emitting feature of the detector has been effectively utilized for data encryption and decryption.

3.10 References

1. Li, Y.; Shi, Z.; Liang, W.; Wang, L.; Li, S.; Zhang, F.; Ma, Z.; Wang, Y.; Tian, Y.; Wu, D.; Li, X.; Zhang, Y.; Shan, C.; Fang, X. Highly stable and spectrum-selective ultraviolet photodetectors based on lead-free copper-based perovskites. *Materials Horizons.* **2020**, 7, 530-540.

2. Zhang, Q.; Jie, J.; Diao, S.; Shao, Z.; Zhang, Q.; Wang, L.; Deng, W.; Hu, W.; Xia, H.; Yuan, X.; Lee, S. T. Solution-processed graphene quantum dot deep-UV photodetectors. *ACS Nano.* **2015**, 9, 1561-70.

3. An, Q.; Meng, X.; Xiong, K.; Qiu, Y. Self-powered ZnS Nanotubes/Ag Nanowires MSM UV Photodetector with High On/Off Ratio and Fast Response Speed. *Sci Rep.* **2017**, 7, 4885.

4. Zuo, J.; Tu, L.; Li, Q.; Feng, Y.; Que, I.; Zhang, Y.; Liu, X.; Xue, B.; Cruz, L. J.; Chang, Y.; Zhang, H.; Kong, X. Near Infrared Light Sensitive Ultraviolet-Blue Nanophotoswitch for Imaging-Guided "Off-On" Therapy. *ACS Nano.* **2018**, 12, 3217-3225.

5. Wu, H.; Sun, Y.; Lin, D.; Zhang, R.; Zhang, C.; Pan, W. GaN Nanofibers based on Electrospinning: Facile Synthesis, Controlled Assembly, Precise Doping, and Application as High Performance UV Photodetector. *Advanced Materials.* **2009**, 21, 227-231.

6. Guo, D.; Su, Y.; Shi, H.; Li, P.; Zhao, N.; Ye, J.; Wang, S.; Liu, A.; Chen, Z.; Li, C.; Tang, W. Self-Powered Ultraviolet Photodetector with Superhigh Photoresponsivity (3.05 A/W) Based on the GaN/Sn:Ga2O3 pn Junction. *ACS Nano.* **2018**, 12, 12827-12835.

7. Wang, F.; Gao, T.; Zhang, Q.; Hu, Z.-Y.; Jin, B.; Li, L.; Zhou, X.; Li, H.; Van Tendeloo, G.; Zhai, T. Liquid-Alloy-Assisted Growth of 2D Ternary Ga2In4S9 toward High-Performance UV Photodetection. *Advanced Materials.* **2019**, 31, 1806306.

8. Kim, S. J.; Han, J. W.; Kim, B.; Meyyappan, M. Single Walled Carbon Nanotube Based Air Pocket Encapsulated Ultraviolet Sensor. *ACS Sens.* **2017**, 2, 1679-1683.

9. Gao, Y.; Xu, J.; Shi, S.; Dong, H.; Cheng, Y.; Wei, C.; Zhang, X.; Yin, S.; Li, L. TiO2 Nanorod Arrays Based Self-Powered UV Photodetector: Heterojunction with NiO Nanoflakes and Enhanced UV Photoresponse. *ACS Appl Mater Interfaces.* **2018**, 10, 11269-11279.

10. Li, G.; Suja, M.; Chen, M.; Bekyarova, E.; Haddon, R. C.; Liu, J.; Itkis, M. E. Visible-Blind UV Photodetector Based on Single-Walled Carbon Nanotube Thin Film/ZnO Vertical Heterostructures. *ACS Appl Mater Interfaces.* **2017**, 9, 37094-37104.

11. Kim, Y.; Kim, S. J.; Cho, S. P.; Hong, B. H.; Jang, D. J. High-performance ultraviolet photodetectors based on solution-grown ZnS nanobelts sandwiched between graphene layers. *Sci Rep.* **2015**, 5, 12345.

12. Zheng, W.; Lin, R.; Ran, J.; Zhang, Z.; Ji, X.; Huang, F. Vacuum-Ultraviolet Photovoltaic Detector. *ACS Nano.* **2018**, 12, 425-431.

13. Kim, J.; Kwon, S.-M.; Kang, Y. K.; Kim, Y.-H.; Lee, M.-J.; Han, K.; Facchetti, A.; Kim, M.-G.; Park, S. K. A skin-like two-dimensionally pixelized full-color quantum dot photodetector. *Science Advances.* **2019**, 5, eaax8801.

14. Beard, M. C. Multiple Exciton Generation in Semiconductor Quantum Dots. *J Phys Chem Lett.* **2011**, 2, 1282-8.

15. Lee, J. H.; Lee, W. W.; Yang, D. W.; Chang, W. J.; Kwon, S. S.; Park, W. I. Anomalous Photovoltaic Response of Graphene-on-GaN Schottky Photodiodes. *ACS Appl Mater Interfaces.* **2018**, 10, 14170-14174.

16. Chen, W.; Castro, J.; Ahn, S.; Li, X.; Vazquez-Mena, O. Improved Charge Extraction Beyond Diffusion Length by Layer-by-Layer Multistacking Intercalation of Graphene Layers inside Quantum Dots Films. *Adv Mater.* **2019**, 31, e1807894.

17. Gong, M.; Liu, Q.; Cook, B.; Kattel, B.; Wang, T.; Chan, W. L.; Ewing, D.; Casper, M.; Stramel, A.; Wu, J. Z. All-Printable ZnO Quantum Dots/Graphene van der Waals Heterostructures for Ultrasensitive Detection of Ultraviolet Light. *ACS Nano.* **2017**, 11, 4114-4123.

18. Zhu, Y.; Liu, K.; Ai, Q.; Hou, Q.; Chen, X.; Zhang, Z.; Xie, X.; Li, B.; Shen, D. A high performance self-powered ultraviolet photodetector based on a p-GaN/n-ZnMgO heterojunction. *Journal of Materials Chemistry C.* **2020**, 8, 2719-2724.

19. Chen, X.; Liu, K.; Zhang, Z.; Wang, C.; Li, B.; Zhao, H.; Zhao, D.; Shen, D. Self-Powered Solar-Blind Photodetector with Fast Response Based on Au/β-Ga2O3 Nanowires Array Film Schottky Junction. *ACS Applied Materials & Interfaces.* **2016**, 8, 4185-4191.

20. Chen, H.; Yu, P.; Zhang, Z.; Teng, F.; Zheng, L.; Hu, K.; Fang, X. Ultrasensitive Self-Powered Solar-Blind Deep-Ultraviolet Photodetector Based on All-Solid-State Polyaniline/MgZnO Bilayer. *Small.* **2016**, 12, 5809-5816.

21. Arora, K.; Goel, N.; Kumar, M.; Kumar, M. Ultrahigh Performance of Self-Powered β-Ga2O3 Thin Film Solar-Blind Photodetector Grown on Cost-Effective Si Substrate Using High-Temperature Seed Layer. *ACS Photonics*. **2018**, 5, 2391-2401.

22. Liu, R.; Wang, F.; Liu, L.; He, X.; Chen, J.; Li, Y.; Zhai, T. Band Alignment Engineering in Two-Dimensional Transition Metal Dichalcogenide-Based Heterostructures for Photodetectors. *Small Structures*. **2021**, 2, 2000136.

23. Santra, P. K.; Kamat, P. V. Mn-doped quantum dot sensitized solar cells: a strategy to boost efficiency over 5%. *J Am Chem Soc*. **2012**, 134, 2508-11.

24. Hsu, C. L.; Chang, S. J. Doped ZnO 1D nanostructures: synthesis, properties, and photodetector application. *Small*. **2014**, 10, 4562-85.

25. Clark, P. C. J.; Neo, D. C. J.; Ahumada-Lazo, R.; Williamson, A. I.; Pis, I.; Nappini, S.; Watt, A. A. R.; Flavell, W. R. Influence of Multistep Surface Passivation on the Performance of PbS Colloidal Quantum Dot Solar Cells. *Langmuir*. **2018**, 34, 8887-8897.

26. Asaduzzaman, A.; Runge, K.; Deymier, P.; Muralidharan, K. Effect of Ligand Adsorption on the Electronic Properties of the PbS(100) Surface. *Langmuir*. **2020**, 36, 13312-13319.

27. Teh, Z. L.; Hu, L.; Zhang, Z.; Gentle, A. R.; Chen, Z.; Gao, Y.; Yuan, L.; Hu, Y.; Wu, T.; Patterson, R. J.; Huang, S. Enhanced Power Conversion Efficiency via Hybrid Ligand Exchange Treatment of p-Type PbS Quantum Dots. *ACS Applied Materials & Interfaces*. **2020**, 12, 22751-22759.

28. Garcia-Cortes, M.; Sotelo González, E.; Fernández-Argüelles, M. T.; Encinar, J. R.; Costa-Fernández, J. M.; Sanz-Medel, A. Capping of Mn-Doped ZnS Quantum Dots with DHLA for Their Stabilization in Aqueous Media: Determination of the Nanoparticle Number Concentration and Surface Ligand Density. *Langmuir*. **2017**, 33, 6333-6341.

29. Ritchhart, A.; Monahan, M.; Mars, J.; Toney, M. F.; De Yoreo, J. J.; Cossairt, B. M. Covalently Linked, Two-Dimensional Quantum Dot Assemblies. *Langmuir*. **2020**, 36, 9944-9951.

30. Sun, R.; Zhou, D.; Wang, Y.; Xu, W.; Ding, N.; Zi, L.; Zhuang, X.; Bai, X.; Song, H. Highly efficient ligand-modified manganese ion doped CsPbCl3 perovskite quantum dots for photon energy conversion in silicon solar cells. *Nanoscale*. **2020**, 12, 18621-18628.

31. Shen, T.; Li, B.; Zheng, K.; Pullerits, T.; Cao, G.; Tian, J. Surface Engineering of Quantum Dots for Remarkably High Detectivity Photodetectors. *The Journal of Physical Chemistry Letters*. **2018**, 9, 3285-3294.

32. Manna, M.; Roy, S.; Bhandari, S.; Chattopadhyay, A. A Ratiometric and Visual Sensing of Phosphate by White Light Emitting Quantum Dot Complex. *Langmuir*. **2021**, 37, 5506-5512.

33. Pramanik, S.; Roy, S.; Mondal, A.; Bhandari, S. A two-target responsive reversible ratiometric pH nanoprobe: a white light emitting quantum dot complex. *Chemical Communications*. **2019**, 55, 4331-4334.

34. Bhandari, S.; Roy, S.; Pramanik, S.; Chattopadhyay, A. Chemical Reactions Involving the Surface of Metal Chalcogenide Quantum Dots. *Langmuir*. **2019**, 35, 14399-14413.

35. Gogoi, K.; Pramanik, S.; Chattopadhyay, A. Charge Transport Characteristics of Surface-Complexed Quantum Dot in a Thin Film Transistor. *Advanced Materials Interfaces*. **2020**, 7, 1901665.

36. Roy, S.; Bhandari, S.; Manna, M.; De, S.; Chattopadhyay, A. The nature of binding of quinolate complex on the surface of ZnS quantum dots. *Physical Chemistry Chemical Physics*. **2019**, 21, 589-596.

37. Roy, S.; Manna, M.; Chattopadhyay, A. Complex Transfer Reaction from ZnO to ZnS Quantum Dots Driven by Surface Anions. *The Journal of Physical Chemistry C*. **2018**, 122, 9939-9946.

38. Yin, X.; Zhang, C.; Guo, Y.; Yang, Y.; Xing, Y.; Que, W. PbS QD-based photodetectors: future-oriented near-infrared detection technology. *Journal of Materials Chemistry C*. **2021**, 9, 417-438.

39. Begum, R.; Chattopadhyay, A. Redox-Tuned Three-Color Emission in Double (Mn and Cu) Doped Zinc Sulfide Quantum Dots. *Journal of Physical Chemistry Letters*. **2014**, 5, 126-130.

40. Bradshaw, L. R.; Hauser, A.; McLaurin, E. J.; Gamelin, D. R. Luminescence Saturation via Mn2+–Exciton Cross Relaxation in Colloidal Doped Semiconductor Nanocrystals. *The Journal of Physical Chemistry C*. **2012**, 116, 9300-9310.

41. Chen, H.-Y.; Chen, T.-Y.; Berdugo, E.; Park, Y.; Lovering, K.; Son, D. H. Hot Electrons from Consecutive Exciton–Mn Energy Transfer in Mn-Doped Semiconductor Nanocrystals. *The Journal of Physical Chemistry C*. **2011**, 115, 11407-11412.

42. White, M. A.; Weaver, A. L.; Beaulac, R.; Gamelin, D. R. Electrochemically Controlled Auger Quenching of Mn2+ Photoluminescence in Doped Semiconductor Nanocrystals. *ACS Nano*. **2011**, 5, 4158-4168.

43. Qiao, T.; Parobek, D.; Son, D. H. Photons and charges from colloidal doped semiconductor quantum dots. *Journal of Materials Chemistry C*. **2019**, 7, 14788-14797.

44. Pramanik, S.; Bhandari, S.; Roy, S.; Chattopadhyay, A. Synchronous Tricolor Emission-Based White Light from Quantum Dot Complex. *The Journal of Physical Chemistry Letters*. **2015**, 6, 1270-1274.

45. Hopkins, T. A.; Meerholz, K.; Shaheen, S.; Anderson, M. L.; Schmidt, A.; Kippelen, B.; Padias, A. B.; Hall, H. K.; Peyghambarian, N.; Armstrong, N. R. Substituted Aluminum and Zinc Quinolates with Blue-Shifted Absorbance/Luminescence Bands: Synthesis and Spectroscopic, Photoluminescence, and Electroluminescence Characterization. *Chemistry of Materials*. **1996**, 8, 344-351.

46. Pan, H.-C.; Liang, F.-P.; Mao, C.-J.; Zhu, J.-J.; Chen, H.-Y. Highly Luminescent Zinc(II)−Bis(8-hydroxyquinoline) Complex Nanorods: Sonochemical Synthesis, Characterizations, and Protein Sensing. *The Journal of Physical Chemistry B*. **2007**, 111, 5767-5772.

47. Bhandari, S.; Pramanik, S.; Khandelia, R.; Chattopadhyay, A. Gold Nanocluster and Quantum Dot Complex in Protein for Biofriendly White-Light-Emitting Material. *ACS Applied Materials & Interfaces*. **2016**, 8, 1600-1605.

48. Li, Y.; Shi, Z. F.; Liang, W. Q.; Wang, L. T.; Li, S.; Zhang, F.; Ma, Z. Z.; Wang, Y.; Tian, Y. Z.; Wu, D.; Li, X. J.; Zhang, Y. T.; Shan, C. X.; Fang, X. S. Highly stable and spectrum-selective ultraviolet photodetectors based on lead-free copper-based perovskites. *Materials Horizons*. **2020**, 7, 530-540.

49. Dong, Y.; Parobek, D.; Rossi, D.; Son, D. H. Photoemission of Energetic Hot Electrons Produced via Up-Conversion in Doped Quantum Dots. *Nano Letters*. **2016**, 16, 7270-7275.

50. Barrows, C. J.; Rinehart, J. D.; Nagaoka, H.; deQuilettes, D. W.; Salvador, M.; Chen, J. I. L.; Ginger, D. S.; Gamelin, D. R. Electrical Detection of Quantum Dot Hot Electrons Generated via a Mn2+-Enhanced Auger Process. *The Journal of Physical Chemistry Letters*. **2017**, 8, 126-130.

51. Soci, C.; Zhang, A.; Xiang, B.; Dayeh, S. A.; Aplin, D. P. R.; Park, J.; Bao, X. Y.; Lo, Y. H.; Wang, D. ZnO Nanowire UV Photodetectors with High Internal Gain. *Nano Letters*. **2007**, 7, 1003-1009.

52. Alenezi, M. R.; Alshammari, A. S.; Alzanki, T. H.; Jarowski, P.; Henley, S. J.; Silva, S. R. P. ZnO Nanodisk Based UV Detectors with Printed Electrodes. *Langmuir*. **2014**, 30, 3913-3921.

Appendix B

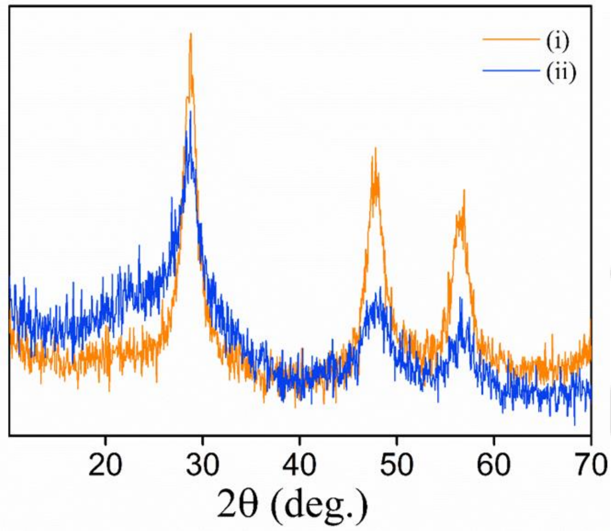

Figure B3.1. Powder XRD patterns of (i) ligand free Qdot and (ii) QDC.

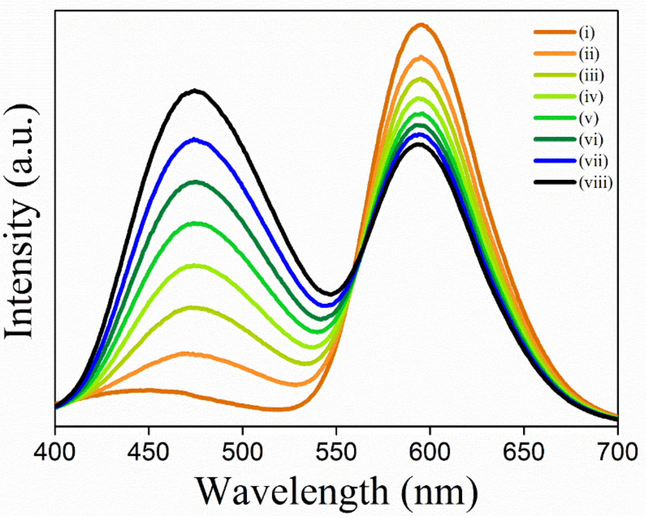

Figure B3.2. Photoluminescence spectra on addition of (i) 00, (ii) 0.99 µM, (iii) 1.99 µM, (iv) 2.99 µM, (v) 3.98 µM, (vi) 4.97 µM and (vii) 5.96 µM HQS ligand to Mn^{2+} doped ZnS Qdot (λex= 330 nm).

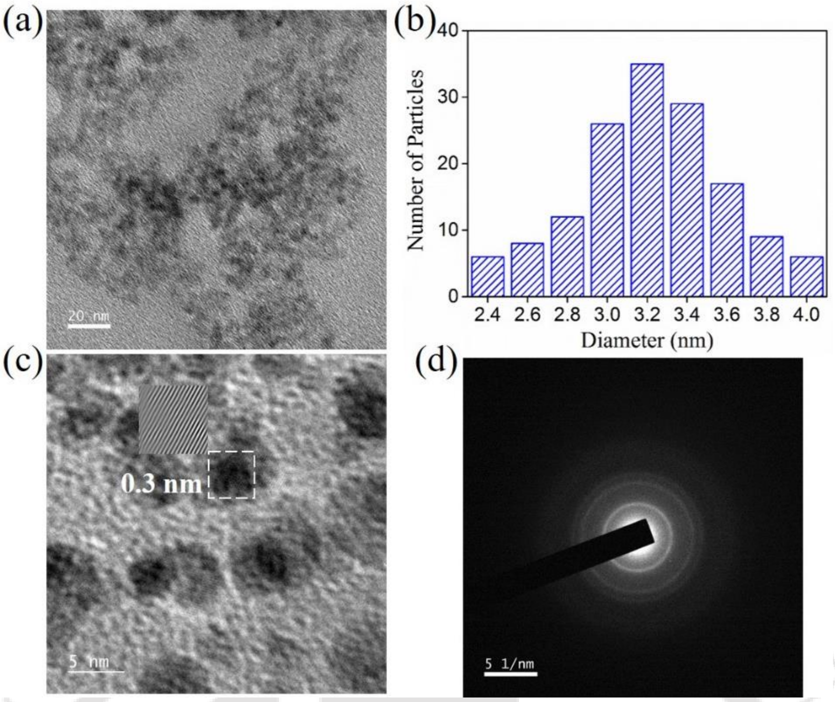

Figure B3.3. (a) Transmission Electron Microscopy image (scale bar - 20 nm), (b) corresponding particle size distribution, (c) high resolution transmission electron microscope image (scale bar - 5 nm) (inset: marked are IFFT image) with lattice fringe spacing 0.3 nm and (d) SAED pattern of as-synthesized Qdots.

Photoresponse of ZnS Qdot

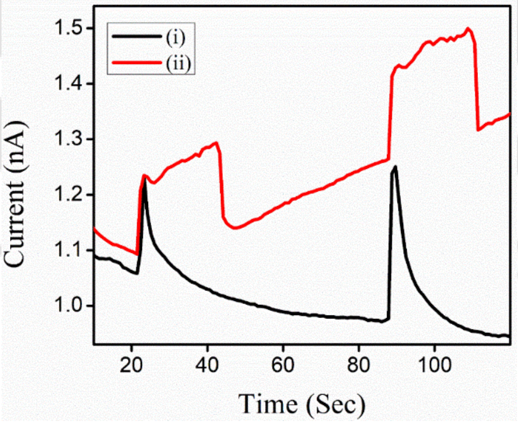

Figure B3.4. Photoresponse of only ZnS Qdot PD upon (i) 255 nm and (ii) 365nm irradiation.

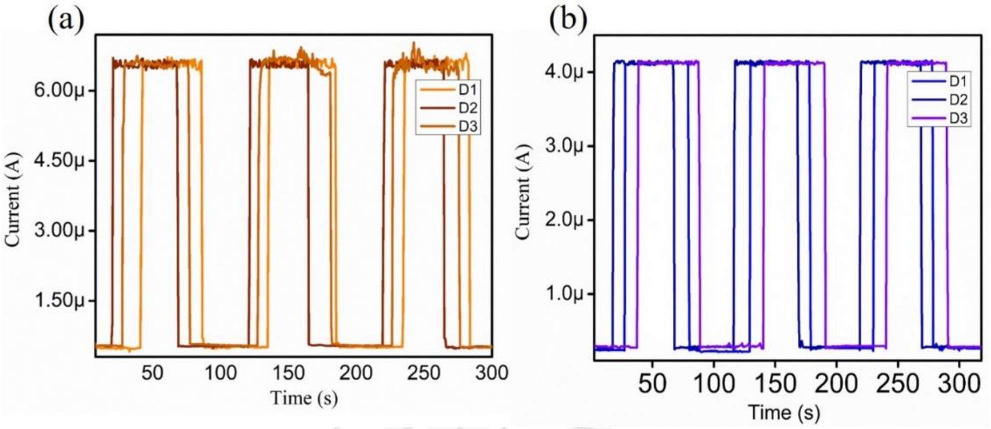

Figure B3.5. Photoresponse of three (a) Mn^{2+} doped ZnS Qdot photodetectors and (b) Mn^{2+} doped ZnS Qdot complex photodetectors.

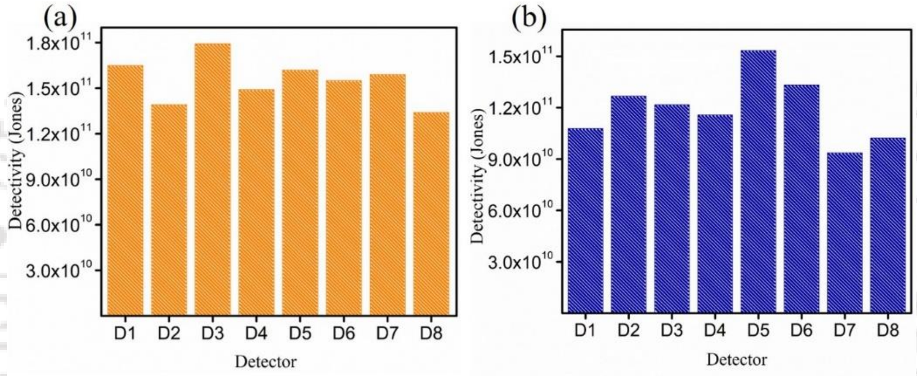

Figure B3.6. Responsivity of eight (a) Mn^{2+} doped ZnS Qdot photodetectors and (b) Mn^{2+} doped ZnS Qdot complex photodetectors. The numbers in D represent specific detectors used for the study.

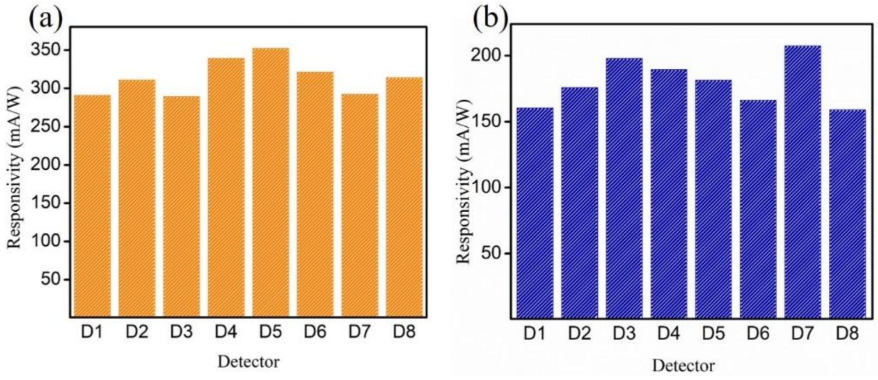

Figure B3.7. Detectivity of eight (a) Mn^{2+} doped ZnS Qdot photodetectors and (b) Mn^{2+} doped ZnS Qdot complex photodetectors. The numbers in D represent specific detectors used for the study.

Table B1. Performance parameters of Qdot-PD and QDC-PD.

	Photocurrent		**Responsivity (mA/W)**		**Detectivity (Jones)**		**Dark Current**	**t_r/t_f** μs
	UVA	**UVC**	**UVA**	**UVC**	**UVA**	**UVC**		
Qdot (0 V)		185 nA		9.8		1.2 × 10^{11}	6x 10^{-10}A	65/130
QDC (0V)	90 nA		4.8		6.6 × 10^{10}		5x10^{-10}A	65/130
Qdot (3V)	2.05 μA	6.59 μA	87±23	0.3±0.02 × 10^{3}	4±1 × 10^{10}	1.7±0.2 × 10^{11}	4 x 10^{-7} A	65/130
QDC (3V)	4.21 μA	1.82 μA	0.2±0.02 × 10^{3}	81±10	1.2±0.2×10^{11}	5±1 ×10^{10}	2.1 x 10^{-7} A	65/130

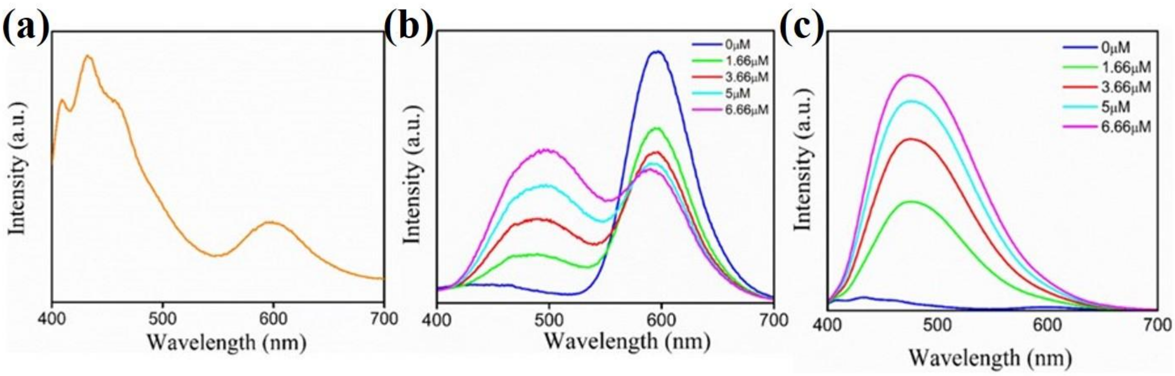

Figure B3.8. Photoluminescence spectrum of Mn^{2+} doped ZnS Qdot at (A)λ_{ex}=365 nm **(B)** Quenching of photoluminescence (λ_{em}=595 nm) of Qdot on successive additions of HQS ligand at λ_{ex}=255 nm **(C)** Photoluminescence of QDC on increasing concentration of HQS ligand in Qdot dispersion at λ_{ex}=365 nm.

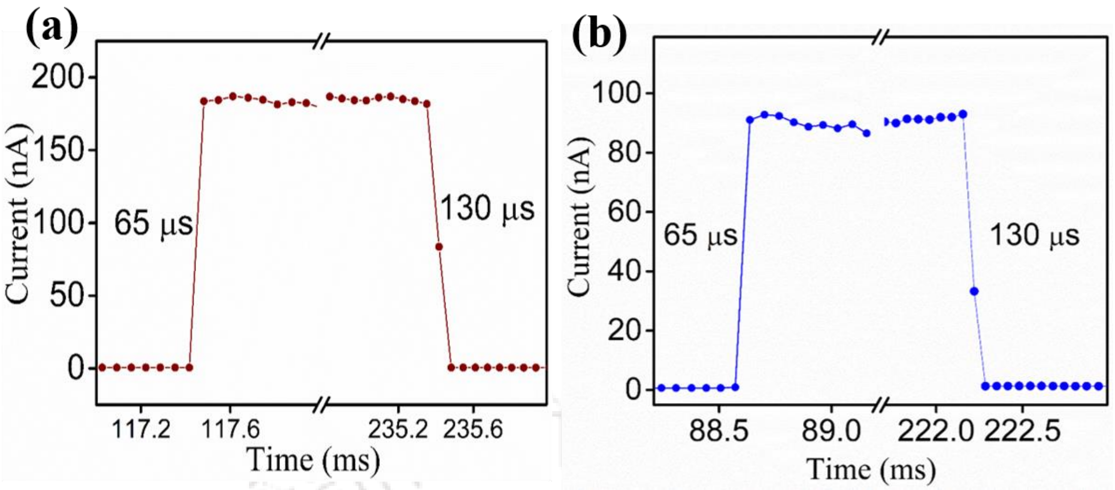

Figure B3.9. Transient characteristics under Zero bias (a) Qdot-PD and (b) QDC-PD.

Table B2. Comparison table on device performance.

S.I	**Materials**	**Responsivity (A/W)**	**Detectivity (Jones)**	**Response time**	**Bias voltage**	**Refs**
1.	ZnS Qdot	0.1×10^{-3}		0.35s/0.07s	40 V	1
2.	ZnS Qdot	0.31		0.05	1.0 V	2
3	$CuInS_2$/ZnS Core–Shell QD	0.86	3.76×10^{11}	$<5 \times 10^{-3}$ s	-40V	3
4	ZnO	6.27×10^{-3}		8.79s/18.13s	1V	4
5	MnO QD	25×10^{-3}	1.49×10^{11}	0.29s	1 V	5
6.	Mn^{2+}-ZnS QD	0.3±0.02	1.7×10^{11}	<65 μs/ 130 μs	3V	This work
7.	Mn^{2+}-ZnS-HQS QDC	0.2±0.02	1.2×10^{11}	<65 μs / 130 μs	3V	This work
8.	α/β-Ga_2O_3	0.26×10^{-3}	2.8×10^{9}	0.54s	0V	6
9.	Ga_2O_3	5.8×10^{-3}	7.6×10^{10}	0.108×10^{-3} s /0.380×10^{-3} s	0V	7
10.	α-Ga_2O_3 Nanorod Array–Cu_2O	0.42×10^{-3}(254nm), 0.57×10^{-3}(365 nm)		10.3s	0V	8
11.	graphene/ZnS QDs/4HSiC	0.29×10^{-3}		0.028×10^{-3} s /0.75×10^{-3} s	0	9
12.	ZnO/ZnS Core shell	0.056		0.04 s	0V	10
13.	ZnO	1.42×10^{-3}	1.07×10^{11}	1.25s/ 1.84s	0	11
14.	Mn^{2+}-ZnS QD	9.8×10^{-3}	1.3×10^{11}	<65μs/130 μs	0V	This work
15.	Mn^{2+}-ZnS-HQS QDC	4.7×10^{-3}	5.6×10^{10}	<65 μs / 130 μs	0V	This work

References

1. Xia, Y.; Zhai, G.; Zheng, Z.; Lian, L.; Liu, H.; Zhang, D.; Gao, J.; Zhai, T.; Zhang, J. Solution-processed solar-blind deep ultraviolet photodetectors based on strongly quantum confined ZnS quantum dots. *Journal of Materials Chemistry C*. 2018, 6, 11266-11271.

2. Premkumar, S.; Nataraj, D.; Bharathi, G.; Ramya, S.; Thangadurai, T. D. Highly Responsive Ultraviolet Sensor Based on ZnS Quantum Dot Solid with Enhanced Photocurrent. *Scientific Reports.* 2019, 9, 18704.

3. Liu, Y.; Zhao, C.; Li, J.; Zhao, S.; Xu, X.; Fu, H. Y.; Yu, C.; Kang, F.; Wei, G. Highly Sensitive CuInS2/ZnS Core–Shell Quantum Dot Photodetectors. *ACS Applied Electronic Materials.* 2021, 3, 1236-1243.

4. Veerla, R. S.; Sahatiya, P.; Badhulika, S. Fabrication of a flexible UV photodetector and disposable photoresponsive uric acid sensor by direct writing of ZnO pencil on paper. *Journal of Materials Chemistry C.* 2017, 5, 10231-10240.

5. Mitra, S.; Pak, Y.; Alaal, N.; Hedhili, M. N.; Almalawi, D. R.; Alwadai, N.; Loganathan, K.; Kumarasan, Y.; Lim, N.; Jung, G. Y.; Roqan, I. S. Novel P-Type Wide Bandgap Manganese Oxide Quantum Dots Operating at Deep UV Range for Optoelectronic Devices. *Advanced Optical Materials.* 2019, 7, 1900801.

6. Wu, C.; He, C.; Guo, D.; Zhang, F.; Li, P.; Wang, S.; Liu, A.; Wu, F.; Tang, W. Vertical α/β-Ga2O3 phase junction nanorods array with graphene-silver nanowire hybrid conductive electrode for high-performance self-powered solar-blind photodetectors. *Materials Today Physics.* 2020, 12, 100193.

7. Kan, H.; Zheng, W.; Fu, C.; Lin, R.; Luo, J.; Huang, F. Ultrawide Band Gap Oxide Nanodots (Eg > 4.8 eV) for a High-Performance Deep Ultraviolet Photovoltaic Detector. *ACS Applied Materials & Interfaces.* 2020, 12, 6030-6036.

8. He, C.; Guo, D.; Chen, K.; Wang, S.; Shen, J.; Zhao, N.; Liu, A.; Zheng, Y.; Li, P.; Wu, Z.; Li, C.; Wu, F.; Tang, W. α-Ga2O3 Nanorod Array–Cu2O Microsphere p–n Junctions for Self-Powered Spectrum-Distinguishable Photodetectors. *ACS Applied Nano Materials.* 2019, 2, 4095-4103.

9. Kan, H.; Zheng, W.; Lin, R.; Li, M.; Fu, C.; Sun, H.; Dong, M.; Xu, C.; Luo, J.; Fu, Y.; Huang, F. Ultrafast Photovoltaic-Type Deep Ultraviolet Photodetectors Using Hybrid Zero-/Two-Dimensional Heterojunctions. *ACS Applied Materials & Interfaces.* 2019, 11, 8412-8418.

10. Lin, H.; Wei, L.; Wu, C.; Chen, Y.; Yan, S.; Mei, L.; Jiao, J. High-Performance Self-powered Photodetectors Based on ZnO/ZnS Core-Shell Nanorod Arrays. *Nanoscale Research Letters.* 2016, 11, 420.

11. Zhang, Y.; Peng, M.; Liu, Y.; Zhang, T.; Zhu, Q.; Lei, H.; Liu, S.; Tao, Y.; Li, L.; Wen, Z.; Sun, X. Flexible Self-Powered Real-Time Ultraviolet Photodetector by Coupling Triboelectric and Photoelectric Effects. *ACS Applied Materials & Interfaces.* 2020, 12, 19384-19392.

Chapter 4

Gold Nanoparticle Network based Tactile Sensor for Human Activity Recognition

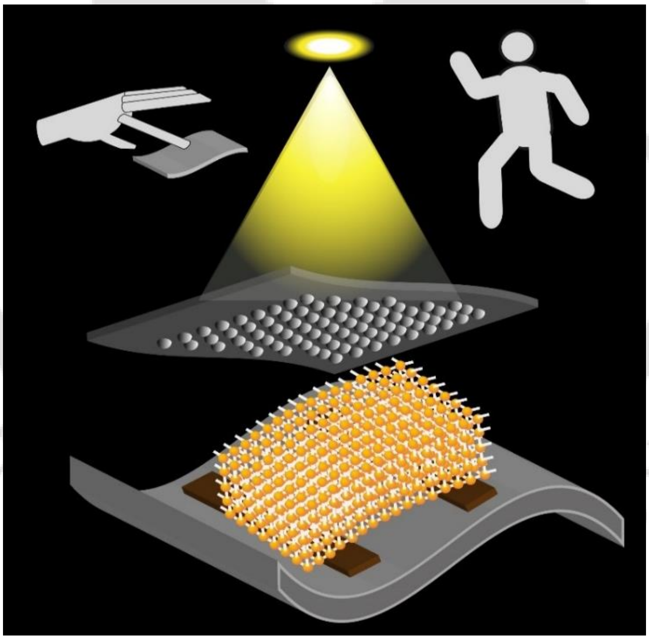

Chapter 4

Gold Nanoparticle Network based Tactile Sensor for Human Activity Recognition

Abstract

Strain-based complex functionalities in response to external physical stimuli is significant for the development of intelligent robotic systems. Herein, we have developed an assembly of gold nanoparticles (Au NP-PA network) through ligand interaction with short linker molecule 2-picolylamine (PA). With sub-nanometer spacing between the nanoparticles (NP), the network promoted strain sensitive carrier tunnelling between them. A multi-stimuli responsive tactile sensor based on these NP networks and a lithographically patterned PDMS microstructures were developed that effectively transduced mechanical strain to electrical responses, and could identify variable weights, detect finger touch patterns and was ultra-sensitive to vibrational movements. Different physical activities such as jogging, leg movements, and standing from sitting postures were identified using the system. A significantly high gauge factor of 243±10 associated with the Au NP-PA network was recorded. In addition, it exhibited strain-dependent plasmonic-photodetection with a responsivity of 309 mA/W at a tensile strain of 3.7%. The multi-stimuli responsive Au NP-PA network demonstrated here opens up new perspectives to develop artificially intelligent multifunctional systems.

4.1 Introduction

With the massive development of artificially intelligent technology, multifunctional flexible sensors are of utmost interest that functionally meet the demands of robotic interfaces, smart medical prognosis and flexible electronics.[1-3] Human sensory system inspired tactile sensors with nanostructured materials such as metal oxides[4], polymers and polymer composites[5] are reported to emulate human tactile sensory and reflex behaviours driving the need of wearable gadgets, primary healthcare platforms and electronic skin for robotic interfaces. In this regard, impressive tactile sensors are being developed that can perceive external mechanical stimuli such as, stress, strain, torsion, spatio-temporal touch patterns, heartbeat and breathing sequence and translate them into recognizable electrical signals or digital images. These sensors operate on the concepts of piezo-resistive,[6, 7] piezo-capacitive[3, 8] and tribo-electric nano generators (TENG),[9-11] that mimic manual palpation as well as respond to neurovascular signals.

In spite of progressive growth in strain and static pressure sensors, it is challenging to develop dynamic pressure sensors or vibration sensors due to their inherent latency in the sensor readout. Piezoelectric materials such as multiwalled carbon nanotube,[7] reduced graphene oxide/PDMS composite[12] and several other nanocrystal/PDMS composites[13, 14] have been designed as vibration sensors. Moreover, TENG sensors have been effective and robust that can harvest mechanical vibrations and turn them into electrical signals due to the contact and separation between two materials.[15] Crosslinked gold nanoparticle (Au NPs) have emerged as a new breed of piezoelectric transducers the sensitivity of which towards mechanical strain could be controlled with organic linkers such as marcaptopropanoic acids, 1,9-nonanedithiol,[16] tetra(ethylene glycol) dithiol[17] and also introduce chemiresistive sensing abilities depending on the type and polarity of the linker molecule.[18] However, strategically controlled higher order assembly of Au NP via ligand interactions has not been adequately investigated and hence leaves an ample room to capitalise on/exploit their importance as mechanoreceptors.

Tactile sensors that can be driven by external stimuli such as light, in addition to cutaneous touch and mechanical strain simultaneously, would be novel for enhancing the multifunctional attributes. Developing a sensor that can detect diverse inputs accurately and concurrently still remains a challenge. In this context, assembly of metal nanostructures has attractive properties such as large surface area and high electrical conductivity due to carrier tunnelling in percolating network of NP assembly.[17] Enhanced localized surface plasmon resonance (LSPR) in metal NP assembly,[19, 20] supports their wide scale potential for plasmonic devices and photocatalytic applications over broad spectral range spanning from ultraviolet to the infrared. Therefore, synergistic coupling of LSPR and piezoelectric effect can modulate internal electric field that can regulate internal charge migration for potential applications in multifunctional tactile sensors.

Herein, we have developed an assembly of Au NP through ligand interaction with short organic linker molecule 2-picolylamine (PA). The binding interaction between the linker and

Au NP is via donor–acceptor interaction between pyridine-N and vacant orbital of Au through σ donation and π-back donation of valance electron from the polarized Au. Hydrogen bonds between the free NH_2 group of PA attached to Au NP resulted in the formation of NP networks and sub-nanometer spacing between the units facilitated carrier tunnelling between them. A multi-stimuli responsive tactile sensor based on these NP network and a micro-patterned polydimethylsiloxane (PDMS) layer was demonstrated. The micro-patterned PDMS layer offered different compressive strains on the NP assembly that produced triboelectric responses due to contact electrification depending on the degree of external strain. The device response towards concave and convex bending, static pressure exerted by variable weights and finger touch patterns have been demonstrated. The fast responsivity of 20 ms produced vibrational transduction responses. A significantly high gauge factor of 243±10 was obtained, which implied its high sensitivity towards mechanical deformations. In addition, phtoresponsive characteristics of Au NP-PA assembly were recorded, which exhibited strain-dependent photoresponse characteristics. Responsivity of 309 mA/W and detectivity of $2.1\text{x}10^{10}$ were observed under a low mechanical strain of 3.7%. These piezo-phototronic responses of Au NP-PA assembly, in integration with its tactile responses is thus a novel approach to design and fabricate multifunctional flexible electronic devices.

4.2 Materials and Methods

Materials: Si/SiO_2 substrate, 184 silicone elastomer base and curing agent (Sylgard), Milli-Q (MQ) water, Au wire (Kurt J Lesker), hexamethyldisilazane (HMDS) (Himedia), S1813 G2 positive photoresist (Microposit), MF-319 Developer (Microposit), gold(III) chloride (Sigma), trisodium citrate (Sigma), 2-picolylamine (Mark) and (3- mercaptopropyle) trimethoxy silane (fluka).

Au NP Synthesis:

Au NP was synthesized following a well-established method.[21] 27.2 mg trisodium citrate was dissolved in 50 mL water (MQ grade) in a round bottom flask and heated at 110 °C under continuous stirring. After an hour of stirring 246 µL of 29 mM $HAuCl_4$ was added into the solution. The appearance of the mixture turned red after some time and the stirring was continued for another 30 min. Thereafter, the stirring was stopped and the red coloured dispersion was allowed to reach room temperature. Finally, the citrate stabilized Au NP dispersion was centrifuged at 15000 rpm for 15 min and re-dispersed into the same volume of MQ grade water for further use.

Au NP-PA network synthesis: 400 µL of 0.5 M PA solution was added into the 10 mL of Au NP dispersion and stirred for 1 h. After that the mixture was centrifuged at 15000 rpm for 15 min and re-dispersed in the same volume of water (MQ grade). The colour transition from red to violet indicated the formation of assembled Au NP structures and was ready for further experimental use.

Substrate cleaning: Glass substrates and Si/SiO_2 wafers were successively cleaned with acetone, isopropyl alcohol and MQ grade water in an ultrasonic bath chamber and was dried under N_2 gas flow.

Device fabrication: Sylgard 184 silicone elastomer base and curing agent were thoroughly mixed in 10:1 ratio and degassed for 0.5 h to remove air bubbles and the mixture was spin-coated at 500 rpm for 60 s on pre-cleaned glass substrates. The substrates were then heat treated at 70 °C for 2 h to harden the elastomer. 150 µm thick PDMS layer was finally peeled off from the glass substrate for further use (**Figure C4.1 a, Appendix C**).

Electrode deposition: The PDMS substrates were placed on a PET substrate and was ozone treated for 30 minutes to increase the hydrophilicity of the surface. Gold electrodes were deposited with the help of a shadow mask through thermal evaporation system. The deposition was carried out for 5 minutes at 6×10^{-6} mbar chamber pressure and the rate of deposition was maintained at 4-10 Å/s. The substrates were annealed at 60 °C to get better adhesion of the electrodes. A gap of 40 µm between the electrodes were obtained the pictures of which are shown in **Figure C4.1 b, Appendix C**.

Au NP - PA network film formation: 3-marcaptopropyle silane solution was cast over the Au electrode patterned PDMS substrate and was kept for 30 minutes. The solution was then removed and the substrate was thoroughly washed with MQ grade water. Then the dispersion of Au NP-PA network was cast over the electrodes and was vacuum dried. Au NP assembly dispersion was cast consecutively in a layer by layer fashion. FESEM images showed the coverage of the electrodes after 1st, and 6th layer depositions of the Au NP assembly (**Figure C4.2, C4.3, Appendix C**). For comparison, FESEM images of bare Au NP layer after 6th layer of deposition is shown in **Figure C4.4 Appendix C.**

Fabrication of micropatterned PDMS layer: The micropatterned top PDMS layer was fabricated by employing photolithography technique. First, HMDS primer was coated on pre-cleaned Si/SiO_2 substrate at 4000 rpm for 60 s and was heated at 175 ^oC for 15 min. Subsequently, a layer of microposit S1813 G2 positive photoresist was spin-coated at a spin speed of 3500 rpm for 1 min and the substrate was heated at 130 ^oC for 3 min. The desired pattern with a microdot structure of 2 μm was drawn using the Dilase 250. After UV exposer, the substrate was developed in the positive photoresist developer (Microposit MF-319 Developer). The area where the UV was exposed forms a microstuctured puddle/ well and the unexposed area remains as is. This patterned photoresist layer on Si/SiO_2 substrates were used as moulds to develop inverse of the pattern features i.e., microstructured crest/hill patterns on one side of the PDMS layer. PDMS elastomer was cast over the patterned Si/SiO_2 substrates and degassed for 15 min to remove air bubbles. The substrates were then spin-coated at 300 rpm for 60 s. After thermal curing, the substrate was dipped in isopropyl alcohol to lift-off the photoresist and thereby obtain the micropatterned truncated cone shaped patterns on the PDMS layer having a feature size of 3 µm-bottom diameter and 5 µm top diameter. To make the complete device, the Au NP – PA network deposited layer was used as the bottom layer and the micro-patterned PDMS layer was placed over it. Au electrodes of the base layer were extended to make further electrical measurements.

4.3 Instruments Used

1. Electrical Characterizations: All the electrical measurements were carried out in Keithley 2614B source meter.

2. Photolithgraphy: Micro-patterned structures on PDMS substrates were fabricated with the help of Mask writer (Dilase 250).

3. FESEM: FESEM images of micropatterned PDMS layer and the Au NP film morphology and cross-sectional view of the PDMS layer were taken using JEOL JSM-7610F FESEM system.

4. UV-Vis absorbance spectra: UV-Vis absorbance spectra were recorded in Jasco V-360 spectrophotometer.

5. Morphological Characterization: Transmission electron microscopy (TEM) imaging, high resolution transmission electron microscopy (HRTEM), selected area electron diffraction

(SAED), and energy dispersive X-ray spectroscopy (EDS) characterizations were carried out in JEOL JEM-2100F transmission electron microscope (TEM) system.

4.4 Materials Characterization and Device Architecture

A structured two-dimensional network of NPs mimics an atomic crystal arrangement, where the NPs are not randomly arranged, but has a certain spacing between the NP centres and a two-dimensional repeating unit. Such an arrangement of NPs can be considered as a superlattice, that has a better stability and produces more uniform electromagnetic field than a random aggregate. Such NP frameworks also foster piezoelectric characteristics, where there is a strong correlation between external mechanical stimuli and tunnelling of carrier between adjacent units. To achieve this, we have considered PA as the functional linker molecule. The linker molecule was chosen in such a way that, it should be short enough to promote carrier tunnelling between the particles and also allow the formation of plasmonic hotspots and enhance hot carrier population in the NP network. Taking these factors into account, we have designed Au NP network composed of 18 nm diameter sized unit NPs and PA ligand molecules. When Au NP was treated with PA, pyridine-N site of PA molecule was bonded to the surface of Au NP and the free NH_2 group of PA participated in inter-particle hydrogen bond formation with another PA attached on Au NP.[22] The spherical shaped Au NP having average diameter of 18 nm and a higher order assembly of Au NP was observed from the transmission electron microscopy (TEM) image and a polycrystalline nature was observed from the selected area electron diffraction (SAED) patterns (**Figure 4.1a, Figure C4.5, Appendix C**). The NP network led to an average inter-particle distance of 0.6 nm (**Figure C4.6, Appendix C**). For comparison, the TEM image of the bare Au NP is shown in **Figure C4.7, Appendix C.** FESEM images confirmed the higher order assembly of the NPs (**Figure 4.1b**). A schematic representation of the molecular interaction and the network formation is illustrated in **Figure 4.1c**. The formation of Au NP-PA network can also be underpinned from the absorbance peak at 665 nm (**Figure C4.8, Appendix C**) in addition to absorbance peak of bare Au NP at 524 nm.

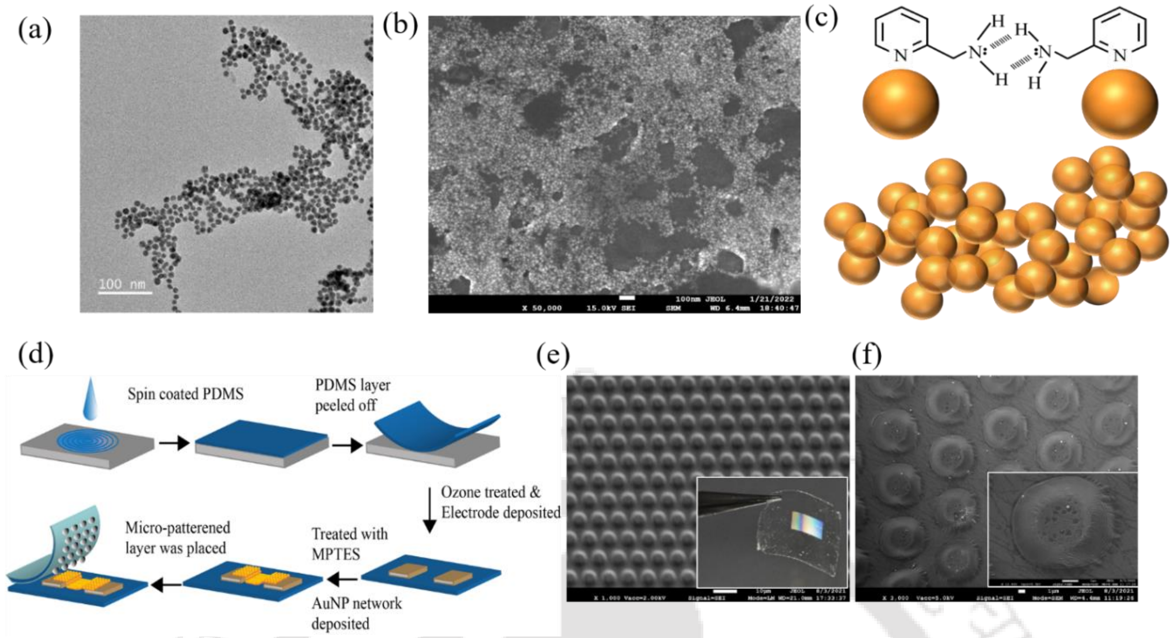

Figure 4.1. (a) Transmission electron microscopy image of Au NP network, (b) field emission scanning electron microscopy image and (c) schematic of Au NP-PA network formation. (d) Schematic representation of fabrication procedure of the tactile sensor. Topography of micropattened layer at a (e) scale bar of 10 µm (inset: digital photograph) (f) scale bar of 1 µm (inset: individual truncated conical shape of the pattern).

A substantial fraction of atoms near the Au NP surface, edge, or defect cites remains under-coordinated and negative charges gravitate toward the outermost shells, leaving positive charges in the interior shells of Au NPs. These shifting charges are referred to as valance electrons and are locally polarised by the entrapped core electrons. This under-coordination induced quantum trapping and valance charge polarization significantly assist the Au-N binding process. Upon interaction with the PA ligand, lone pair of electrons from pyridine-N are transferred to the vacant orbital of Au through σ donation as a result of which the effective negative surface potential of citrate stabilized Au NP might have been enhanced after the attachment of 2-PA molecules at the surface. This bond is not completely a pure N–Au donor–acceptor bond as π-back donation from occupied Au valence orbital to pyridine-N π^* orbital may also be present.[23]. As shown in the schematic in **Figure 4.1c** the hydrogen bonds between the free NH_2 group of the ligand bonded to the Au NP facilitates the formation of the network. Detailed synthesis procedure of Au NP-PA network formation is described in the experimental section. Compositional distribution of Au NP-PA assembly was confirmed by energy-dispersive X-ray spectroscopy (EDS) mapping, where the elemental distribution of nitrogen in 2-PA and gold can be observed (**Figure C4.9, C4.10, Appendix C**).

After achieving such a structure of Au NP network, we extended our research towards fabricating a tactile sensor from them. The tactile sensor was fabricated on a flexible polydimethylsiloxane (PDMS) substrate, where Au NP-PA network was grown covering the channel between the gold electrodes. The steps involved in the device fabrication process is schematically represented in **Figure 4.1d**. The electrodes with a channel length of 40 μm were fabricated using shadow mask through thermal evaporation method (**Figure C4.1b, Appendix**). The electrode deposited PDMS substrates were first treated with 3-mercaptopropyl trimethoxy silane (MPTES) to promote the adhesion of Au NP-PA network to the substrate and to obtain a homogeneous growth. The silane group of MPTES binds with the PDMS substrate and the -SH stretching has affinity towards gold surfaces. These thiol groups bind covalently with Au NPs and help in attaching them to the substrate. Such organosilanes such as 3-mercaptopropyl trimethoxysilane, 3-amino-propyle trimethoxy silane, 3-aminopropyl-methyl-diethoxysilane are used to covalently attach Au NPs to silicon or PDMS substrates with the help of its anchoring thiol or amine group that has large affinity towards gold surfaces.[17, 24-26]

Subsequently, the dispersion of Au NP-PA assembly was consecutively cast over the treated surface and the channel coverage improved with the number of deposition cycles (**Figure C4.2, C4.3, Appendix C**). A homogeneous distribution was obtained after 6 layers of deposition that covered the channel area and long percolation channels of Au NP – PA were observed. On the contrary, 6 consecutive layers of bare Au NP deposition created a segregated NP film and the NPs were concentrated mostly at the circumference of the cast (**Figure C4.4. Appendix C**). A comparison study was carried out, where I-V responses of as-synthesised Au NP, Au NP-PA assembly and Au NP-PA assembly after treating the substrate with MPTES (**Figure C4.11, Appendix C**) were recorded. A higher current was observed in the Au NP-PA network device in comparison to as-synthesised Au NP- device, which could be due to cross-linked NPs in the Au NP-PA network, that established conductive percolation channels facilitating carrier tunnelling between the particles. Negative surface potential of Au NP due to electron transfer from pyridine-N of 2-PA molecules to the vacant orbitals of Au through σ donation could be another plausible reason for observed enhanced current. The substrate treated with 3-mercaptopropyle trimethoxy silane recorded further enhancement in the current, which could possibly be due to the stronger attachment of the same to the substrate and the electrodes and uniform coverage across the channel.

Thereafter, to complete the sensor, a micropatterned PDMS layer was used at the top of the Au NP-PA network layer. This micropatterned flexible PDMS layer was fabricated using photolithography techniques, where lithographycally developed photoresist micropatterns over Si/SiO_2 wafer served as the moulds. The regularly patterned wells/caves of the templet mould can be clearly observed (**Figure C4.12, Appendix C**). PDMS elastomer was spun over the templet, thermally cured and released to get the desired patterns, morphology of which is presented in **Figure 4.1e, f.** Truncated conical shapes with top diameter of 3 µm and bottom diameter 6 µm were obtained. The detailed device fabrication process is described in the experimental details section. The purpose of using this micropatterned top PDMS layer is to couple the triboelectric effects through contact electrification between Au NP- PA network and PDMS to generate tactile responses. Surface topography plays a critical role in enhancing the triboelectric effect due to effective increase in the contact area between the materials and also elevate sensitivity and the range of detection.[27, 28] Triboelectric effects between different surfaces have been ascribed to charge transfer between the surfaces and have been utilised not only as a strain sensor but also as a novel technology that can harvest mechanical energy to electricity.

4.5 Multi-Stimuli Responses

To analyse the strain sensitivity, the skin-like flexible device was fixed on a PET substrate and device responses were recorded on mechanical concave (compressive strain) and convex (tensile strain) bending conditions. Strain experienced due to concave and convex bending angle can be obtained from the largely adopted equation below-

$$\varepsilon = h/2R \qquad \textbf{4.1}$$

where, h and R represents the thickness of the device and radius of curvature on bending. On application of convex bending (strain, ε=1.5%) the output current of the device increased and upon releasing the strain the device response recovered to its original value (**Figure 4.2a**). The corresponding $\Delta R/R_0$ was observed to be 0.62 (62%) (**Figure 4.2b**). The bending responses of the device at different convex bending were monitored at a bias voltage of 0.5V and it has been observed that with increase in the bending angle (from ε =0.37% to ε=3.7%), the output current of the device increased (**Figure 4.2c**). Similarly, the electrical response of the device at concave bending angle (ε =1.5%) was also increased (**Figure 4.2d**) and the corresponding $\Delta R/R_0$ was observed to be 0.88 (88%) (**Figure 4.2e**). The response of the device at increasing concave bending angle (ε =0.37% to ε=3.7%) exhibited increase in the output current and is shown in **Figure 4.2f**.

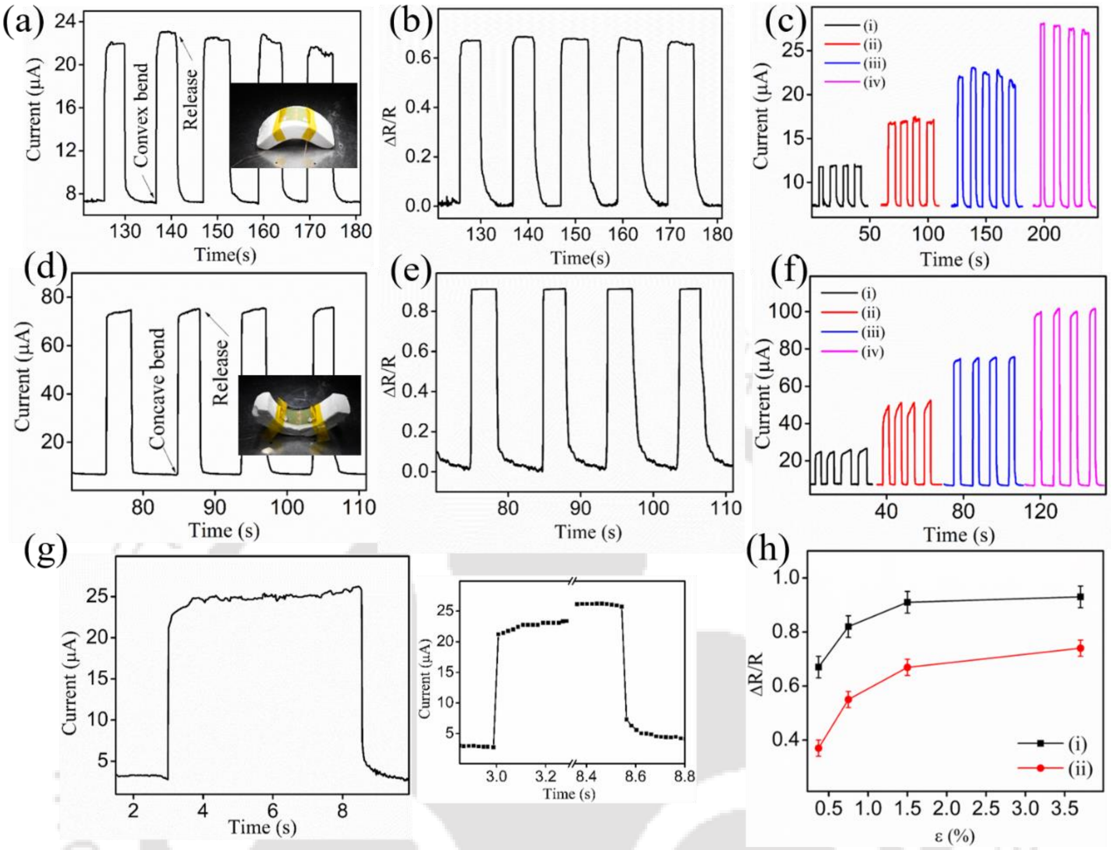

Figure 4.2. (a) Electric response at a convex bending angle (strain=1.5%), (b) corresponding ΔR/R0 ratio and (c) response at convex bending strain of (i) 0.37, (ii) 0.75, (iii) 1.5%, (iv) 3.7%. (d) Electric response at a concave bending angle (strain=1.5%), (e) corresponding ΔR/R0 ratio and (f) response at concave bending strain of (i) 0.37, (ii) 0.75, (iii) 1.5%, (iv) 3.7%. (g) Response and decay profiles, (h) ΔR/R0 vs strain plot and (h) ΔR/R0 vs ε plot (i) compressive strain (concave bending) (ii) tensile strain (convex bending).

The increase in the conductivity due to both convex and concave bending angles is possibly due to the combined effects of strain induced piezo-tronic effects and the triboelectric effects. Upon bending, the Au NP network would not only experience the concave and convex deformation but also the pressure exerted by the micropatterned layer. Thus, conductive pathways were established, which resulted in increase in output currents. Upon concave bending, the top layers of NP network would experience compressive strain and bottom layer would experience tensile strain, whereas, upon convex bending, the top layer would experience tensile strain while bottom layers would experience compressive strain. Effectively, either of concave or convex bending would generate piezotronic and triboelectric effects. So, an overall increase in the conductive channels could be expected, which would result in increase in the current output. Upon increasing the bending angle, the contact area between the NP layer and patterned PDMS layer would increase and a larger pressure would be exerted to the NP network. Due to this, better conductive channels could be expected, which might possibly be the reason for increase in the current output with increase in the bending angle (**Figure 4.2c, f**). Fast response time of 20 ms and decay time of 20 ms under 0.5 V bias condition was observed (**Figure 4.2g)**. $\Delta R/R_0$ ratio with concave and convex strain is represented in **Figure 4.2h**. 100 cycles of convex bending responses were recorded (**Figure C4.13, Appendix C**), the results of which suggested fatigue robustness of the device response.

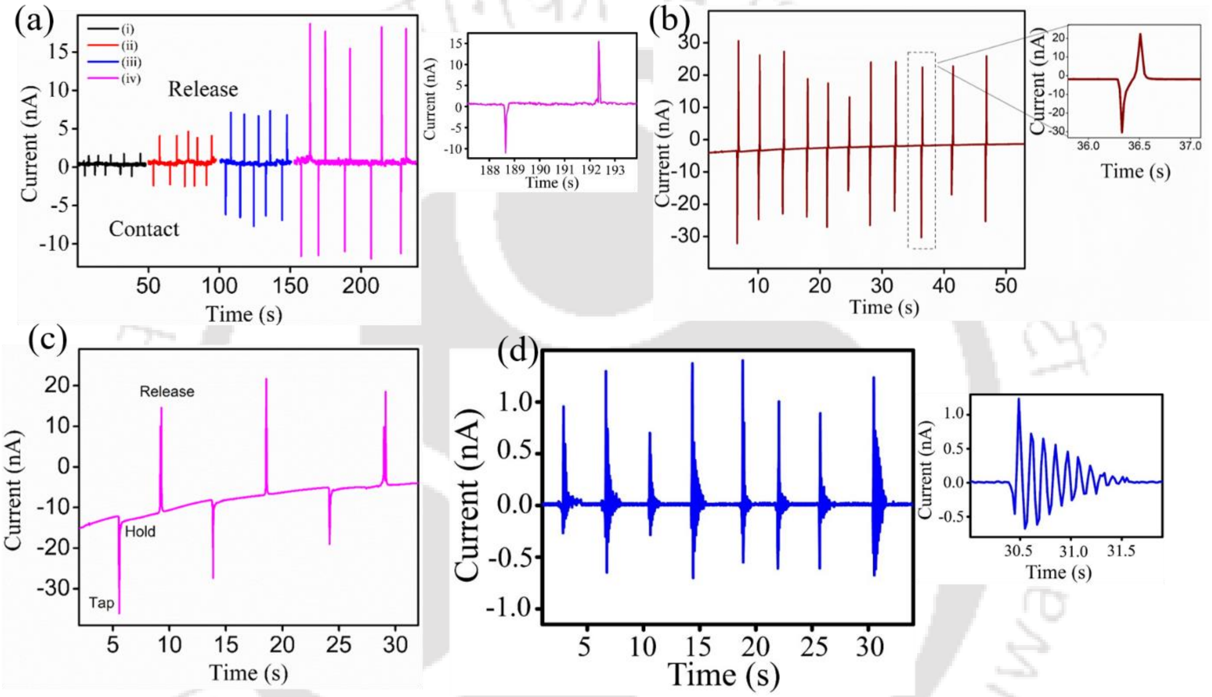

Figure 4.3. (a) Current response of the device on contact and release of (i) 0.5 g, (ii) 1.5 g (iii) 3.5 g (iv) 6.0 g, (b) current response under tapping action, (c) current response under tap hold and release action and (d) response to mechanical vibrations.

To understand the pressure sensitivity, as a proof of concept, we have demonstrated the device’s capability to recognize different weights. Pressure sensors convert pressure stimuli to electrical signals. The network of Au NP-PA sandwiched between electrode patterned bottom PDMS layer and microstructured top PDMS was observed to be sensitive to pressure exerted by variable weights. For this experiment, weights of 0.5 g, 1.5 g, 3.5 g and 6g were used to see response of the device when placed over it. Oppositely polar responses on contact and release mode (**Figure 4.3a**) were observed i.e., on contact, a negative current pulse was observed, whereas after withdrawing the weight, a positive pulse was observed. With increase in the weight, greater current pulses were recorded possibly due to magnitude of stress in the region of contact between the micropatterned layer and the Au NP-PA network layer. Device responsivity towards pressure was due to triboelectric effect between the Au NP-PA assembly layer and the PDMS layer.

Tribolelectric sensors work on the principle of generation of electricity due to contact electrification and electrostatic induction. When the two surfaces are in contact due to external stress, triboelectric charges are generated at the interface between the two the layers, i.e., positive charges are developed at the surface of one material and negative charges on the other (at the interface) according to their electron affinities. So, during contact, electrons from the AuNP-PA assembly are attracted towards the PDMS layer, which results in a negative current pulse and during release compensating charges give rise to the positive current pulse (**Figure 4.3a**).[27-29] So, alternating current outputs were observed for repeated contact and release action. Patterned PDMS structures in this regard enhance the generation of triboelectric charges and surpass the effects exhibited by flat/unstructured surfaces. This could be attributed to (1) generation of greater surface charges due to increased friction (2) change in the dielectric constants due to air voids and (3) ease of separation of triboelectric charges.[30] It can be inferred from previous reports that, increasing the contact area between the surfaces substantially improves electrification process, and hence the device performance. Also, the deformation magnitude of microstructures critically influences the output response. The triboelectric charge generated could be quantified using the formula in Eq 4.1 and 4.2 (Appendix C) and it can be understood from the equation that the electric field generated is dependent on permittivity of air, amount of charge transferred and the relative dielectric constant of the dielectric layer. The voltage developed across the two layer could be represented by equation 4.5 (Appendix C) and is dependent on permittivity of vacuum, triboelectric charge density and the gap between the two layers.[31] Therefore, the micropatterned PDMS layer having truncated conical shapes with a feature size of 3 µm (smaller diameter) conformed to deformed states corresponding to the pressure experienced by it due to the applied weight which altered the contact area and the distance between the two layers. This in turn, changed the air gap and friction between the two layers to produce triboelectric charges corresponding to the applied pressure. With this principle, the sensors can identify variable weights when placed over it. Current output due to contact electrification under multiple tapping on the device with finger under self-biased mode is presented in **Figure 4.3b** and output under tap hold and release mode is shown in **Figure 4.3c**. The current output under each tapping action showed distinct oppositely polar peaks that corresponded to different stages of application of pressure. Furthermore, the quick triboelectric charging/discharging mechanism allowed the detection of high-frequency contact vibrations. Damping peaks of the vibrational movement can be clearly observed (**Figure 4.3d**) and synchronicity can be established between dampening vibrational movements and the current output.

4.6 Physical Activity Recognition

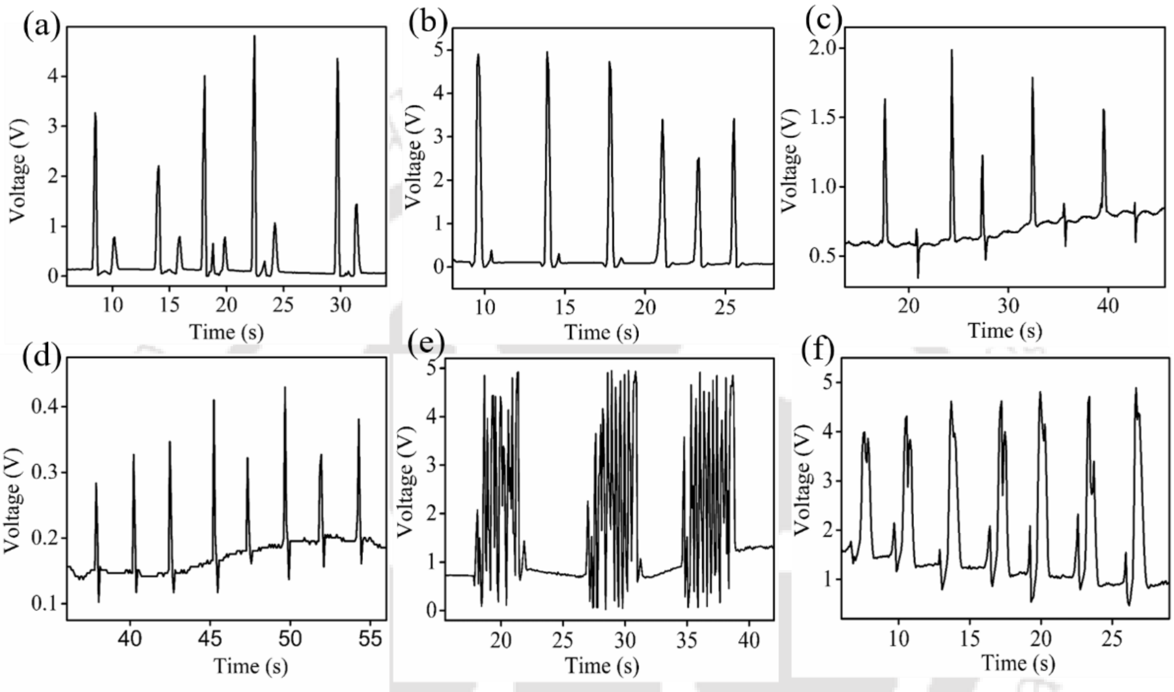

Figure 4.4. (a) Response of the device while (a) standing from sitting position, (b) leg movements in sitting position, (c) contact and release of weight, (d) tapping action, (e) jogging and (d) leg movements in standing position.

Considering its frequency responses, the device could be effectively employed in healthcare applications. For instance, the device was also used to recognize different physical activities. Experiments were carried out to document motion responses to physical activities such as sitting and standing, leg movements and jogging activities (**Figure 4.4a-f**). The device was paired to a microcontroller unit to record the device responses, and a moving average filter algorithm was employed to recognize the patterns. The sensor was tied to the wrist and responses were recorded corresponding to different physical activities. The physical activities were translated to contact and separation sequences between the Au NP-PA network and the micro-patterned layer. **Figure 4.4a** shows the records of the real time response while standing up from sitting position and sitting back. Two distinct peaks with different intensities corresponding to standing up (larger peak) and sitting down (smaller peak) were observed, which could be due to muscular movements and vibrations. **Figure 4.4b** represents real time response of leg movements in sitting posture. With upward motion of the leg a positive voltage pulse was observed and while bringing it back to the rest, a small change in the voltage was observed. The measurements were carried out for alternate leg movements to confirm the responses. Placing and releasing of weight and tapping action on the sensor are shown in **Figure 4.4c, d**. On the onset of pressure due to weight and tapping action, an increased voltage pulse across the sensor was recorded and while releasing a decreased voltage pulse was observed, which could be attributed to contact electrification and electrostatic induction as discussed before. Real time response of jogging activity was recorded, which produced multiple peaks corresponding to the leg movements during the jogging activity (**Figure 4.4e**). The fast response time of the sensor enabled the detection of high frequency responses of leg movements during the activity. To obtain a clear picture about the responses of the jogging activity, responses due to leg movements in steady standing condition was observed. **Figure 4.4f** represents the response corresponding to (alternate) leg movements in standing condition. These results supported that the responses were due to leg movements and not merely due to hand movements during jogging activity. Therefore, assessing the nature and frequency of device response, it could be applied to recognise human activities. Such systems find wide scale applicability as fitness bands, activity recognition bands in healthcare, prosthetics as well as in robotic interfaces. Novel flexible sensors based on piezo-resistive and piezo-capacitive sensing mechanisms are effective in detecting tactile responses but suffer from slower readout because of which they are not suitable for dynamic pressure sensing applications. In this regard, triboelectric sensing mechanisms have recently gained importance owing to their ability to meet the requirement of high sensitivity, increased detection range, zero power consumption and low cost of production. The device developed in this work not only responded to bending deformations but also to mechanical vibrations (dynamic pressure). The change in resistance of Au NP-PA network layer and the triboelectric contact potential developed are the key parameters for its high sensitivity towards physical deformations. The combination of triboelectric potential and resistive responses are the main focus here to detect both static and dynamic stimuli together, mimicking the human sensory receptors. Such a system using controlled assembly of Au NP has not been reported before and its feasibility for use in wearable bands to monitor physical activities were demonstrated.

4.7 Piezo-Resistive Characteristics

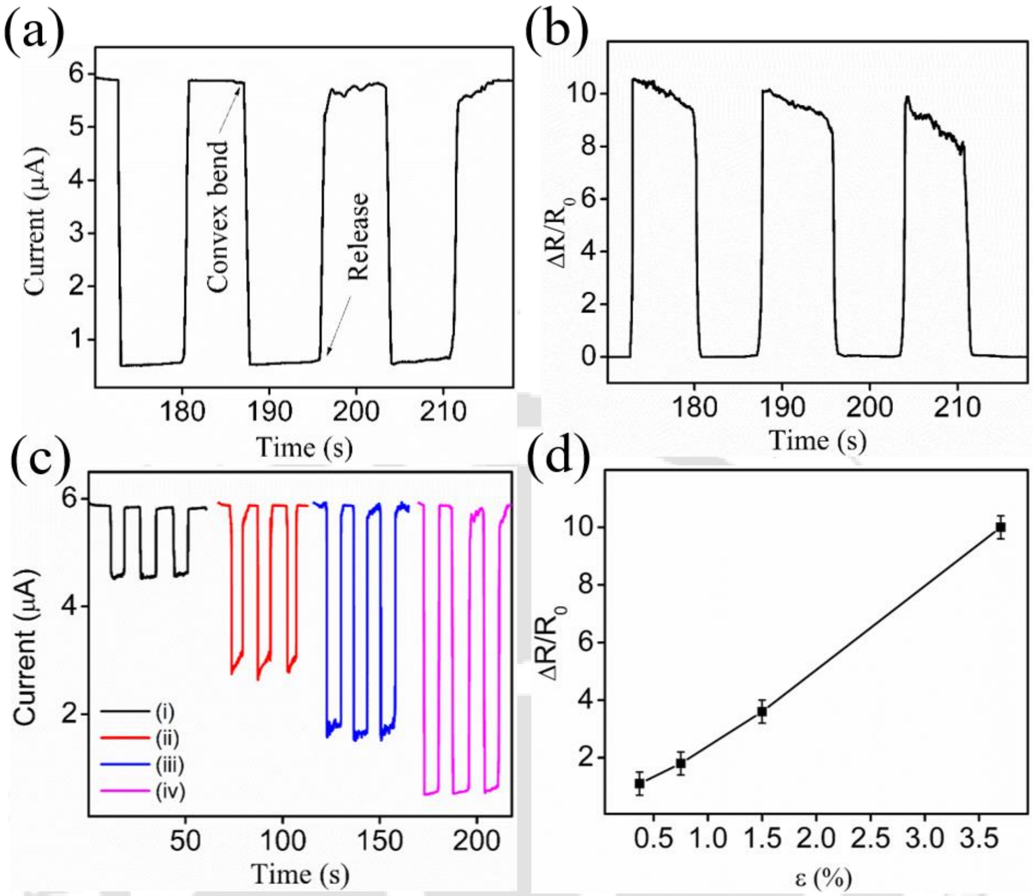

Figure 4.5. (a) Electric response at a convex bending angle (strain=3.7%), (b) corresponding $\Delta R/R_0$ ratio, (c) response at convex bending strain of (i) 0.37, (ii) 0.75, (iii) 1.5%, (iv) 3.7% and (d) $\Delta R/R_0$ ratio vs convex strain.

To study the piezoelectric behaviour of the Au NP-PA assembly, the device responses at different bending angles (concave and convex) were observed without the micro-structured PDMS layer. It can be observed from **Figure 4.5a**, that the current output decreased with convex bending (tensile strain=3.7%). The corresponding $\Delta R/R_0$ can be observed in **Figure 4.5b** where $\Delta R/R_0$ of 9±0.4 was observed for a tensile strain of 3.7%. Conversely, an increase in output current (decrease in device resistance) was observed, when concave bending angle (compressive strain) was applied (**Figure C4.14, Appendix**). $\Delta R/R_0$ ratio of 7±0.3 was observed for a compressive strain of 3.7%. For a highly sensitive stain sensor, a high value of gauge factor is desired. Gauge factor of the assembled Au NP-PA network was obtained using the standard and widely adopted formula:

Gauge Factor (GF) = $(\Delta R/R_0)/\varepsilon$ **4.2**

Where, ΔR change in resistance due to the applies strain ε, R_0 is the absolute resistance of the device. ε here was calculated using equation 1. The Gauge factor was found to be 243 ± 10 at a low applied strain of 3.7% (tensile strain). Sensing performance of a strain sensor was quantitatively measured by high gauge factor at a significantly low applied strain. However, it is extremely challenging to obtain gauge factor that is larger than 100 (**Table C1, Appendix C**). Therefore, such an approach of creating higher order assembly of uniformly spaced Au NP through molecular binding, would provide us with an easy and efficient route to develop piezoresistive sensors inheriting a high gauge factor. A decreasing trend of current was observed with increase in the tensile strain (**Figure 4.5c**). The corresponding $\Delta R/R_0$ ratio vs tensile strain is plotted in **Figure 4.5d**. A high gauge factor of 243± 10 for tensile strain and 200 ± 8 for compressive strain demonstrated high strain sensitivity of the device making it a promising candidate for motion detectors and health monitoring systems. High sensitivity of the Au NP-PA network layer can be explained by tunnelling of electrons in between the NPs linked together by the molecular linker. As mentioned before, sub-nanometer range inter particle distance of 0.6 nm with negative surface charges facilitated enhanced charge conduction in the Au NP-PA network layer and exhibited strain sensitive output current. So, when tensile strain was applied, the Au NP – PA network conformed to a stretched state where the inter-particle distance increased, because of which carrier tunnelling between the NPs was reduced and we observed a reduction in the output current (**Figure 4.5a**). On the contrary, when compressive strain was applied, the inter-particle distance might have been reduced, which resulted in the increase in the output current (**Figure C4.14, Appendix C**).

4.8 Piezo-Phototronic Detection

We expanded our interest towards studying piezophototronic behaviour of Au NP-PA network by taking into account the surface plasmon resonance in metallic NPs. It is well established that in metallic nanostructures, when impinged with photons of appropriate energy, electron clouds (localized surface plasmons) are generated within the metal nanostructured framework, that collectively oscillates and is termed as surface plasmon resonance. Rupture of these oscillating electron clouds results in electron-electron scattering at the nanostructure surface and generation of high energy electrons known as hot electrons. These hot electrons, can be utilized for up-conversion of photonic energy to electric current (photoelectric efficiency) in photodetectors at the wavelength of resonance. Recent report from our group illustrated that the higher order assembly of Au NP exhibits higher degree of surface plasmons at the hot-spots between the NPs, which facilitates interesting chemical reactions with enhanced reaction rate.[32] Therefore, we extended our interest towards studying piezo-phototronic behaviour in the Au NP - PA network. Photoconductive effects of these Au NP-PA network layers were investigated under white light illumination (2 mA/W, bias voltage = 0.1 V) (**Figure C4.15, Appendix C**). Compared to the device made with as-synthesised Au NPs, the Au NP-PA network device showed enhanced photoconductive properties. A typical Au NP-PA network device showed 2-fold increase in the photocurrent with good reproducibility and stability, whereas the as-synthesised Au NP device showed only 40% increase in the photocurrent generation (**Figure C4.16, Appendix C**). Wavelength dependent responsivity of Au NP-PA network device showed higher responsivity in comparison to as-synthesised Au NP device (**Figure C4.16, Appendix C**). In particular, the Au NP-PA device exhibited maximum responsivity of 2.5 A/W and detectivity of 3.5×10^{13} Jones between 650-700 nm whereas the bare Au NP device exhibited responsivity of 25 mA/W and detectivity of 3×10^{12} between 500-550 nm wavelengths of irradiation. It was also observed that, the minimum voltage required to obtain the photoresponse in as-synthesised Au NP device was 2 V, whereas, high response was recorded for Au NP-PA network device for a bias voltage as low as 0.1 V (**Figure C4.17, Appendix C**). The enhanced photocurrent generation and low operating voltage in the Au NP-PA network device might be owing to a higher degree of Au NP aggregation, which created more surface plasmons and increased the hot carrier population in the Au NP-PA assembly.

Subsequently, to illustrate the strain induced photoresponse, the device characteristics were investigated under tensile strain of 3.7%. It was observed that, the device exhibited photoresistive behaviour under applied mechanical strain i.e., the magnitude of output current decreased with tensile strain at an illumination intensity of 2 mW/cm^2(**Figure 4.6a**). **Figure 4.6b** demonstrated the strain modulated photoresponse, where increase in the tensile strain exhibited an increase in the photoresistive behaviour. In particular, higher photo-resistive behaviour was observed for tensile stain of 3.7% than that for a tensile strain of 0.37% at an illumination intensity of 2 mW/cm^2. Greater mechanical strain on the NP assembly produced greater photo-response, indicating a strong synergy between the piezophototronic effect and LSPR. As discussed before, due to tensile strain, the Au NP network adopted a stretched conformation state where the interparticle distance increased as a result of which a poor carrier tunnelling could be expected between the NPs.

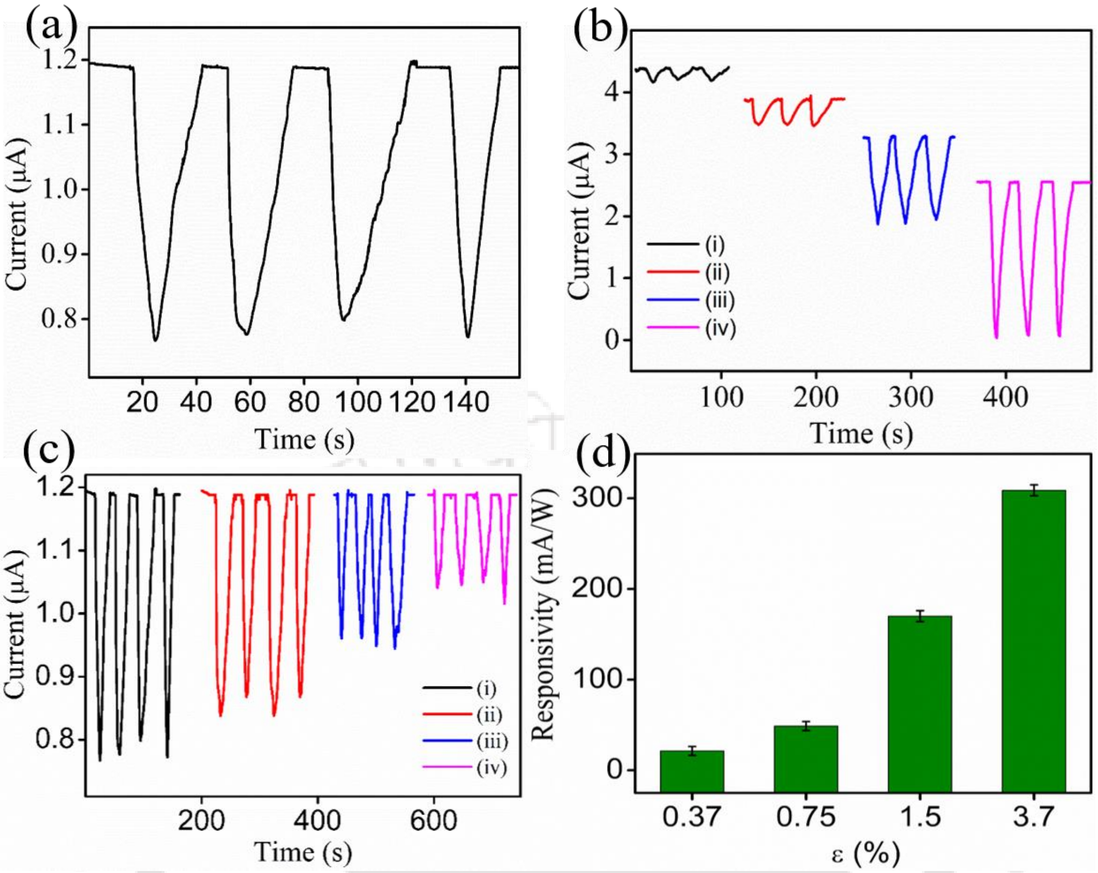

Figure 4.6. (a) Strain induced photoresistive characteristics of Au NP-PA assembly device (ε=3.7%), (b) photoresponse at a tensile strain of (i) ε=0.37% (ii) ε=0.7% (iii) ε=1.5% (iv) ε=0.37%, (c) photoresponse at ε=0.37% at illumination intensity of (i) 2 mW/ cm^2 (ii) 1.5 mW/ cm^2 (iii) 1 mW/ cm^2 (iv) 0.5 mW/ cm^2 and (e) responsivity vs strain plot of Au NP-PA assembly device.

So, under light illumination, photoexcited hot carriers experienced a resistive pathway due to increase in the interparticle distance and underwent scattering within the system and thereby reduced the output current under applied tensile strain. In addition to this, internal heating within the framework due to carrier scattering may also have influenced the decrease in current upon photo-illumination. Therefore, with an increased degree of deformations, greater photo-resistive behaviour was observed. Further to show the effectiveness of the Au NP-PA assembly device, the illumination intensity dependent photoresponse was measured at a tensile strain of 3.7% (**Figure 4.6c**) and with decrease in the illumination intensities from 2 mW/cm^2 to 0.5 mW/cm^2, a decreasing photoresponse trend was observed. Responsivity vs tensile strain is plotted in **Figure 4.6d** where increase in responsivity with increase in the tensile strain was observed. For example, responsivities of 21 mA/W, 48 mA/W, 170 mA/W and 309 mA/W were observed for tensile strain of 0.37%, 0.75%, 1.50% and 3.7%, respectively. These results demonstrated that the Au NP-PA network-based strain sensor is also capable of detecting light at a low bias voltage of 0.1 V and the detection efficiencies can be modulated by mechanical strain due to their piezo-phototronic behaviour. A summary of performance parameters that compares previous research to ours is presented in **Table C2** (**Appendix C**).

4.9 Conclusions

In a nutshell, a 3D network of Au NP was created through ligand interaction with PA ligand. The bonding between the Au NP and the ligand was explained based on the transfer of electrons from pyridine-N site of the ligand to the vacant orbitals of Au through σ donation. A probable π-back donation from Au valence orbital to pyridine-N π* orbital was also involved in the bond formation. The 3D network of Au NP was formed through the hydrogen bonds between the free NH_2 group of the ligand bonded to Au NPs. Based on these NP networks and a lithographically patterned PDMS microstructures, a multi-stimuli responsive tactile sensor was developed that effectively transduced mechanical strain to electrical responses. Micropatterned PDMS layer was used to couple triboelectric potential through contact electrification between the PDMS layer and Au NP-PA network. These highly sensitive devices could effectively distinguish between variable weights, detect finger tapping action and were also ultra-sensitive to vibrational movements. The proposed device recognised different physical activities like sitting-standing motion, jogging and leg movements, which validated its significance towards physical activity monitoring devices. These Au NP-PA network exhibited piezoresistive characteristics with a high gauge factor of 243±10, which was utilized to detect different degree of compressive and tensile strains applied to it. Enhanced photo responsive characteristics in assembled Au NP-PA network was used to detect visible light, which added to the multifunctional attributes of the tactile sensor. A responsivity of 2.5 A/W and detectivity of 3.5×10^{13} Jones were observed in the Au NP-PA network device whereas, responsivity of 25 mA/W and detectivity of 3×10^{12} were observed in Au NP device in flat condition. In addition, the Au NP-PA device exhibited strain dependent plasmonic-photodetection with a responsivity of 309 mA/W at a tensile strain of 3.7%. Its highly sensitive tactile responses together with strain sensitive photodetection performances led us to design and develop more comprehensive multifunctional tactile and piezo-phototronic sensors. The multi-stimuli responsive Au NP-PA network demonstrated here opens up new perspectives to develop artificially intelligent multifunctional systems and is promising in designing wearable bands for physiological activity monitoring.

4.10 References

1. He, F.; You, X.; Gong, H.; Yang, Y.; Bai, T.; Wang, W.; Guo, W.; Liu, X.; Ye, M. Stretchable, Biocompatible, and Multifunctional Silk Fibroin-Based Hydrogels toward Wearable Strain/Pressure Sensors and Triboelectric Nanogenerators. *ACS Applied Materials & Interfaces*. **2020**, 12, 6442-6450.

2. Huang, L.-B.; Xu, W.; Zhao, C.; Zhang, Y.-L.; Yung, K.-L.; Diao, D.; Fung, K. H.; Hao, J. Multifunctional Water Drop Energy Harvesting and Human Motion Sensor Based on Flexible Dual-Mode Nanogenerator Incorporated with Polymer Nanotubes. *ACS Applied Materials & Interfaces*. **2020**, 12, 24030-24038.

3. Tang, R.; Meng, Q.; Wang, Z.; Lu, C.; Zhang, M.; Li, C.; Li, Y.; Shen, X.; Sun, Q. Multifunctional Ternary Hybrid Hydrogel Sensor Prepared via the Synergistic Stabilization Effect. *ACS Applied Materials & Interfaces*. **2021**, 13, 57725-57734.

4. Wang, X.-m.; Chai, Y.; Wang, Z.-p.; Yu, J.; Chen, X.; Wong, C. P. Metal Oxides/Carbon Felt Pressure Sensors with Ultra-Broad-Range High Sensitivity. *Advanced Materials Interfaces*. **2021**, n/a, 2101663.

5. Wang, C.; Dong, L.; Peng, D.; Pan, C. Tactile Sensors for Advanced Intelligent Systems. *Advanced Intelligent Systems*. **2019**, 1, 1900090.

6. Liu, H.; Li, M.; Ouyang, C.; Lu, T. J.; Li, F.; Xu, F. Biofriendly, Stretchable, and Reusable Hydrogel Electronics as Wearable Force Sensors. *Small*. **2018**, 14, 1801711.

7. Chen, X.; Zeng, Q.; Shao, J.; Li, S.; Li, X.; Tian, H.; Liu, G.; Nie, B.; Luo, Y. Channel-Crack-Designed Suspended Sensing Membrane as a Fully Flexible Vibration Sensor with High Sensitivity and Dynamic Range. *ACS Applied Materials & Interfaces*. **2021**, 13, 34637-34647.

8. Sun, J.-Y.; Keplinger, C.; Whitesides, G. M.; Suo, Z. Ionic skin. *Advanced Materials*. **2014**, 26, 7608-7614.

9. Kim, W.-G.; Kim, D.-W.; Tcho, I.-W.; Kim, J.-K.; Kim, M.-S.; Choi, Y.-K. Triboelectric Nanogenerator: Structure, Mechanism, and Applications. *ACS Nano*. **2021**, 15, 258-287.

10. Rahman, M. T.; Rana, S. M. S.; Zahed, M. A.; Lee, S.; Yoon, E.-S.; Park, J. Y. Metal-organic framework-derived nanoporous carbon incorporated nanofibers for high-performance triboelectric nanogenerators and self-powered sensors. *Nano Energy*. **2022**, 94, 106921.

11. Durukan, M. B.; Cicek, M. O.; Doganay, D.; Gorur, M. C.; Çınar, S.; Unalan, H. E. Multifunctional and Physically Transient Supercapacitors, Triboelectric Nanogenerators, and Capacitive Sensors. *Advanced Functional Materials*. **2022**, 32, 2106066.

12. Dinh Le, T.-S.; An, J.; Huang, Y.; Vo, Q.; Boonruangkan, J.; Tran, T.; Kim, S.-W.; Sun, G.; Kim, Y.-J. Ultrasensitive Anti-Interference Voice Recognition by Bio-Inspired Skin-Attachable Self-Cleaning Acoustic Sensors. *ACS Nano*. **2019**, 13, 13293-13303.

13. Liu, Y.-F.; Liu, Q.; Li, Y.-Q.; Huang, P.; Yao, J.-Y.; Hu, N.; Fu, S.-Y. Spider-Inspired Ultrasensitive Flexible Vibration Sensor for Multifunctional Sensing. *ACS Applied Materials & Interfaces*. **2020**, 12, 30871-30881.

14. Wang, H.; Zhou, R.; Li, D.; Zhang, L.; Ren, G.; Wang, L.; Liu, J.; Wang, D.; Tang, Z.; Lu, G.; Sun, G.; Yu, H.-D.; Huang, W. High-Performance Foam-Shaped Strain Sensor Based on Carbon Nanotubes and Ti3C2Tx MXene for the Monitoring of Human Activities. *ACS Nano*. **2021**, 15, 9690-9700.

15. Wang, Z. L. Triboelectric Nanogenerators as New Energy Technology for Self-Powered Systems and as Active Mechanical and Chemical Sensors. *ACS Nano.* **2013**, 7, 9533-9557.

16. Ketelsen, B.; Yesilmen, M.; Schlicke, H.; Noei, H.; Su, C.-H.; Liao, Y.-C.; Vossmeyer, T. Fabrication of Strain Gauges via Contact Printing: A Simple Route to Healthcare Sensors Based on Cross-Linked Gold Nanoparticles. *ACS Applied Materials & Interfaces.* **2018**, 10, 37374-37385.

17. Huang, C.-B.; Yao, Y.; Montes-García, V.; Stoeckel, M.-A.; Von Holst, M.; Ciesielski, A.; Samorì, P. Highly Sensitive Strain Sensors Based on Molecules–Gold Nanoparticles Networks for High-Resolution Human Pulse Analysis. *Small.* **2021**, 17, 2007593.

18. Olichwer, N.; Leib, E. W.; Halfar, A. H.; Petrov, A.; Vossmeyer, T. Cross-Linked Gold Nanoparticles on Polyethylene: Resistive Responses to Tensile Strain and Vapors. *ACS Applied Materials & Interfaces.* **2012**, 4, 6151-6161.

19. Pal, S.; Paul, S.; Chattopadhyay, A. Enhanced solid-state plasmon catalyzed oxidation and SERS signal in the presence of transition metal cations at the surface of gold nanostructures. *Physical Chemistry Chemical Physics.* **2021**, 23, 21808-21816.

20. Riskin, M.; Tel-Vered, R.; Lioubashevski, O.; Willner, I. Ultrasensitive Surface Plasmon Resonance Detection of Trinitrotoluene by a Bis-aniline-Cross-Linked Au Nanoparticles Composite. *Journal of the American Chemical Society.* **2009**, 131, 7368-7378.

21. Ojea-Jiménez, I.; Romero, F. M.; Bastús, N. G.; Puntes, V. Small Gold Nanoparticles Synthesized with Sodium Citrate and Heavy Water: Insights into the Reaction Mechanism. *The Journal of Physical Chemistry C.* **2010**, 114, 1800-1804.

22. Moon, S. W.; Ha, J. W. Influence of the capping material on pyridine-induced chemical interface damping in single gold nanorods. *Analyst.* **2019**, 144, 2679-2683.

23. Zhang, X.; Sun, C. Q.; Hirao, H. Guanine binding to gold nanoparticles through nonbonding interactions. *Physical Chemistry Chemical Physics.* **2013**, 15, 19284-19292.

24. Kuddannaya, S.; Chuah, Y. J.; Lee, M. H. A.; Menon, N. V.; Kang, Y.; Zhang, Y. Surface Chemical Modification of Poly(dimethylsiloxane) for the Enhanced Adhesion and Proliferation of Mesenchymal Stem Cells. *ACS Applied Materials & Interfaces.* **2013**, 5, 9777-9784.

25. Joseph, E.; Rajput, S. S.; Patil, S.; Nisal, A. Mechanism of Adhesion of Natural Polymer Coatings to Chemically Modified Siloxane Polymer. *Langmuir.* **2021**, 37, 2974-2984.

26. Heuer-Jungemann, A.; Feliu, N.; Bakaimi, I.; Hamaly, M.; Alkilany, A.; Chakraborty, I.; Masood, A.; Casula, M. F.; Kostopoulou, A.; Oh, E.; Susumu, K.; Stewart, M. H.; Medintz, I. L.; Stratakis, E.; Parak, W. J.; Kanaras, A. G. The Role of Ligands in the Chemical Synthesis and Applications of Inorganic Nanoparticles. *Chemical Reviews.* **2019**, 119, 4819-4880.

27. Tao, J.; Bao, R.; Wang, X.; Peng, Y.; Li, J.; Fu, S.; Pan, C.; Wang, Z. L. Self-Powered Tactile Sensor Array Systems Based on the Triboelectric Effect. *Advanced Functional Materials.* **2019**, 29, 1806379.

28. Ha, M.; Lim, S.; Cho, S.; Lee, Y.; Na, S.; Baig, C.; Ko, H. Skin-Inspired Hierarchical Polymer Architectures with Gradient Stiffness for Spacer-Free, Ultrathin, and Highly Sensitive Triboelectric Sensors. *ACS Nano.* **2018**, 12, 3964-3974.

29. Lin, L.; Xie, Y.; Wang, S.; Wu, W.; Niu, S.; Wen, X.; Wang, Z. L. Triboelectric Active Sensor Array for Self-Powered Static and Dynamic Pressure Detection and Tactile Imaging. *ACS Nano.* **2013**, 7, 8266-8274.

30. Fan, F.-R.; Lin, L.; Zhu, G.; Wu, W.; Zhang, R.; Wang, Z. L. Transparent Triboelectric Nanogenerators and Self-Powered Pressure Sensors Based on Micropatterned Plastic Films. *Nano Letters*. **2012**, 12, 3109-3114.

31. Lei, H.; Chen, Y.; Gao, Z.; Wen, Z.; Sun, X. Advances in self-powered triboelectric pressure sensors. *Journal of Materials Chemistry A*. **2021**, 9, 20100-20130.

32. Pal, S.; Dutta, A.; Paul, M.; Chattopadhyay, A. Plasmon-Enhanced Chemical Reaction at the Hot Spots of End-to-End Assembled Gold Nanorods. *The Journal of Physical Chemistry C*. **2020**, 124.

Appendix C

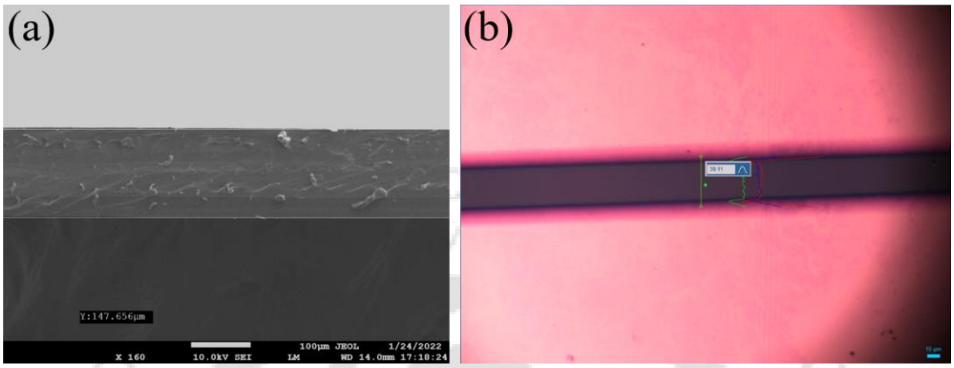

Figure C4.1. (a) Thickness of PDMS layer (150 µm) and (b) channel gap between the two electrodes.

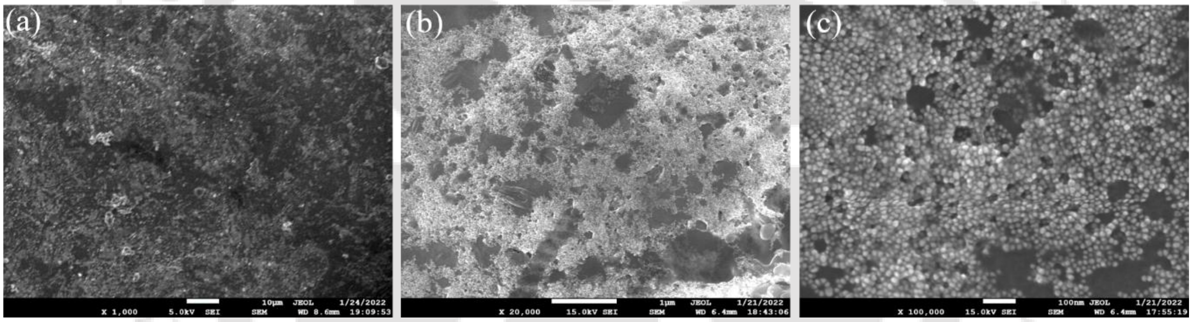

Figure C4.2. FESEM image of the channel area after 6st layer of deposition of Au NP-PA network.

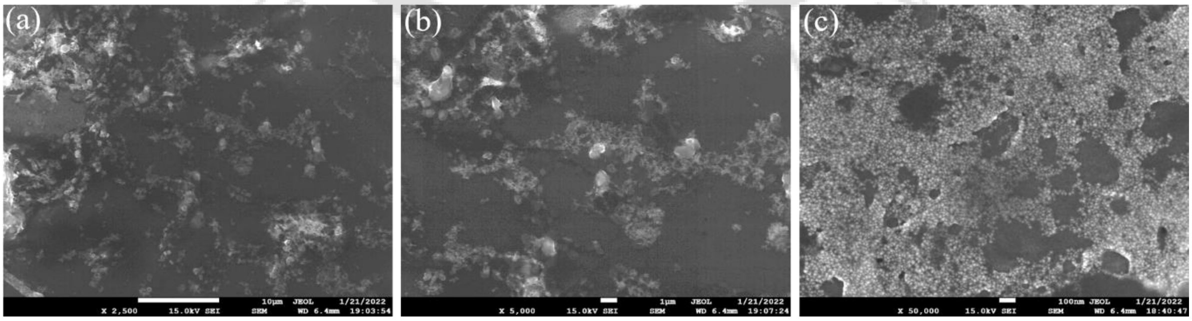

Figure C4.3. FESEM image of the channel area after 1th layer of deposition of Au NP-PA network.

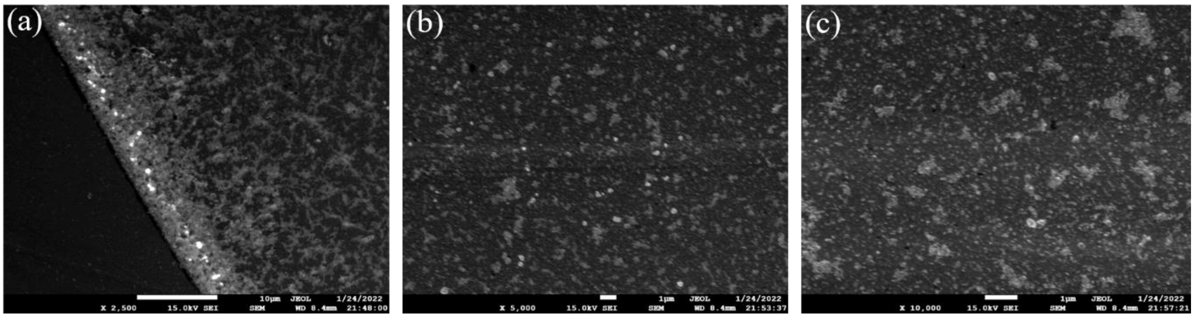

Figure C4.4. FESEM images of the channel area after 6th layer of deposition of bare Au NP.

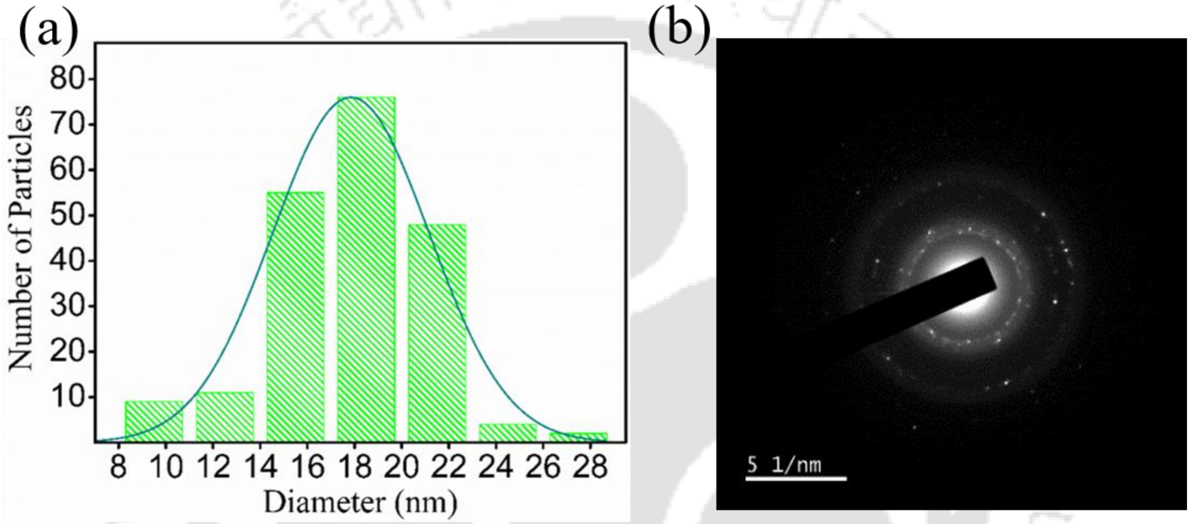

Figure C4.5. (a) Particle size distribution of Au NP and (b) selected area electron diffraction (SAED) patterns.

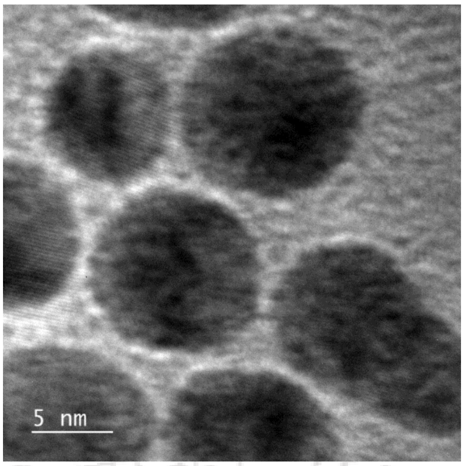

Figure C4.6. High resolution transmission electron microscopy image of Au NP assembly having average inter-particle distance of 0.6 nm.

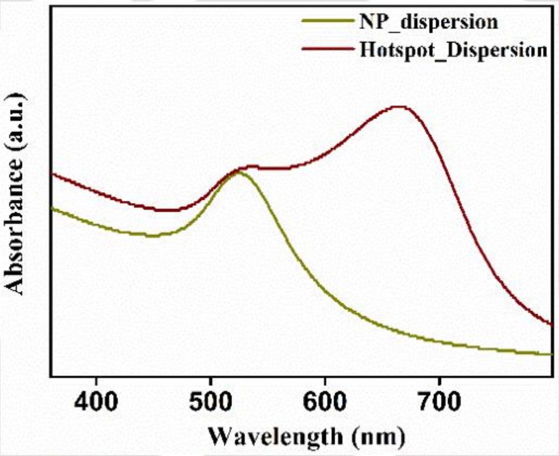

Figure C4.7. UV-vis absorbance spectra of Au NP and Au NP-PA network.

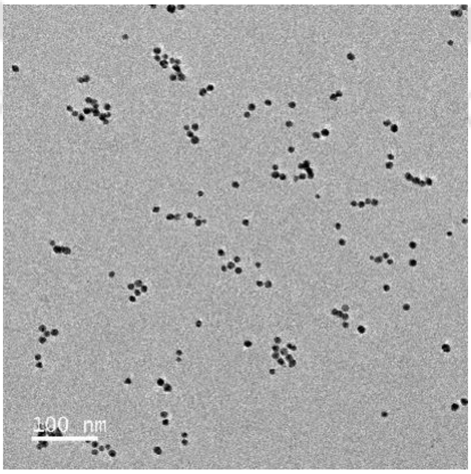

Figure C4.8. Transmission electron microscopy image of Au NP.

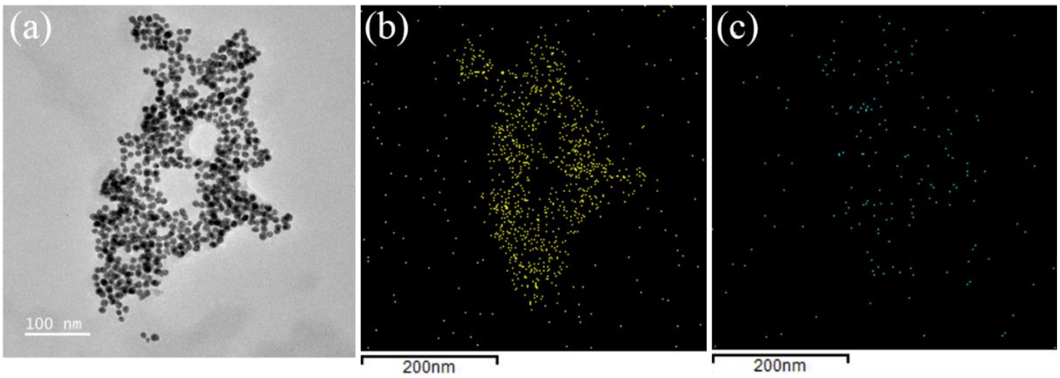

Figure C4.9. (a) Transmission electron microscopy image of Au NP-PA network. Elemental mapping nanoparticle population showing the distribution of (b) Au NP and (c) nitrogen.

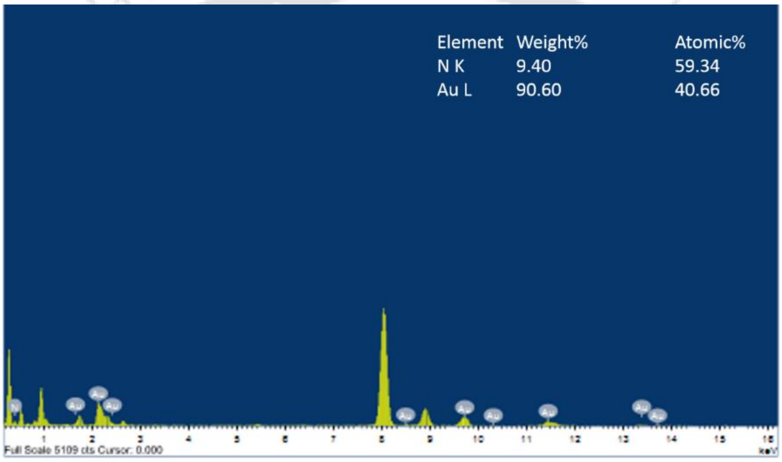

Figure C4.10. TEM-EDX spectra of Au NP-PA network showing elemental composition of gold and nitrogen.

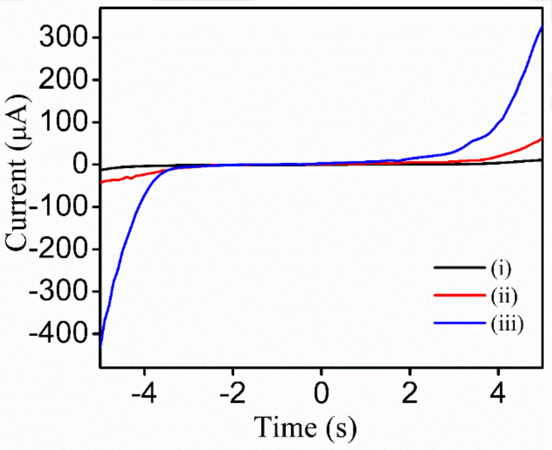

Figure C4.11. Current Vs Voltage plot of (i) as synthesised- Au NP device, (ii) Au NP-PA assembly device and (iii) Au NP-PA device whose substrate was treated with 3-mercaptopropyle trimethoxy silane.

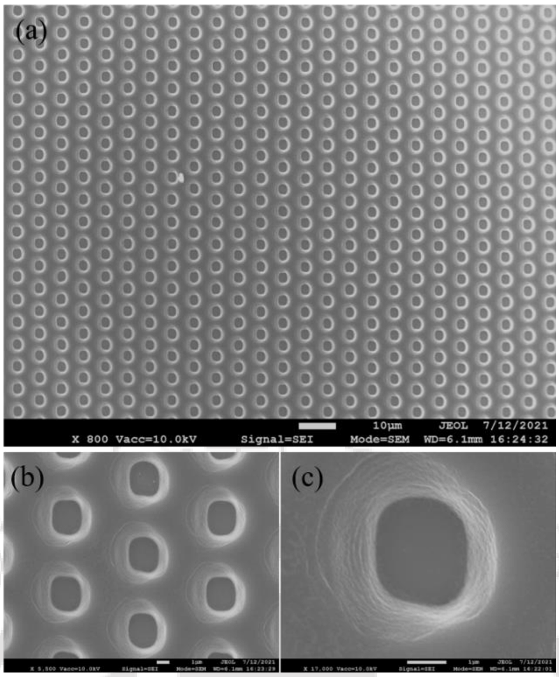

Figure C4.12. FESEM image of the mould used for developing patterned PDMS layer. (a) scale bar 10um (b) scale bar 1um (c) individual well developed on Si/SiO$_2$ substrate.

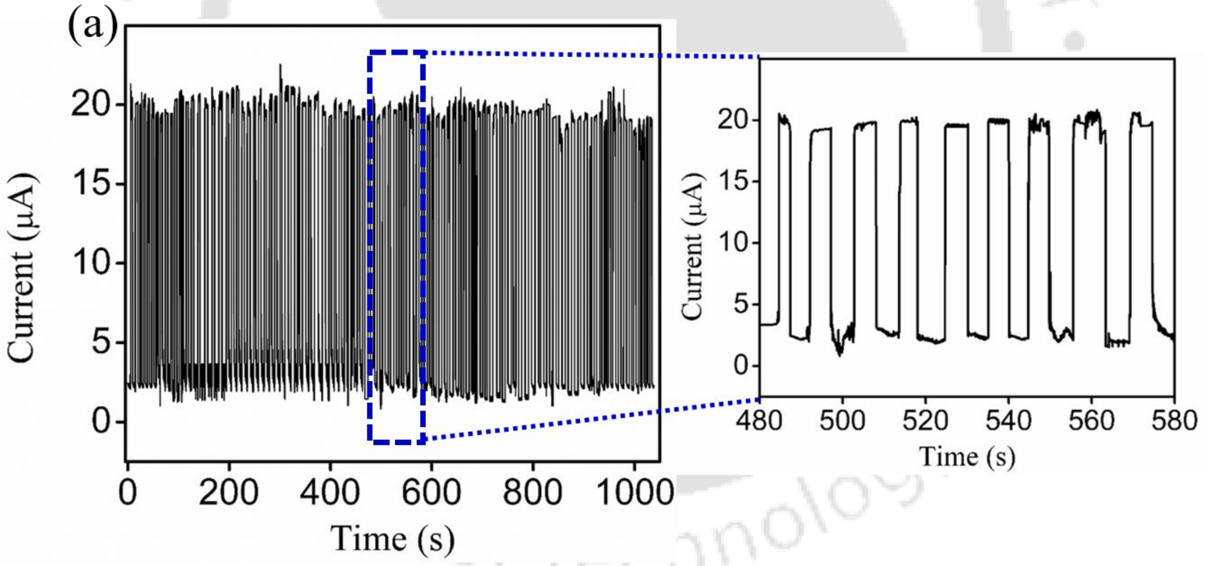

Figure C4.13. (a) Device response at convex bending angle for 100 cycles.

The strength of electric field between two layers of a triboelectric sensor can be represented by

In the air gap $\boldsymbol{E = \frac{\sigma_0 - \frac{Q}{S}}{\varepsilon_0}}$ **4.1**

In the dielectric layer $\boldsymbol{E_1 = \frac{-Q}{\varepsilon_0 \varepsilon_1 S}}$ **4.2**

Where, σ_0 corresponds to density of triboelectric charge; Q corresponds to amount the of transferred charge; ε_0 corresponds to the permittivity of vacuum; ε_1 corresponds to the relative dielectric constant of the dielectric layer and S corresponds to sensitivity.

Open circuit voltage across the two layers can be represented as

$$\boldsymbol{V_{oc} = \frac{\sigma_0 d_t}{\varepsilon_0}} \qquad \mathbf{4.3}$$

Where, d$_{(t)}$ represents the air gap.

Table C1. Comparison of performance parameters

Material	Deposition method	Detection range	Response time	Gauge factor	Ref.
AgNP	PDMS stamping	0-25%	1s	2.05 at ε = 20%	1
AgNP/polyurethane	Reduction reaction at Polyurethane substrate	Upto 200%	239.7 ms) / (274.0 ms	79, at ε =50%	2
8-MOA-exchanged Au NPs	Layer by layer deposition	0.075–0.785		26 at ε =0.075%	3
Ag nanoparticles/ Polyurethane-based stretchable fibers	Reduction reaction at Polyurethane substrate			659 at ε =200%	4
1,9-nonanedithiol cross-linked gold nanoparticle	Layer by layer sin coating and contact printing	−0.12 < ε < 0.12%		26	5
Cross-Linked Gold Nanoparticles on Polyethylene	layer-by-layer self-assembly			25	6
Silver Nanoparticles	dropcast	up to 25%	48 ms	60	7
Crosslinked Au NP with tetra(ethylene glycol) dithiol (SH-TEG-SH) linker	consecutive batch deposition	−0.63% to 0.63%	16.1 ms	126	8
Silver Nanowire–Elastomer Nanocomposite	Dropcast and optical heating	Upto 70%	200 ms	14 at ε = 70%	9
Crosslinked Au NP with picolyleamine	Layer by layer deposition	-3.7% to +3.7%.	40 ms	240±6 at ε =3.5%	This work

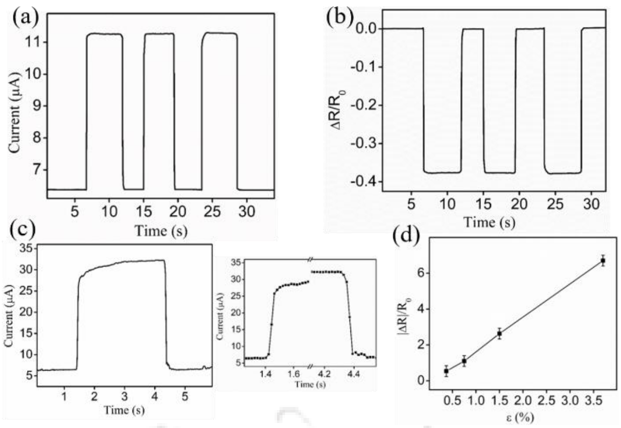

Figure C4.14. (a) Electric response at a concave bending angle (compressive strain of 0.75%), (b) corresponding $\Delta R/R_0$ ratio. (c) Response and decay profiles and (d) $|\Delta R|/R_0$ ratio vs strain (concave bending).

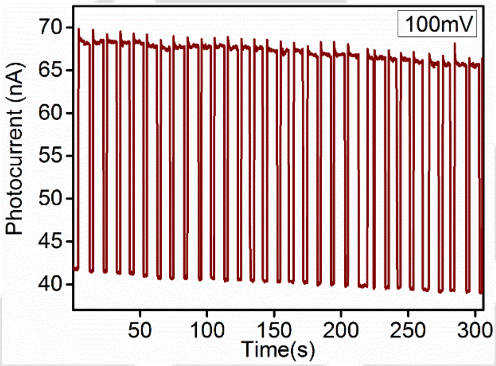

Figure C4.15. Photoresponse of Au NP-PA assembly device at an illumination intensity of 2 mW/cm^2 (bias voltage 100 mV).

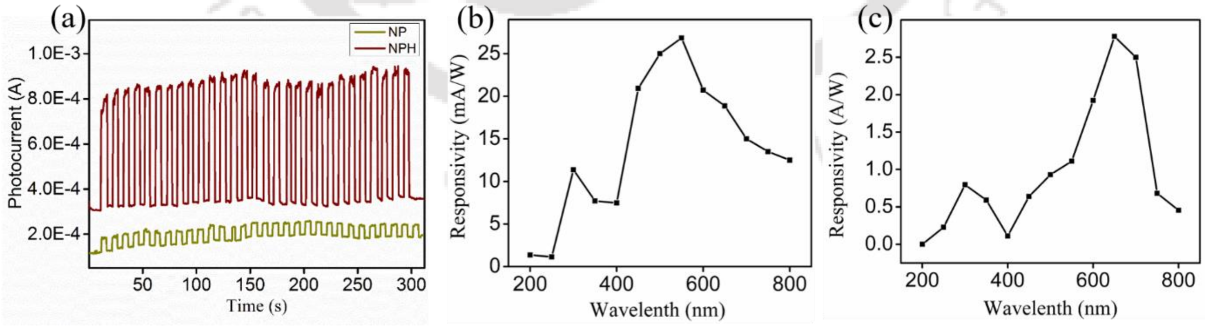

Figure C4.16. Comparison of (a) photoresponse characteristics of Au NP-PA assembly device and as-synthesised Au NP device at an illumination intensity of 2 mW/cm^2 (bias voltage 2 V). Responsivity vs wavelength dependent characteristics of (b) as-synthesised Au NP device and (c) Au NP-PA network device.

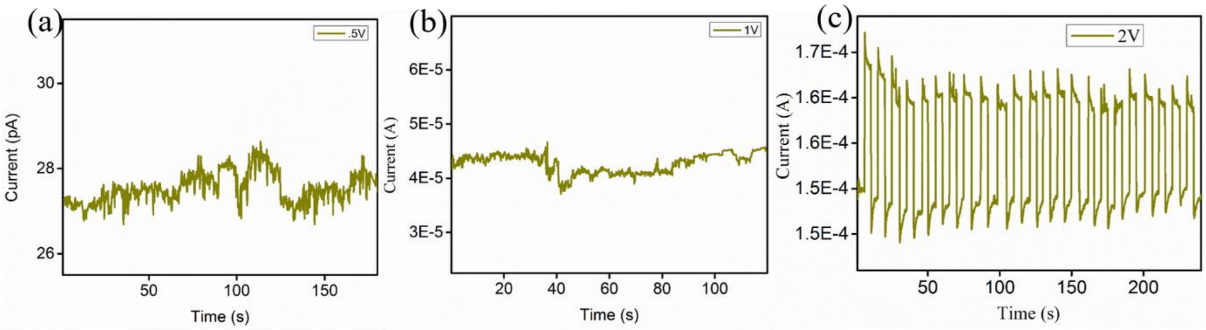

Figure C4.17. Comparison of (a) photoresponse characteristics of as-synthesised Au NP device at a bias voltage of (a) 500 mV (b) 1 V (c) 2 V an illumination intensity of 2 mW/cm^2.

Table C2. Performance parameters of piezo-phototronic response

Material	**Plasmonic**	**Responsivity**	**Detectivity**	**Response time**	**Piezo-phototronic**	**Flexi-bility**	**Ref**
$MAPbI_3$ /NaYF$_4$:Yb/Er upconversion nanoparticles	yes	0.27 A W^{-1}	0.76 × 10^{12} Jones	52 ms/. 67 ms,		yes	10
CsPbBr3 microwire	yes	4.2 A/W.	9.9 × 10^8 jones	4/15 ms	yes	yes	11
All-Si based	yes	94.5 mA/W	4.38 × 10^{11} Jones	0.4/ 1.3 ms	no	no	
Au NP-PA assembly (flat condition)	yes	2.5A/W	3.5 × 10^{13} Jones	<20ms	-	-	This work
Au NP-PA assembly (e=3.7%)	yes	309 mA/W	2.16× 10^{10} Jones	5s/13s	yes	yes	This work

References

1. Lee, J.; Kim, S.; Lee, J.; Yang, D.; Park, B. C.; Ryu, S.; Park, I. A stretchable strain sensor based on a metal nanoparticle thin film for human motion detection. *Nanoscale*. **2014**, 6, 11932-11939.

2. Kim, H.; Shaqeel, A.; Han, S.; Kang, J.; Yun, J.; Lee, M.; Lee, S.; Kim, J.; Noh, S.; Choi, M.; Lee, J. In Situ Formation of Ag Nanoparticles for Fiber Strain Sensors: Toward Textile-Based Wearable Applications. *ACS Applied Materials & Interfaces*. **2021**, 13, 39868-39879.

3. Ly, T. N.; Park, S. Wearable strain sensor for human motion detection based on ligand-exchanged gold nanoparticles. *Journal of Industrial and Engineering Chemistry*. **2020**, 82, 122-129.

4. Lee, J.; Shin, S.; Lee, S.; Song, J.; Kang, S.; Han, H.; Kim, S.; Kim, S.; Seo, J.; Kim, D.; Lee, T. Highly Sensitive Multifilament Fiber Strain Sensors with Ultrabroad Sensing Range for Textile Electronics. *ACS Nano*. **2018**, 12, 4259-4268.

5. Ketelsen, B.; Yesilmen, M.; Schlicke, H.; Noei, H.; Su, C.-H.; Liao, Y.-C.; Vossmeyer, T. Fabrication of Strain Gauges via Contact Printing: A Simple Route to Healthcare Sensors Based on Cross-Linked Gold Nanoparticles. *ACS Applied Materials & Interfaces*. **2018**, 10, 37374-37385.

6. Olichwer, N.; Leib, E. W.; Halfar, A. H.; Petrov, A.; Vossmeyer, T. Cross-Linked Gold Nanoparticles on Polyethylene: Resistive Responses to Tensile Strain and Vapors. *ACS Applied Materials & Interfaces*. **2012**, 4, 6151-6161.

7. Zou, Q.; He, K.; Ou-Yang, J.; Zhang, Y.; Shen, Y.; Jin, C. Highly Sensitive and Durable Sea-Urchin-Shaped Silver Nanoparticles Strain Sensors for Human-Activity Monitoring. *ACS Applied Materials & Interfaces*. **2021**, 13, 14479-14488.

8. Huang, C.-B.; Yao, Y.; Montes-García, V.; Stoeckel, M.-A.; Von Holst, M.; Ciesielski, A.; Samorì, P. Highly Sensitive Strain Sensors Based on Molecules–Gold Nanoparticles Networks for High-Resolution Human Pulse Analysis. *Small*. **2021**, 17, 2007593.

9. Amjadi, M.; Pichitpajongkit, A.; Lee, S.; Ryu, S.; Park, I. Highly Stretchable and Sensitive Strain Sensor Based on Silver Nanowire–Elastomer Nanocomposite. *ACS Nano*. **2014**, 8, 5154-5163.

10. Li, J.; Shen, Y.; Liu, Y.; Shi, F.; Ren, X.; Niu, T.; Zhao, K.; Liu, S. F. Stable High-Performance Flexible Photodetector Based on Upconversion Nanoparticles/Perovskite Microarrays Composite. *ACS Applied Materials & Interfaces*. **2017**, 9, 19176-19183.

11. Yang, Z.; Jiang, M.; Guo, L.; Hu, G.; Gu, Y.; Xi, J.; Huo, Z.; Li, F.; Wang, S.; Pan, C. A high performance CsPbBr3 microwire based photodetector boosted by coupling plasmonic and piezo-phototronic effects. *Nano Energy*. **2021**, 85, 105951.

Chapter 5

Summery and Future Prospects

5.1 Conclusions

The dissertation work is focused on solid state semiconducting device fabrication using functional nanomaterials targeted towards optoelectronic and mechanoreceptive sensors. In particular, charge transport characteristics of white light emitting Qdot complex (QDC), performance of self-powered UV detector based on the QDC and multi-stimuli response of a tactile sensor based on nanoparticle assembly were studied.

In brief, charge transport characteristics of white light emitting quantum dot complex (Mn^{2+} doped ZnS Qdot surface complexed with 8-hydroxyquinoline 5- sulphonic acid) was studied, which exhibited ambipolar transport characteristics in a thin film transistor framework with high carrier mobilities and I_{ON}/I_{OFF} ratio. In addition, carrier hopping characteristics were analysed at low temperature regimes. Electron mobility and hole mobility in QDC system exhibited nearest neighbour hopping (NNH) characteristics between 257 and 357 K and variable-range hopping (VRH) characteristics between 77 and 217 K.

Mn^{2+} doped ZnS Qdot being a wide band gap material, was used for fast UVC detection. The UV detection properties of QDC was also analysed and a shift in the detection band from UVC in Qdot photodetector to UVA in QDC photodetector was observed. The device operations under self-powered mode was analysed, which elucidated fast response and high responsivity and detectivity. The detectors were then incorporated with ARDUINO UNO microcontroller unit and the device responses were calibrated to selectively detect UVA and UVC in a portable prototype. On account of the white light emitting feature of QDC, it was used as an anti- counterfeiting ink for data encryption, where orange emitting Qdot was used as the interfering agent.

A tactile sensor was developed by employing 2-picolylamine (2-PA) ligand mediated controlled assembly of gold nanoparticle (Au NP- PA) and lithographically patterned polydimethylsiloxane (PDMS) microstructures. Ligand interactions enhanced the carrier tunnelling between the nanoparticles in the nanoparticle assembly and exhibited high piezo-resistive characteristics with a gauge factor of 240±6. On application of external mechanical stimuli, the micro-patterned PDMS layer provided with different degree of pressure to the nanoparticle assembly, which was translated to electrical response in the tactile sensor. The tactile sensor was used to identify variable weights, vibrations, and tapping action. Subsequently, the photoresponse characteristics of the device were investigated under tensile strain. The piezo-phototronic responses of Au NP-PA network device together with vibration and strain sensitivity make it a multifunctional tactile sensor, which could find potential applications in wearable electronics.

5.2 Future Prospects

White light emitters have significant importance in the commercial displays. Commercially, white light emission is obtained from multicomponent systems. However, white light emission from a single moiety is vital and has multifaceted importance in terms of reduced device complexity and internal losses. Therefore, electroluminescence characteristics of white light emitting Qdot complex - reported in the thesis - is an important aspect that could be studied.

The surface complexation routes to alter the absorption and emission properties of the photoactive material could be studied for detection of specific spectral bands. Heterostructured devices with 2-D nanomaterials could be perused targeting an enhanced responsivity and self-powered detection.

Ligand mediated nanoparticle assembly has significant importance towards plasmonics and catalytic applications but are less explored for applications as plasmatic photodetectors as well as flexible sensors. Polymeric composites of such nanoparticle assembly could be used to fabricate piezo-resistive, piezo-capacitive, and piezo-electric flexible sensors that are important in the field of wearable electronics for potential applications towards health monitoring systems, smart watches, electronic skin etc. Such compositions could also be perused to fabricate energy harvesters. Au NP network could also be studied as conductive inks for printable electronics pertaining to its greater conductivity due to favourable carrier tunnelling.

Data processing and wireless transmission is the bottleneck in designing such sensors. Transmitting data wirelessly limits the area of coverage whereas, wired data transmission increases the device complexity and latency. In addition to this, sensor outputs from arrayed units need to be differentiated and comprehended for each actuation event. This would require large number of data handling, calibrations, signal processing and filtering so as to achieve optimal efficiency with highest precision. Thus interdisciplinary approach of cloud computing, machine learning, big data analysis along with the design and development of sensors hold promise for successful shift from silicon technology to flexible and printable technology.

Publications

Publication from Thesis Work

1. **Gogoi, K**.; Pramanik, S.; Chattopadhyay, A. Charge Transport Characteristics of Surface-Complexed Quantum Dot in a Thin Film Transistor. ***Advanced Materials Interfaces.*** **2020, 7, 1901665.**
2. **Gogoi, K**.; Chattopadhyay, A. Surface Engineering of Quantum Dots for Self-Powered Ultraviolet Photodetection and Information Encryption. ***Langmuir.*** **2022, 38, 2668-2676.**
3. **Gogoi, K**; Pal S; Chattopadhyay, A. Multi-stimuli responsive gold nanoparticle network based tactile sensor for human activity recognition and piezophototronic detection. (**Manuscript under preparation**)

Publication from Collaborative Work

1. Gayen, C.; Goswami, U.; **Gogoi, K**.; Basu, S.; Paul, A. Crystallization-Induced Emission Enhancement of Nanoclusters and One-Step Conversion of "Nanoclusters to Nanoparticles" as the Basis for Intracellular Logic Operations. *ChemPhysChem.* 2019, 20, 953-958.

Conferences and Workshops Attended

1. Participated in Indian Nanoelectronics users' program - Idea to Innovation (INUP - i2i) 2022.
2. Participated in the International Conference on Advanced Nanomaterials and Nanotechnology (ICANN-2017), organised by Centre for Nanotechnology, IIT Guwahati.
3. Poster presentation at International Conference on Advanced Nanomaterials and Nanotechnology (ICANN-2019), organised by Centre for Nanotechnology, IIT Guwahati.
4. Oral presentation at International Conference on Advanced Nanomaterials and Nanotechnology (ICANN-2021) organised by Centre for Nanotechnology, IIT Guwahati.
5. NWNTD (National Workshop on Nanoelectronics and Theranostic devices) 2016 organized by Centre for Nanotechnology, IIT Guwahati.

6. NWNTD (National Workshop on Nanoelectronics and Theranostic devices) 2017 organized by Centre for Nanotechnology, IIT Guwahati.
7. NWNTD (National Workshop on Nanoelectronics and Theranostic devices) 2018 organized by Centre for Nanotechnology, IIT Guwahati.
8. NWNTD (National Workshop on Nanoelectronics and Theranostic devices) 2019 organized by Centre for Nanotechnology, IIT Guwahati.

Permissions

Figure 1.2 b

JOHN WILEY AND SONS LICENSE
TERMS AND CONDITIONS
Apr 08, 2022

This Agreement between Ms. Kasturi Gogoi ("You") and John Wiley and Sons ("John Wiley and Sons") consists of your license details and the terms and conditions provided by John Wiley and Sons and Copyright Clearance Center.

License Number	5270060759843
License date	Mar 15, 2022
Licensed Content Publisher	John Wiley and Sons
Licensed Content Publication	Advanced Functional Materials
Licensed Content Title	Organization of Matter on Different Size Scales: Monodisperse Nanocrystals and Their Superstructures
Licensed Content Author	H. Weller, M. Haase, A. Kornowski, et al
Licensed Content Date	Oct 21, 2002
Licensed Content Volume	12
Licensed Content Issue	10
Licensed Content Pages	12
Type of use	Dissertation/Thesis
Requestor type	University/Academic
Format	Electronic
Portion	Figure/table
Number of figures/tables	1
Will you be translating?	No

Title	Nano-Enabled Optoelectronic and Mechatronic devices
Institution name	Indian Institute of Technology Guwahati
Expected presentation date	Mar 2022
Portions	Figure 1.b
Requestor Location	Ms. Kasturi Gogoi Centre for Nanotechnology, IIT Guwahati Amingaon North Guwahati Guwahati, Assam 781039 India Attn: Ms. Kasturi Gogoi
Publisher Tax ID	EU826007151
Total	0.00 USD

Figure 1.4 a

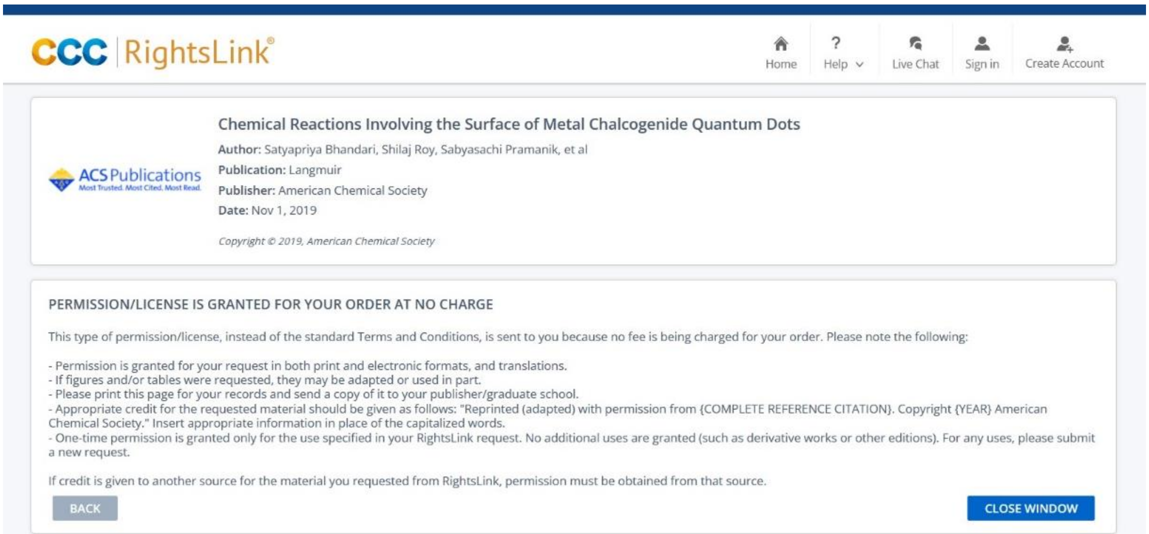

Chemical Reactions Involving the Surface of Metal Chalcogenide Quantum Dots

Author: Satyapriya Bhandari, Shilaj Roy, Sabyasachi Pramanik, et al
Publication: Langmuir
Publisher: American Chemical Society
Date: Nov 1, 2019

Copyright © 2019, American Chemical Society

PERMISSION/LICENSE IS GRANTED FOR YOUR ORDER AT NO CHARGE

This type of permission/license, instead of the standard Terms and Conditions, is sent to you because no fee is being charged for your order. Please note the following:

- Permission is granted for your request in both print and electronic formats, and translations.
- If figures and/or tables were requested, they may be adapted or used in part.
- Please print this page for your records and send a copy of it to your publisher/graduate school.
- Appropriate credit for the requested material should be given as follows: "Reprinted (adapted) with permission from {COMPLETE REFERENCE CITATION}. Copyright {YEAR} American Chemical Society." Insert appropriate information in place of the capitalized words.
- One-time permission is granted only for the use specified in your RightsLink request. No additional uses are granted (such as derivative works or other editions). For any uses, please submit a new request.

If credit is given to another source for the material you requested from RightsLink, permission must be obtained from that source.

Figure 1.4 b

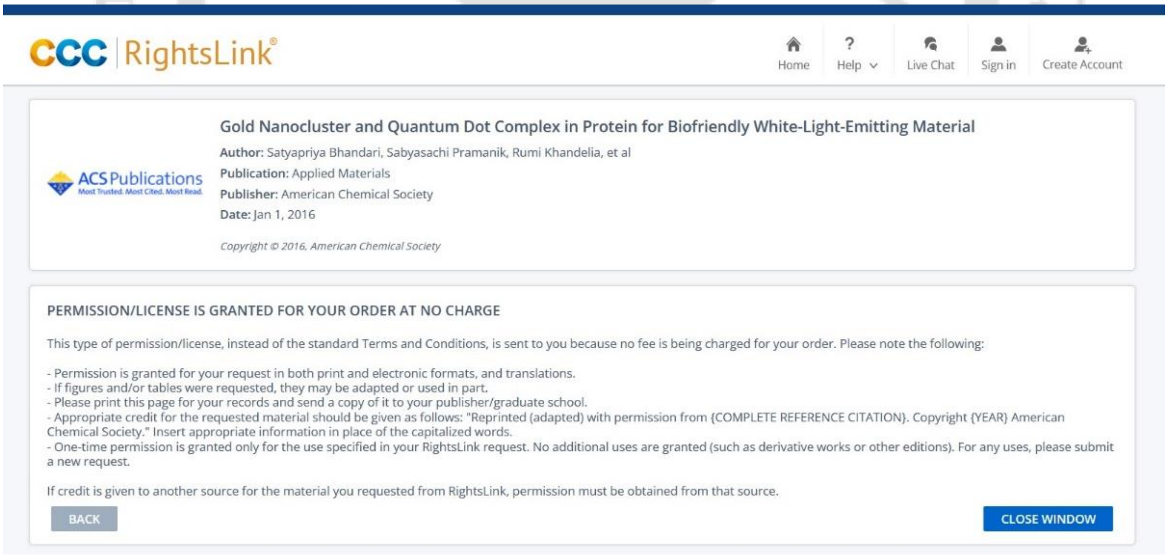

Gold Nanocluster and Quantum Dot Complex in Protein for Biofriendly White-Light-Emitting Material

Author: Satyapriya Bhandari, Sabyasachi Pramanik, Rumi Khandelia, et al
Publication: Applied Materials
Publisher: American Chemical Society
Date: Jan 1, 2016

Copyright © 2016, American Chemical Society

PERMISSION/LICENSE IS GRANTED FOR YOUR ORDER AT NO CHARGE

This type of permission/license, instead of the standard Terms and Conditions, is sent to you because no fee is being charged for your order. Please note the following:

- Permission is granted for your request in both print and electronic formats, and translations.
- If figures and/or tables were requested, they may be adapted or used in part.
- Please print this page for your records and send a copy of it to your publisher/graduate school.
- Appropriate credit for the requested material should be given as follows: "Reprinted (adapted) with permission from {COMPLETE REFERENCE CITATION}. Copyright {YEAR} American Chemical Society." Insert appropriate information in place of the capitalized words.
- One-time permission is granted only for the use specified in your RightsLink request. No additional uses are granted (such as derivative works or other editions). For any uses, please submit a new request.

If credit is given to another source for the material you requested from RightsLink, permission must be obtained from that source.

Figure 1.6 a

Case CSCSI0062344 solution proposed: PLEASE DO NOT REPLY

ACS Publications <acs@service-now.com>

Fri 4/8/2022 1:23 PM

Solution proposed to your case.

Short Description: Permissions to Reprint for thesis work -- DOI: 10.1021/acsnano.8b07938 -- Figure 1a
Priority: 3 – Moderate

If you feel your case is not completely resolved, please select the button below and select "Reject Solution" from the portal.

Comments:

04-08-2022 01:23:45 PM EDT - Raquel Picar-Simpson Additional comments

Dear Kasturi Gogoi,

RE: Permissions to Reprint for thesis work -- DOI: 10.1021/acsnano.8b07938 -- Figure 1a

Your permission requested is granted, and there is no fee for this reuse. In your planned reuse, you must cite the ACS article as the source, add this direct link https://pubs.acs.org/doi/10.1021/acsnano.8b07938, and include a notice to readers that further permissions related to the material excerpted should be directed to the ACS.

If you need further assistance, please let me know.

Best regards,
Raquel
~~~~~~~~~~~~~~~~~~~~~~~~~~~~~~~~~~~~

Raquel Picar-Simpson
ACS Publications Support
Customer Services & Information
Website: https://acs.service-now.com/acs
Email: support@services.acs.org
Phone: 800-227-9919 | 202-872-(HELP) 4357
~~~~~~~~~~~~~~~~~~~~~~~~~~~~~~~~~~~~

Permissions to Reprint for thesis work

MS. KASTURI GOGOI

Fri 4/8/2022 12:24 PM

Dear Sir/Madam

With due respect, I would like to request you to kindly provide me the **rights and permissions** to reprint Figure 1a of the article entitled "Electroluminescence generation in PbS Quantum Dot Light-Emitting Field-Effect Transistors with Solid-State Gating" for my thesis. https://doi.org/10.1021/acsnano.8b07938.

I would be grateful for your kind considerations.

With regards,

Kasturi Gogoi

Indian Institute of Technology Guwahati

Figure 1.6 b

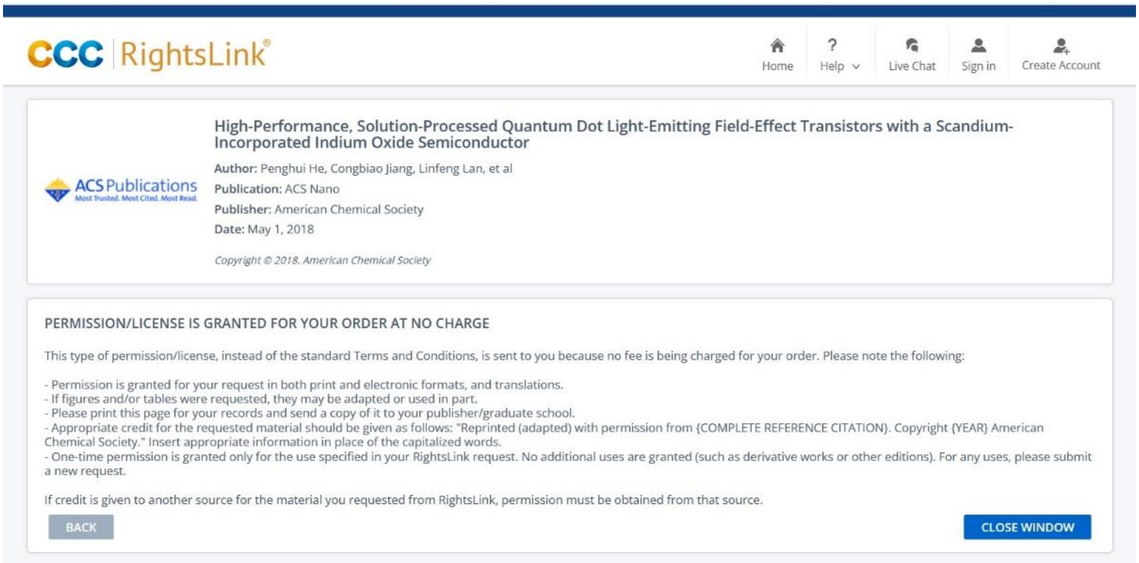

High-Performance, Solution-Processed Quantum Dot Light-Emitting Field-Effect Transistors with a Scandium-Incorporated Indium Oxide Semiconductor

Author: Penghui He, Congbiao Jiang, Linfeng Lan, et al
Publication: ACS Nano
Publisher: American Chemical Society
Date: May 1, 2018

Copyright © 2018, American Chemical Society

PERMISSION/LICENSE IS GRANTED FOR YOUR ORDER AT NO CHARGE

This type of permission/license, instead of the standard Terms and Conditions, is sent to you because no fee is being charged for your order. Please note the following:

- Permission is granted for your request in both print and electronic formats, and translations.
- If figures and/or tables were requested, they may be adapted or used in part.
- Please print this page for your records and send a copy of it to your publisher/graduate school.
- Appropriate credit for the requested material should be given as follows: "Reprinted (adapted) with permission from {COMPLETE REFERENCE CITATION}. Copyright {YEAR} American Chemical Society." Insert appropriate information in place of the capitalized words.
- One-time permission is granted only for the use specified in your RightsLink request. No additional uses are granted (such as derivative works or other editions). For any uses, please submit a new request.

If credit is given to another source for the material you requested from RightsLink, permission must be obtained from that source.

Figure 1.7

JOHN WILEY AND SONS LICENSE
TERMS AND CONDITIONS
Apr 08, 2022

This Agreement between Ms. Kasturi Gogoi ("You") and John Wiley and Sons ("John Wiley and Sons") consists of your license details and the terms and conditions provided by John Wiley and Sons and Copyright Clearance Center.

License Number	5284131416359
License date	Apr 08, 2022
Licensed Content Publisher	John Wiley and Sons
Licensed Content Publication	SMALL STRUCTURES
Licensed Content Title	Band Alignment Engineering in Two-Dimensional Transition Metal Dichalcogenide-Based Heterostructures for Photodetectors
Licensed Content Author	Ran Liu, Fakun Wang, Lixin Liu, et al
Licensed Content Date	Dec 21, 2020
Licensed Content Volume	2
Licensed Content Issue	3
Licensed Content Pages	27
Type of use	Dissertation/Thesis
Requestor type	University/Academic
Format	Electronic
Portion	Figure/table
Number of figures/tables	1
Will you be translating?	No
Title	Nano-Enabled Optoelectronic and Mechatronic devices

Institution name	Indian Institute of Technology Guwahati
Expected presentation date	Apr 2022
Portions	Figure 2
Requestor Location	Ms. Kasturi Gogoi Centre for Nanotechnology, IIT Guwahati Amingaon North Guwahati Guwahati, Assam 781039 India Attn: Ms. Kasturi Gogoi
Publisher Tax ID	EU826007151
Total	0.00 USD
Terms and Conditions	

Figure 1.8 a

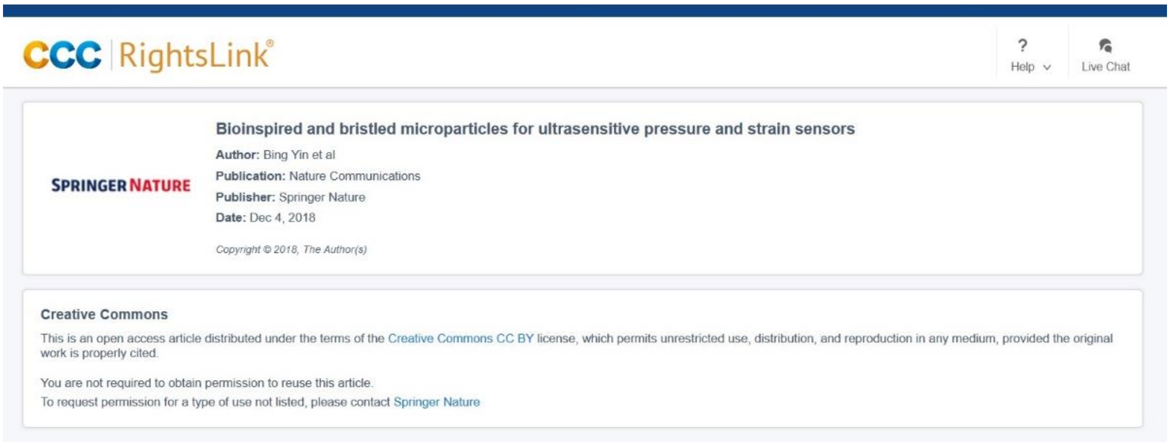

Bioinspired and bristled microparticles for ultrasensitive pressure and strain sensors

Author: Bing Yin et al
Publication: Nature Communications
Publisher: Springer Nature
Date: Dec 4, 2018

Copyright © 2018, The Author(s)

Creative Commons

This is an open access article distributed under the terms of the Creative Commons CC BY license, which permits unrestricted use, distribution, and reproduction in any medium, provided the original work is properly cited.

You are not required to obtain permission to reuse this article.
To request permission for a type of use not listed, please contact Springer Nature

Figure 1.8 b

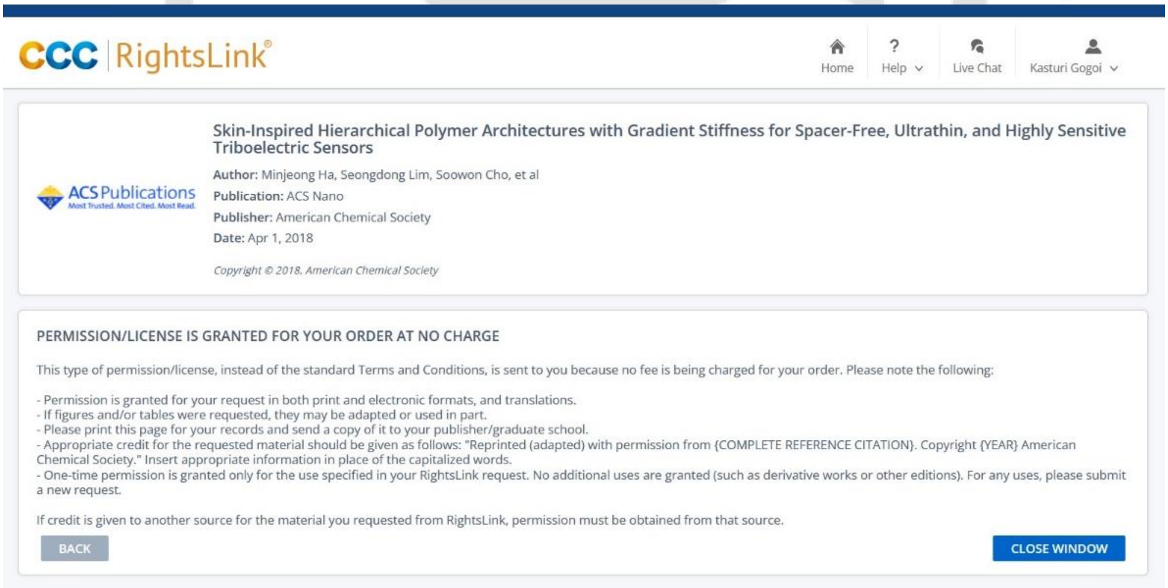

Skin-Inspired Hierarchical Polymer Architectures with Gradient Stiffness for Spacer-Free, Ultrathin, and Highly Sensitive Triboelectric Sensors

Author: Minjeong Ha, Seongdong Lim, Soowon Cho, et al
Publication: ACS Nano
Publisher: American Chemical Society
Date: Apr 1, 2018

Copyright © 2018, American Chemical Society

PERMISSION/LICENSE IS GRANTED FOR YOUR ORDER AT NO CHARGE

This type of permission/license, instead of the standard Terms and Conditions, is sent to you because no fee is being charged for your order. Please note the following:

- Permission is granted for your request in both print and electronic formats, and translations.
- If figures and/or tables were requested, they may be adapted or used in part.
- Please print this page for your records and send a copy of it to your publisher/graduate school.
- Appropriate credit for the requested material should be given as follows: "Reprinted (adapted) with permission from {COMPLETE REFERENCE CITATION}. Copyright {YEAR} American Chemical Society." Insert appropriate information in place of the capitalized words.
- One-time permission is granted only for the use specified in your RightsLink request. No additional uses are granted (such as derivative works or other editions). For any uses, please submit a new request.

If credit is given to another source for the material you requested from RightsLink, permission must be obtained from that source.

Figure 1.8 c

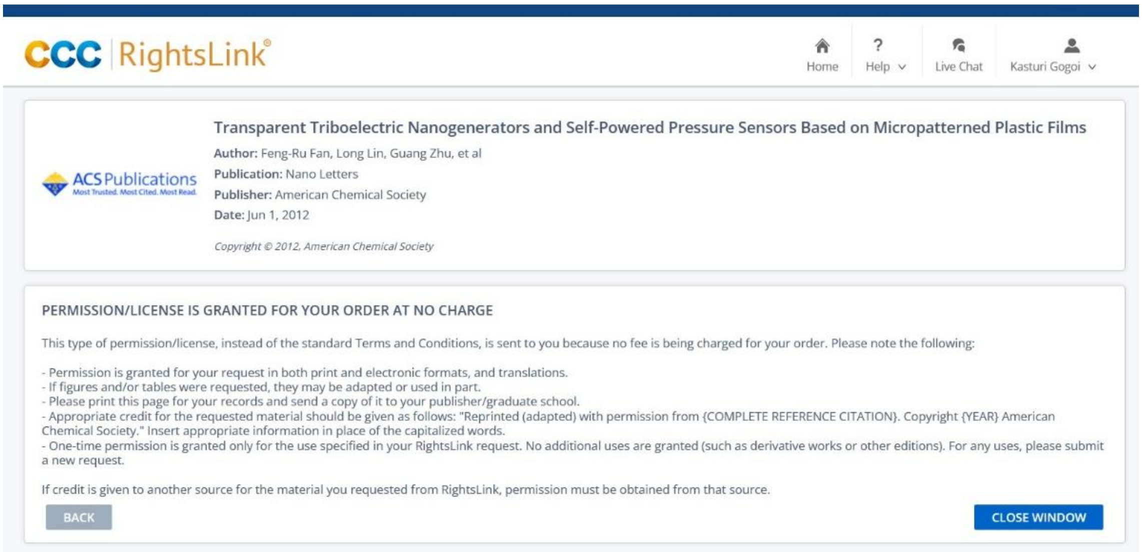

Transparent Triboelectric Nanogenerators and Self-Powered Pressure Sensors Based on Micropatterned Plastic Films

Author: Feng-Ru Fan, Long Lin, Guang Zhu, et al

Publication: Nano Letters

Publisher: American Chemical Society

Date: Jun 1, 2012

Copyright © 2012, American Chemical Society

PERMISSION/LICENSE IS GRANTED FOR YOUR ORDER AT NO CHARGE

This type of permission/license, instead of the standard Terms and Conditions, is sent to you because no fee is being charged for your order. Please note the following:

- Permission is granted for your request in both print and electronic formats, and translations.
- If figures and/or tables were requested, they may be adapted or used in part.
- Please print this page for your records and send a copy of it to your publisher/graduate school.
- Appropriate credit for the requested material should be given as follows: "Reprinted (adapted) with permission from {COMPLETE REFERENCE CITATION}. Copyright {YEAR} American Chemical Society." Insert appropriate information in place of the capitalized words.
- One-time permission is granted only for the use specified in your RightsLink request. No additional uses are granted (such as derivative works or other editions). For any uses, please submit a new request.

If credit is given to another source for the material you requested from RightsLink, permission must be obtained from that source.

Figure 1.8 d

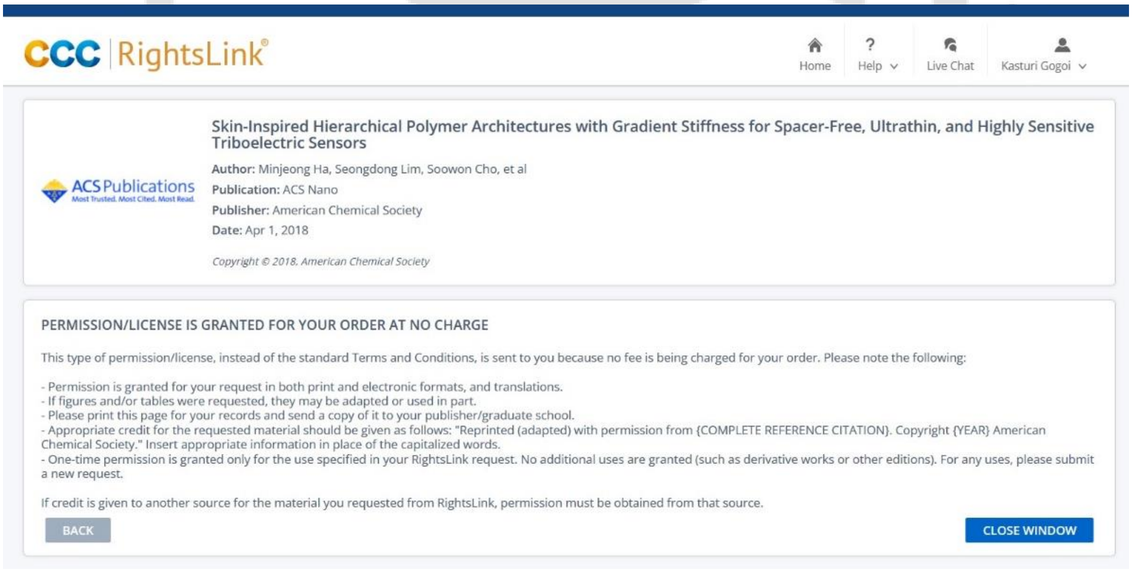

Skin-Inspired Hierarchical Polymer Architectures with Gradient Stiffness for Spacer-Free, Ultrathin, and Highly Sensitive Triboelectric Sensors

Author: Minjeong Ha, Seongdong Lim, Soowon Cho, et al

Publication: ACS Nano

Publisher: American Chemical Society

Date: Apr 1, 2018

Copyright © 2018, American Chemical Society

PERMISSION/LICENSE IS GRANTED FOR YOUR ORDER AT NO CHARGE

This type of permission/license, instead of the standard Terms and Conditions, is sent to you because no fee is being charged for your order. Please note the following:

- Permission is granted for your request in both print and electronic formats, and translations.
- If figures and/or tables were requested, they may be adapted or used in part.
- Please print this page for your records and send a copy of it to your publisher/graduate school.
- Appropriate credit for the requested material should be given as follows: "Reprinted (adapted) with permission from {COMPLETE REFERENCE CITATION}. Copyright {YEAR} American Chemical Society." Insert appropriate information in place of the capitalized words.
- One-time permission is granted only for the use specified in your RightsLink request. No additional uses are granted (such as derivative works or other editions). For any uses, please submit a new request.

If credit is given to another source for the material you requested from RightsLink, permission must be obtained from that source.

Figure 1.8 e

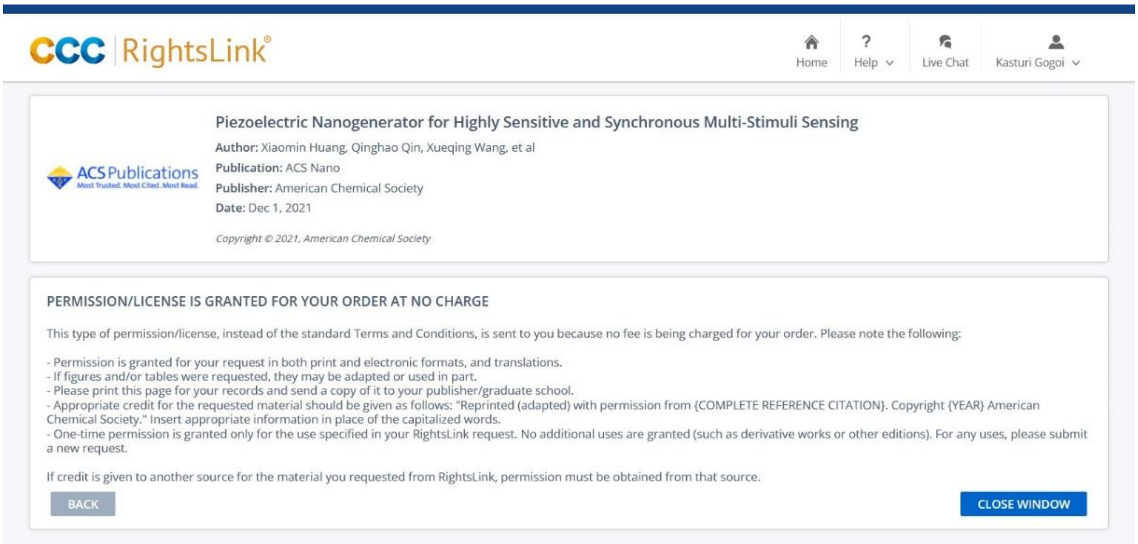

Piezoelectric Nanogenerator for Highly Sensitive and Synchronous Multi-Stimuli Sensing

Author: Xiaomin Huang, Qinghao Qin, Xueqing Wang, et al

Publication: ACS Nano

Publisher: American Chemical Society

Date: Dec 1, 2021

Copyright © 2021, American Chemical Society

PERMISSION/LICENSE IS GRANTED FOR YOUR ORDER AT NO CHARGE

This type of permission/license, instead of the standard Terms and Conditions, is sent to you because no fee is being charged for your order. Please note the following:

- Permission is granted for your request in both print and electronic formats, and translations.
- If figures and/or tables were requested, they may be adapted or used in part.
- Please print this page for your records and send a copy of it to your publisher/graduate school.
- Appropriate credit for the requested material should be given as follows: "Reprinted (adapted) with permission from {COMPLETE REFERENCE CITATION}. Copyright {YEAR} American Chemical Society." Insert appropriate information in place of the capitalized words.
- One-time permission is granted only for the use specified in your RightsLink request. No additional uses are granted (such as derivative works or other editions). For any uses, please submit a new request.

If credit is given to another source for the material you requested from RightsLink, permission must be obtained from that source.

Figure 1.8 f

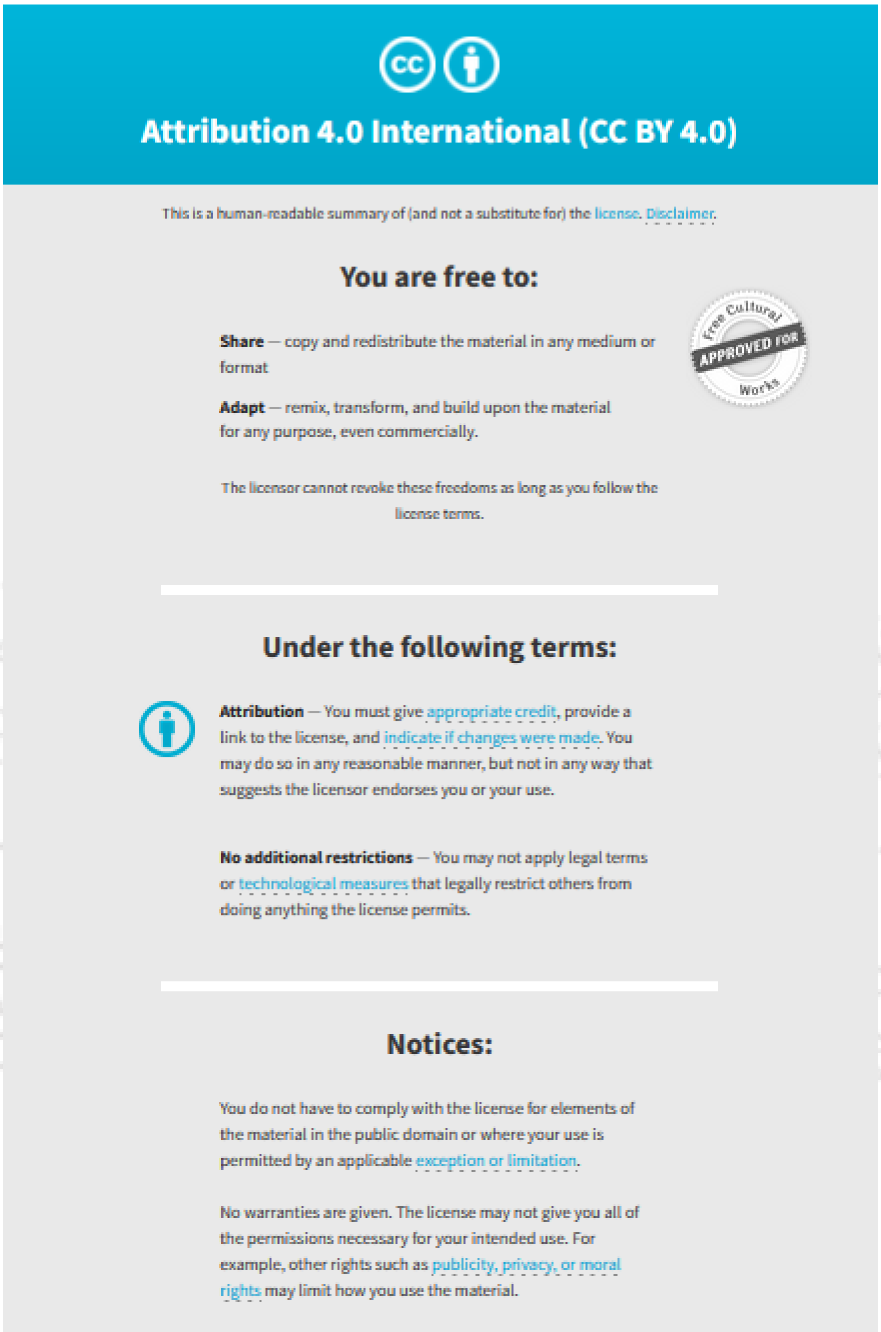

Attribution 4.0 International (CC BY 4.0)

This is a human-readable summary of (and not a substitute for) the license. Disclaimer.

You are free to:

Share — copy and redistribute the material in any medium or format

Adapt — remix, transform, and build upon the material for any purpose, even commercially.

The licensor cannot revoke these freedoms as long as you follow the license terms.

Under the following terms:

Attribution — You must give appropriate credit, provide a link to the license, and indicate if changes were made. You may do so in any reasonable manner, but not in any way that suggests the licensor endorses you or your use.

No additional restrictions — You may not apply legal terms or technological measures that legally restrict others from doing anything the license permits.

Notices:

You do not have to comply with the license for elements of the material in the public domain or where your use is permitted by an applicable exception or limitation.

No warranties are given. The license may not give you all of the permissions necessary for your intended use. For example, other rights such as publicity, privacy, or moral rights may limit how you use the material.

Figure 1.8 g

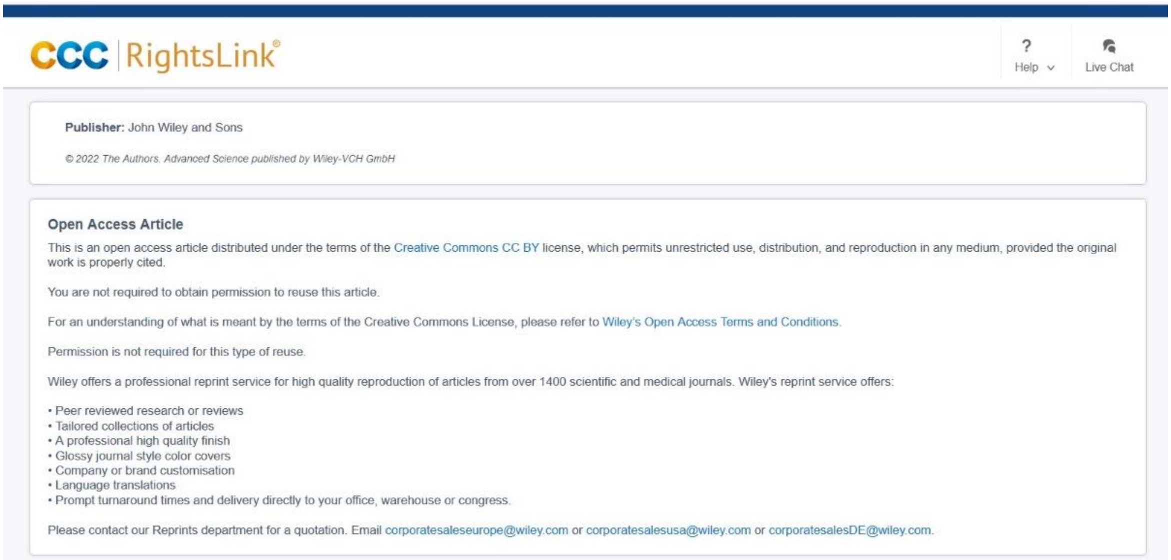

Publisher: John Wiley and Sons

© 2022 The Authors. Advanced Science published by Wiley-VCH GmbH

Open Access Article

This is an open access article distributed under the terms of the Creative Commons CC BY license, which permits unrestricted use, distribution, and reproduction in any medium, provided the original work is properly cited.

You are not required to obtain permission to reuse this article.

For an understanding of what is meant by the terms of the Creative Commons License, please refer to Wiley's Open Access Terms and Conditions.

Permission is not required for this type of reuse.

Wiley offers a professional reprint service for high quality reproduction of articles from over 1400 scientific and medical journals. Wiley's reprint service offers:

- Peer reviewed research or reviews
- Tailored collections of articles
- A professional high quality finish
- Glossy journal style color covers
- Company or brand customisation
- Language translations
- Prompt turnaround times and delivery directly to your office, warehouse or congress.

Please contact our Reprints department for a quotation. Email corporatesaleseurope@wiley.com or corporatesalesusa@wiley.com or corporatesalesDE@wiley.com.

Chapter 2

JOHN WILEY AND SONS LICENSE
TERMS AND CONDITIONS
Apr 08, 2022

This Agreement between Ms. Kasturi Gogoi ("You") and John Wiley and Sons ("John Wiley and Sons") consists of your license details and the terms and conditions provided by John Wiley and Sons and Copyright Clearance Center.

License Number	5283770048342
License date	Apr 07, 2022
Licensed Content Publisher	John Wiley and Sons
Licensed Content Publication	Advanced Materials Interfaces
Licensed Content Title	Charge Transport Characteristics of Surface-Complexed Quantum Dot in a Thin Film Transistor
Licensed Content Author	Arun Chattopadhyay, Sabyasachi Pramanik, Kasturi Gogoi
Licensed Content Date	Jan 1, 2020
Licensed Content Volume	7
Licensed Content Issue	4
Licensed Content Pages	9
Type of use	Dissertation/Thesis
Requestor type	Author of this Wiley article
Format	Electronic
Portion	Full article
Will you be translating?	No
Title	Nano-Enabled Optoelectronic and Mechatronic devices
Institution name	Indian Institute of Technology Guwahati
Expected presentation date	Apr 2022

Requestor Location	Ms. Kasturi Gogoi Centre for Nanotechnology, IIT Guwahati Amingaon North Guwahati Guwahati, Assam 781039 India Attn: Ms. Kasturi Gogoi
Publisher Tax ID	EU826007151
Total	0.00 USD

Chapter 3

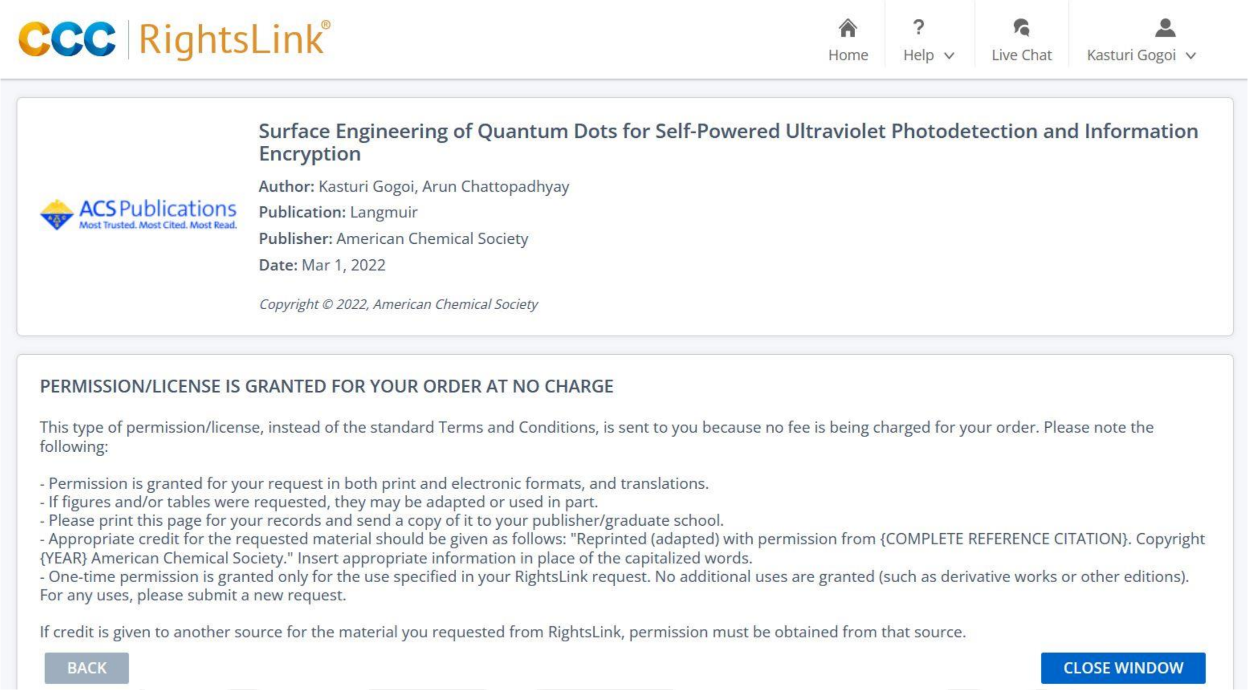

Surface Engineering of Quantum Dots for Self-Powered Ultraviolet Photodetection and Information Encryption

Author: Kasturi Gogoi, Arun Chattopadhyay
Publication: Langmuir
Publisher: American Chemical Society
Date: Mar 1, 2022

Copyright © 2022, American Chemical Society

PERMISSION/LICENSE IS GRANTED FOR YOUR ORDER AT NO CHARGE

This type of permission/license, instead of the standard Terms and Conditions, is sent to you because no fee is being charged for your order. Please note the following:

- Permission is granted for your request in both print and electronic formats, and translations.
- If figures and/or tables were requested, they may be adapted or used in part.
- Please print this page for your records and send a copy of it to your publisher/graduate school.
- Appropriate credit for the requested material should be given as follows: "Reprinted (adapted) with permission from {COMPLETE REFERENCE CITATION}. Copyright {YEAR} American Chemical Society." Insert appropriate information in place of the capitalized words.
- One-time permission is granted only for the use specified in your RightsLink request. No additional uses are granted (such as derivative works or other editions). For any uses, please submit a new request.

If credit is given to another source for the material you requested from RightsLink, permission must be obtained from that source.